A NEW REALISTIC APPROACH TO CONVECTIVE HEAT TRANSFER MODELING AND SIMULATION IN THE PRESENCE OF SWIRLING FLOWS

A DISSERTATION
SUBMITTED TO THE FACULTY OF
UNIVERSITY OF MINNESOTA
BY

Santosh Ilamparuthi

IN PARTIAL FULFILLMENT OF THE REQUIREMENTS
FOR THE DEGREE OF
DOCTOR OF PHILOSOPHY

Ephraim M. Sparrow

December 2017

© Santosh Ilamparuthi 2017

Acknowledgements

This thesis and the journey towards completing it has been a long and hard one. My journey would simply have not been possible without the guidance, support, friendship of many people and it is with joy and gratitude that I would like to acknowledge them here.

First and foremost, I would like to thank Prof. Sparrow or Eph as he insists everyone call him. Eph took me on as a student and agreed to be my adviser when I was in a personally tough spot, and from then on he has been always ready to guide me in both the academic work and with words of advice and encouragement. His patience, kindness and willingness to continue to guide me through his own illness and hardships were enormous sacrifices that I could never payback.

I would also like to thank Dr. John Gorman for always being there to help everyone with their research topics with his insights and encyclopedic knowledge of the software. His knack for navigating the bureaucracy of the university was an asset, which helped greatly when I ran into inadvertent obstacles. John is also a good friend and our conversations both about the research topics and random tangents made work joyful.

I would also like to thank Dr. Abhimanyu Ghosh, who was a both a good friend and colleague throughout the years of working on my PhD. The shared miseries and disappointments made the doldrums bearable and the relief and excitement of completion sweeter.

I would also like to thank all my other friends and colleagues especially, Dr. Jungwon Ahn for his friendship. I want to also thank Shalini, Luca, Amarnath and Aabha, who while not by my side were always in my thoughts, their friendship has been constant and a source of great comfort.

Finally, I want thank my parents, they have been my constant source of love and support without whom none of this would have been possible. Their unwavering belief in me and unflinching support helped me overcome obstacles when my own confidence wavered. Amma and Appa, thank you.

Dedication

This thesis is dedicated to Appa, for teaching me to take the next step and Amma for standing by me while I took it.

Abstract

The thesis deals with internal fluid flows with heat transfer where swirl is a dominant component. The modeling of these flows is important due to their wide prevalence in industrial processes. The use of appropriate turbulence models for swirling flows and verification is performed in the chapter 2. Chapters 3 and 4 deals with applications with swirling flows. This includes the cooling and thermal management of a PCR machine and studying the thermal and flow behavior of fluid flows in large pipes under directly ducted fan flows.

Fluid flow was visualized with both normalized and non-normalized vector plots while temperature contour plots and turbulence ratio contour plots were utilized to delineate the various thermal and fluid flow regimes which were encountered. The simulations were all carried out in ANSYS – CFX predominantly using versions 14 through 16.

The results demonstrated the need for further adoption of the SST turbulence model especially in flows where swirl was a significant factor.

Table of Contents

List of Tables

List of Figures

Chapter 1

CONVECTIVE HEAT TRANSFER IN THE PRESENCE OF SWIRLING FLOW

1.1 Introduction

The focus of this thesis is a fundamental issue in convection heat transfer. It is well known that both convective heat and mass transfer are intimately connected with fluid flow. In fact, heat transfer rates may be considered to be controlled by the magnitude and direction of the fluid flow. In view of this intimate relationship, it is necessary that the fluid flow results which control convective heat transfer be accurate. In simple terms, the central issue to be addressed here is whether the fluid flow solutions which are used as input to the analysis of convective heat transfer are fundamentally correct or somehow flawed.

There is an extensive literature which deals with convective heat transfer that appears in a very wide range of scholarly and applications journals. The publications that are most relevant for the present work are referenced in the subsequent chapters.

A historic look back over the decades will recognize that the simplifications inherent in Prandtl's boundary layer theory are responsible for a certain level of inaccuracy in fluid mechanic outcomes. In particular, it is relevant to recognized that fluid motion is governed by advection and diffusion taken together in the Navier-Stokes equations. The boundary layer theory removed the streamwise component of diffusion. This omission removes the capability of the fluid to see in advance what is ahead of it. From the mathematical point of view, this alters the nature of the governing partial differential equations of fluid from elliptic to parabolic. In this regard, parabolic partial differential equations are easier to solve than are elliptic partial differential equations. This is especially true in the case of numerical solutions.

Prandtl's simplifications aside, a more severe source of fluid-flow errors is the arbitrary choices that are made for the inlet velocities in pipe and duct flows. The choice, embedded universally in fluid mechanic textbooks the world over, is that the fluid entering a pipe or duct possesses a uniform velocity profile. This type of profile is, for one thing, incompatible with the no-slip boundary condition at the bounding walls of pipes and ducts. Equally important is the issue of how such a flat profile shape can be obtained. In academic literature of the past, there is a suggestion that if there is an already existing boundary upstream of the inlet, it should be suctioned off through a slot situated at the inlet cross section. Such a practice is not compatible with real-world applications.

The published heat transfer literature for pipe and duct flows also appears to have totally adopted the assumption of a uniform inlet velocity profile. In almost every such case, no discussion or explanation is given about the means by which the flow is delivered to the pipe or duct inlet. In the opinion of the present writer, that assumption is without grounds.

Here, a realistic approach to convective heat transfer modeling and numerical implementation is undertaken. That approach does away with the need for unsupported assumptions. Instead, actual fluid movers are modeled with high fidelity so that inlet velocity profiles are actually those that are produced by the rotating member contained within the fluid moving device. Beyond the issue of the shape of the velocity profile, an equally important matter is the nature of the turbulence that is advected into the pipe or duct. It is relevant to note that the vast majority of pipe and duct flows are turbulent, and the magnitude and nature of the turbulence have a marked effect on the behavior of both the fluid flow and convective heat transfer in the pipe or duct. In those publications where the flat velocity profile is adopted, it is rare, if ever, for the turbulence characteristics of the flow entering the pipe to be provided. This is as it should be since, this information, if specified, would be arbitrary. In the present modeling, turbulence will be generated by the operation of the modeled rotating fluid mover.

This thesis is comprised of five chapters, including this introductory one and the final one which is a retrospective overview of the accomplishments of the work. The three intermediate chapters will now outlined.

Since turbulence is such an important issue, Chapter 2 is focused on it. In present-day treatments of turbulence, the most common approach is to select a suitable turbulence model. It appears that certain turbulence models are more suited to specific types of flows than are others. The optimum way to verify the efficacy of a turbulence model is by experimentation. However, during the course of the execution of this thesis, laboratory facilities in the Mechanical Engineering Building were not available.

The most suitable alternative was to scour the published literature for very-well-executed experiments and then to carry out high-fidelity numerical simulations for that physical situation using the same simulation approach as that to be used in later sections of the thesis. The outcome of this work was very positive with respect to the quality of the agreement between the results of the experiments and the predictions of the numerical simulations. This outcome, coupled with literature information where other verifications are described, provided convincing proof that the appropriate model had been chosen.

Chapter 3 was motivated by a critical biomedical application. It relates to a device whose function is to obtain information about the nature of a DNA sample. The device had been designed in the manner in which most engineered devices are designed: (a) by trial and error (Edison approach) or (b) by tweaking an-already-existing similar device. Neither of these approaches can be regarded as satisfactory. Here, using advanced modeling tools and highly effective numerical simulations, a device was designed based on first principles and with a minimum of unsubstantiated simplifying assumptions. The flow was delivered to the inlet of the device by an actual rotating axial fan. Both turbulent fluid and heat transfer were treated simultaneously.

Chapter 4 of the thesis has to do with a practical situation that, to the knowledge of the writer, has never been correctly treated in the literature.

The situation is heat transfer in a round pipe, but now the fluid is delivered to the inlet of the pipe by a realistic means. A rotating axial fan is mated to the inlet cross section of the pipe. The fan draws fluid into it from its upstream and lateral environments and discharges the fluid into the pipe inlet. This process naturally generates turbulence and provides a realistic inlet velocity profile. The fluid flow and heat transfer characteristics obtained in this way are compared with results based on the currently standard, highly simplified model wherein the velocity profile at inlet is flat and the turbulence is unspecified. These comparisons unable definitive conclusions to be drawn about the consequences of using an un-physical model.

Chapter 2

EVALUATION TURBULENCE MODELS FOR SWIRLING FLOWS

2.1 Introduction

The growing sophistication of engineering analysis and design coupled with the increased availability of computing power has given rise to a groundswell of numerical simulations performed by users whose skills do not necessarily include computer science. In particular, it is common for practitioners to use popular turbulence models that are insufficient for the complex problems that are awaiting solution. In addition, issues such as the importance of suitable meshes and the need for fine levels of convergence are widely overlooked in engineering-motivated numerical simulations.

Among the extended areas of interest in engineering fluid mechanics are situations in which swirl and secondary flows play a major role. For example, in piping systems, fittings such as bends, coils, tees, and others experience or promote fluid rotation. Furthermore, in the presence of rotating devices such as turbines, compressors, fans, blowers, and other fluid movers, swirl and fluid rotation are a natural consequence of the action of those devices. In most of the aforementioned physical situations, the fluid flow is turbulent.

If numerical simulation is to be a valid tool for the prediction of the outcomes that relate to such flows, it is necessary that definitive information be available with regard to the best turbulence models for numerical simulating such flows. The goal of this paper is to present such information.

A literature search has demonstrated the considerable attention that has been given to the relative capabilities of turbulence models, especially those that are related to the use of the RANS model of momentum conservation for turbulent flow. The structure of all such papers starts with the selection of a physical situation involving turbulent flow, sometimes of academic nature, and continues with the author(s)'s choice of the turbulence models to

be compared. In most cases, the number of such models is in the range of six. These include, at least, the *original* κ-ε, *RNG* κ-ε, *REAL* κ-ε, κ-ω, *SST* κ-ω, and *RSM*. The *LES* model is sometimes considered in these comparisons, but the participating investigators regularly mention the downsides of *LES* which include extensive computational resources and extended computer time.

In [1], consideration was given to fluid flow in the presence of a wall-attached square cylinder. Three turbulence models were employed, two based on the κ-ε platform and the third being the original κ-ω model. Among these, the *REAL* κ-ε model gave the best agreement with experimental data. Turbulent jets issuing from a cross-shaped orifice were studied in [2] making use of seven models, encompassing four based on the κ-ε platform, two based on the κ-ω platform, and *RSM*. The most suitable predictions compared with experimental data were those of the *SST* κ-ω model. A very different application was selected for study in [3]. There, focus was directed to air motion in enclosed indoor spaces motivated by space conditioning and involving forced convection, natural convection, mixed convection, and combinations thereof. A total of eight turbulence models were investigated, with the outcome being summarized as "while the turbulence models have different performances in each of the flow categories, each airflow category favors specific turbulence models."

Still another category of flow was the focus of [4]. Those authors directed attention to a single staggered array of pin fins in crossflow. The same turbulence models were employed as in the foregoing cited studies. It was concluded that the *SST* κ-ω model gave the best overall agreement with the data, but that other models proved to be suitable for specific metrics.

The paper found from the literature survey which most relates to the present focus of swirling flows is [5]. There, four models based on the κ-ε platform and two based on the κ-ω platform were considered. The investigated situation was a swirling flow passing from

a smaller diameter pipe to a larger diameter pipe by means of an abrupt enlargement. The conclusion was that, similar to those of other comparisons with experimental data, the *SST* κ-ω model was globally closest to the compared data, but that local experimental metrics were better linked to other models.

A closer examination of the comparisons conveyed in [5] revealed very substantial deviations between the predicted and experimental results. It is believed that those deviations are the result of an insufficiency in the implementation of the numerical simulations. The mesh used in [5] consisted of only 12,000 nodes, where a node corresponds to a point at which the governing equations are solved and where results are directly obtained. In current practice, numerical simulation of a problem of the complexity of that of [5] would utilize tens of millions of nodes. This state of affairs creates great uncertainty in the outcomes of [5].

A number of papers published earlier than [5] have dealt with swirling flows and with the appropriateness of various turbulence models. References [6-8] constitute a representative sample. These papers date from an era prior to the wide recognition of the κ-ω platform and its subsequent extension to the *SST* κ-ω model. Consequently, the only available models were those based on the κ-ε and RSM platforms. The physical situations dealt with in these paper include: swirling flow passing through an abrupt enlargement [6], confined annular swirling jets and confined coaxial swirling and counter-swirling jets [7], and strongly swirling flow in a water-model combustion chamber [8]. These simulations are also afflicted with the same insufficiency that plagued [5]—a great paucity of nodes. As was true in [5], nodal paucity precluded excellent agreement between the numerical predictions and the experimental data. Among the turbulence models investigated, those based on the RSM platform gave the best agreement with the data.

Another issue which is relevant to the numerical simulations in general is the matter of convergence. Software vendors often suggest a convergence criterion whose value is larger than appropriate in order to make it appear that their software is faster than that of their

competitors. Convergence is commonly expressed in terms of the values of *rms-normalized* residuals. Residuals are the left overs when a current version of a solution is introduced into the governing discretized equations. Values of normalized residuals that are taken to signal convergence range from 10^{-4} to 10^{-6}, depending on the publication in question. It is the experience of the present authors that convergence to values greater than 10^{-6} are of unacceptable accuracy.

The interest of the present authors in swirling turbulent flows is based on their work on real-world engineering applications where such flows are naturally encountered. One class of such problems is the delivery of fan/blower-supplied air to the inlet of heat exchangers. The air is propelled by the rotation of the fan blades, which impart a strong swirl to the air entering the heat exchanger. With respect to pipe bends and elbows, a strong secondary flow is encountered by fluid flowing through the bend. The secondary flow is, in fact, swirl. Another practical problem of interest to the authors is the separation of particles from a particle-laden gas flow. The separation may be achieved by creating a swirling motion in the gas flow such that the particulates are flung outward toward the bounding wall. The practical importance of these applications has underscored the need to reach a definitive conclusion as to the turbulence model which gives results of high accuracy within the constraints of modeling and computational resources of real-world engineering organizations. It is the aim of this investigation to identify such a model.

The issue of the overall accuracy of a numerical simulation model actually goes beyond the quality of the chosen turbulence model. The simulation is based on the conservation equations for mass and momentum. When the flow is turbulent, the momentum conservations equations may be modified from their basic forms to accommodate turbulence transport. In the case of momentum conservation, the modification is a transformation of the Navier-Stokes equations into the RANS (Reynolds-Averaged Navier-Stokes) equations. In this light, both the RANS equations as well as the turbulence model must both be subjects of the validation effort.

2.2 Physical situation

The determination of a highly competent turbulence model for application to swirling flows will be based on the carefully executed and comprehensive experiments of [9]. The swirl that was investigated there is closely aligned with that encountered in the applications of interest to the present authors. Of great importance is that the measurements of [9] included the turbulence characteristics of the flow at the inlet of the apparatus, thereby enhancing the probability of developing a high-fidelity simulation model.

Figure 2.1 is a schematic diagram of a vertical planar cut through the heart of the experimental apparatus. The vertical plane includes the axis of symmetry of the setup. Owing to symmetry, only the upper half of the plane is displayed in the figure. The boundaries of the space shown in the figure define the solution domain of the numerical simulations. A swirling flow enters at the left of the apparatus and, after passing through a length of straight pipe, empties into a straight-walled diffuser. The total angle of the diffuser is 20^o and its axial length is 510 mm.

Inasmuch as the detailed measurements of [9] provided in-depth information about the axial and tangential velocities and the turbulence-characterizing quantities at the inlet cross-section, the exact means of swirl creation is only of passing interest. Briefly, the swirl was created by a honeycomb affixed rigidly to the inner wall of a rotating pipe. The rotating pipe was followed by a length of stationary pipe, and the measurement cross section was 75 mm downstream from the end of the rotating pipe. Alternatively, the measurement cross section may be characterized as being situated 25 mm from the initiation of the diffuser section. In this light, the solution domain for the velocity problem extended from the measurement cross section to the downstream end of the diffuser.

Other relevant information about the physical situation includes: (a) the flowing fluid is constant-property air, (b) the Reynolds number for the flow in the straight pipe upstream

of the diffuser is 166,150, (c) the mean axial velocity at inlet is 11.6 m/s, and (d) the diameter of the straight-section of pipe is 260 mm.

As a necessary step prior to the consideration of numerical solutions and turbulence modeling, boundary conditions have to be specified, and those related to fluid inflow characteristics have to be extracted from the measurements of [9]. At the inlet cross section illustrated in Fig. 2.1 (25 mm upstream of the diffuser), the inlet boundary conditions include the axial velocity distribution, the swirl (tangential) velocity distribution, the turbulence kinetic energy κ, and the turbulence dissipation ε. Although this quantitative information is available from [9], it is critical for the obtainment of accurate comparisons with the numerical solutions and is, therefore, reproduced here in Figs. 2.2-2.4.

Figure 2.2 displays the profile of the axial velocity at the inlet cross section. This profile differs from the typical turbulent pipe-flow velocity profile in that the maximum velocity is not at the axis ($r = 0$). The maximum velocity exceeds the mean axial velocity U_o by 7%. The unconventional shape of the profile can be attributed to the remnants of the upstream swirl. Data could not be collected sufficiently near the pipe wall to confirm the zero-velocity expectation. Also displayed in Fig. 2.2 is the inlet profile of the swirl velocity. The profile deviates only moderately from rigid-body rotation. The deviation from that model is due primarily to the no-slip velocity condition at the wall.

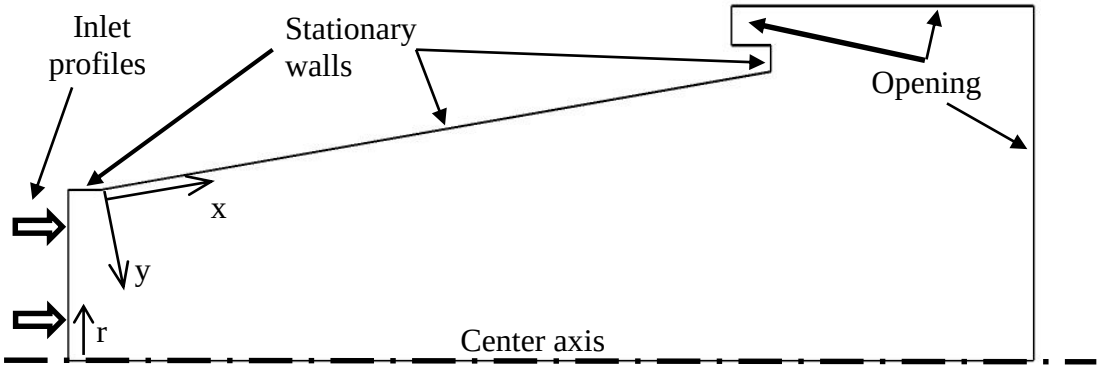

Fig. 2.1: Geometry of the solution domain and the identification of its bounding walls.

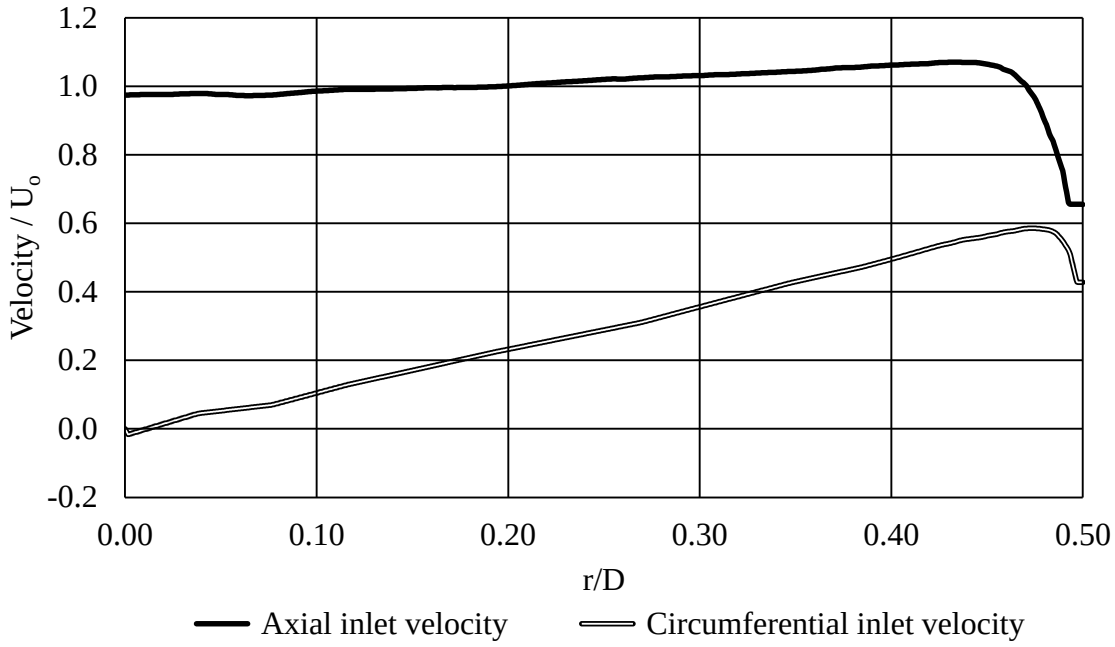

Fig. 2.2: Inlet profiles of the axial and circumferential velocities measured in [9] (*D* = 0.26 m). Processed from data available in [9].

For the implementation of the simulation model, it is also necessary to have information for turbulence quantities at the inlet in order to perform high-fidelity numerical simulations of the experimental situation. Figure 2.3 conveys the profile of the turbulence kinetic energy κ. As a matter of record, the turbulence kinetic energy was not presented in [9]. Rather, the profiles of the individual turbulent velocity fluctuations u', v', and w' were provided there. With these, the turbulence kinetic energy was calculated from

$$\kappa = \frac{1}{2}\left(\overline{u'^2} + \overline{v'^2} + \overline{w'^2}\right) \tag{2.1}$$

Since all the turbulence velocity fluctuations are respectively equal to zero at the wall, it is necessary to explain the seeming paradox displayed in Fig. 2.3 where the turbulence kinetic energy κ, which depends upon the turbulence fluctuations via Eq. (2.1) appears to reach a maximum at the wall *r/D* = 0.5. This unexpected finding can be attributed to the fact that although the turbulence fluctuations are largest in the wall-adjacent boundary layer, they are truly zero at the wall. The dropoff of the κ profile in the near neighborhood of the wall is too sharp to be captured by the graphics package.

The last of the turbulence quantities needed to properly characterize the inlet flow is the turbulence dissipation ε. This quantity is not measured directly, but was calculated by the present authors from the equation

$$\varepsilon = \frac{\kappa^{3/2}}{0.3D} \tag{2.2}$$

where *D* is the diameter of the pipe.

The resulting profile of the turbulence dissipation ε at the inlet is displayed in Fig. 2.4. It can be seen from the figure that the shape of the dissipation profile closely reflects the turbulence kinetic energy profile.

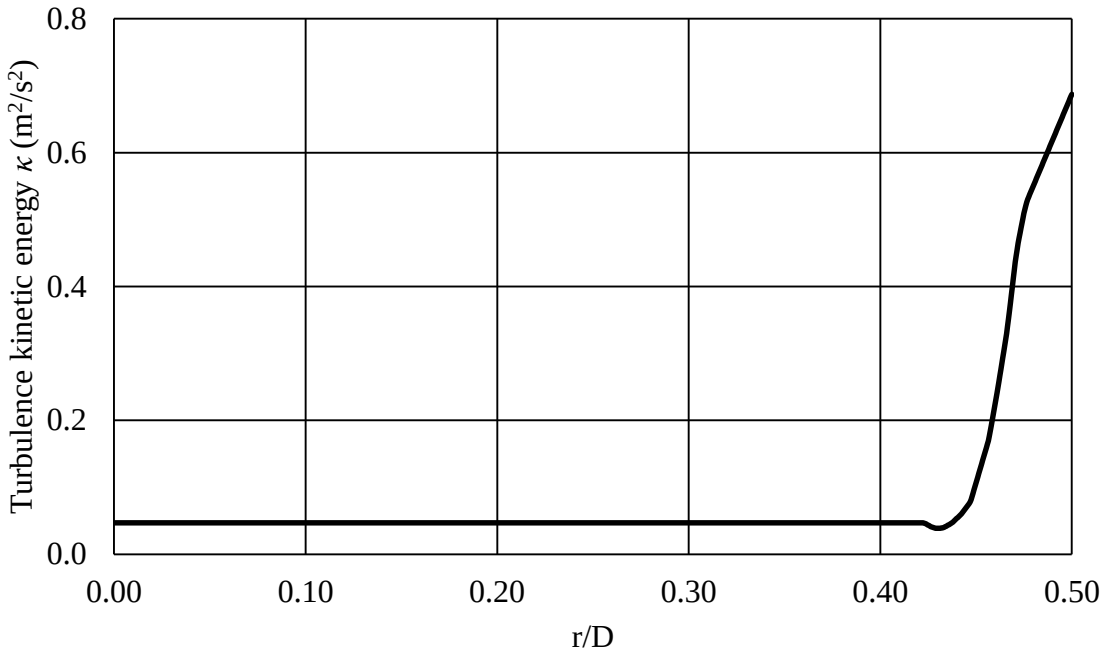

Fig. 2.3: Profile of the turbulence kinetic energy κ at the inlet section from Eq. (2.1). Post processed data from [9].

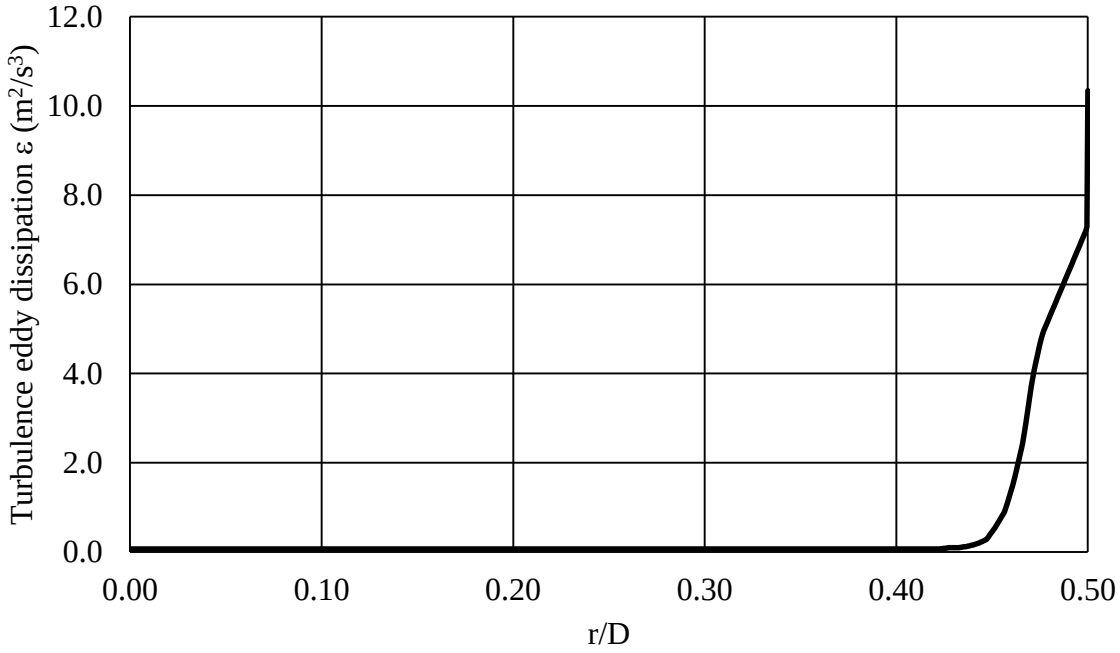

Fig. 2.4: Profile of the turbulence dissipation ε at the inlet section from Eq. (2.2).

2.3 Turbulence models

Five turbulence models were selected for evaluation by comparison with the swirl-flow experimental data of [9]. This selection was based on a number of factors. The κ-ε and κ-ω models were chosen because of their wide popularity (especially for the former) and because they have provided platforms for more refined models. The best of these refinements are conveyed by the *RNG* κ-ε and the *SST* κ-ω models. The aforementioned models, all two-equation models, are used in conjunction with the RANS turbulent-flow momentum equation. The last of the selected models, LES, is not related to the RANS equations and was chosen because of its different approach to turbulence modeling.

The steady-state, constant-property form of the RANS equations, written in Cartesian tensor form, is

$$\rho\left(u_i \frac{\partial u_j}{\partial x_i}\right) = -\frac{\partial p}{\partial x_j} + \frac{\partial}{\partial x_i}\left((\mu + \mu_t)\frac{\partial u_j}{\partial x_i}\right) \quad i = 1,2,3 \; and \; j = 1,2,3 \tag{2.3}$$

The quantity μ_t that appears in Eq. (2.3) is called the turbulent viscosity. It is a standard feature of all turbulence models that are connected with the RANS equations. The various models utilize different approaches to determining this quantity.

In what follows, turbulence-model equations (without buoyancy) for steady, constant-property flow are presented along with their sources and with explanatory notes when appropriate. A listing of the constants and coefficients that appear in the various models is provided after the presentation of the models.

2.3.1 $\kappa - \varepsilon$ Model

The κ-ε model [10] was the first two-equation turbulence model based on the RANS equations. The relationship between κ, ε and the turbulent viscosity μ_t is

$$\mu_t = C_\mu \rho \frac{\kappa^2}{\varepsilon} \tag{2.4}$$

where C_μ is a model constant. The governing equations for κ and ε are

$$\frac{\partial}{\partial x_i}(\rho u_i \kappa) = \frac{\partial}{\partial x_i}\left[\left(\mu + \frac{\mu_t}{\sigma_\kappa}\right)\frac{\partial \kappa}{\partial x_i}\right] + P_\kappa - \rho\varepsilon \tag{2.5}$$

$$\frac{\partial}{\partial x_i}(\rho u_i \varepsilon) = \frac{\partial}{\partial x_i}\left[\left(\mu + \frac{\mu_t}{\sigma_\varepsilon}\right)\frac{\partial \varepsilon}{\partial x_i}\right] + \frac{\varepsilon}{\kappa}(C_{\varepsilon 1} P_\kappa - C_{\varepsilon 2}\rho\varepsilon) \tag{2.6}$$

in which $C_{\varepsilon 1}$, $C_{\varepsilon 2}$, σ_κ, and σ_ε are model constants. The quantity P_κ is a turbulence production term due to viscous forces and is determined from

$$P_\kappa = \mu_t\left(\frac{\partial u_i}{\partial x_j} + \frac{\partial u_j}{\partial x_i}\right)\frac{\partial u_i}{\partial x_j} - \frac{\partial u_\kappa}{\partial x_\kappa}\left(3\mu_t \frac{\partial u_\kappa}{\partial x_\kappa} + \rho\kappa\right) \tag{2.7}$$

2.3.2 RNG $\kappa - \varepsilon$ Model

The RNG approach was developed in [11], where RNG stands for renormalized group. The equations are the same as the regular κ-ε model, but the model constants are different. The relationship between κ, ε and the turbulent viscosity μ_t is

$$\mu_t = C_{\mu RNG} \rho \frac{\kappa^2}{\varepsilon} \tag{2.8}$$

The dissipation transport equation with the new constants is

$$\frac{\partial}{\partial x_i}(\rho u_i \varepsilon) = \frac{\partial}{\partial x_i}\left[\left(\mu + \frac{\mu_t}{\sigma_{\varepsilon RNG}}\right)\frac{\partial \varepsilon}{\partial x_i}\right] + \frac{\varepsilon}{\kappa}(C_{\varepsilon 1RNG}P_\kappa - C_{\varepsilon 2RNG}\rho\varepsilon) \tag{2.9}$$

where

$$C_{\varepsilon 1RNG} = 1.42 - \frac{\eta\left(1-\frac{\eta}{4.38}\right)}{(1+\beta_{RNG}\eta^3)} \tag{2.10}$$

$$\eta = \sqrt{\frac{P_\kappa}{\rho C_{\mu RNG}\varepsilon}} \tag{2.11}$$

2.3.3 $\kappa - \omega$ Model

The $\kappa - \omega$ model [12] equations are of a similar form as the previous models, but the model constants are different. The relationship between κ, ω and the turbulent viscosity μ_t is

$$\mu_t = \rho\frac{\kappa}{\omega} \tag{2.12}$$

$$\frac{\partial}{\partial x_i}(\rho u_i \kappa) = \frac{\partial}{\partial x_i}\left[\left(\mu + \frac{\mu_t}{\sigma_\kappa}\right)\frac{\partial \kappa}{\partial x_i}\right] + P_\kappa - \beta_1\rho\kappa\omega \tag{2.13}$$

$$\frac{\partial}{\partial x_i}(\rho u_i \omega) = \frac{\partial}{\partial x_i}\left[\left(\mu + \frac{\mu_t}{\sigma_\omega}\right)\frac{\partial \omega}{\partial x_i}\right] + \alpha_1\frac{\omega}{\kappa}P_\kappa - \beta\rho\omega^2 \tag{2.14}$$

Here, α_1, β_1, β, σ_k, and σ_ω are model constants, and the quantity P_κ is a turbulence production term which is calculated in the same way as for the regular κ-ε model.

2.3.4 SST Model

The SST model [13] is a blending of the original κ-ε and κ-ω models. The models are known to respectively provide acceptable results away from bounding walls and in the neighborhood of bounding walls. They are blended to create the SST model. In this model the turbulent viscosity μ_t is given by

$$\mu_t = \frac{\alpha_1 \rho \kappa}{\max(\alpha_1 \omega, SF_2)} \tag{2.15}$$

in which

$$F_2 = tanh\left[max\left(\frac{2\sqrt{\kappa}}{\beta_1 \omega y}, \frac{500\mu}{\rho y^2 \omega}\right)\right]^2 \tag{2.16}$$

$$\frac{\partial(\rho u_i \kappa)}{\partial x_i} = \frac{\partial}{\partial x_i}\left[\left(\mu + \frac{\mu_t}{\sigma_{\kappa 3}}\right)\frac{\partial \kappa}{\partial x_i}\right] + P_\kappa - \beta_1 \rho \kappa \omega \tag{2.17}$$

$$\frac{\partial(\rho u_i \omega)}{\partial x_i} = \frac{\partial}{\partial x_i}\left[\left(\mu + \frac{\mu_t}{\sigma_\omega}\right)\frac{\partial \omega}{\partial x_i}\right] + 2\rho(1 - F_1)\frac{1}{\sigma_{\omega 2}\omega}\frac{\partial \kappa}{\partial x_i}\frac{\partial \omega}{\partial x_i} + \frac{\rho \alpha_3}{\mu_t} P_\kappa - \beta \rho \omega^2 \tag{2.18}$$

where F_1 is a blending functions given by

$$F_1 = tanh\left[min\left(max\left(\frac{\sqrt{\kappa}}{\beta_1 \omega y}, \frac{500\mu}{\rho y^2 \omega}\right), \frac{4\rho\kappa}{CD_{\kappa\omega}\sigma_{\omega 2} y^2}\right)\right]^4 \tag{2.19}$$

where y is the distance from a wall boundary, and

$$CD_{\kappa\omega} = max\left(2\rho\frac{1}{\sigma_{\omega 2}\omega}\frac{\partial \kappa}{\partial x_i}\frac{\partial \omega}{\partial x_i}, 10^{-10}\right) \tag{2.20}$$

2.3.5 LES (WALE) Model

The governing equations for the LES (WALE) model [14] are obtained from filtering the time-dependent Navier-Stokes equations. The filtering eliminates eddies smaller than the size of the physical mesh elements and uses an eddy viscosity approach for scales not directly solved for. This leads to Navier-Stokes equations taking the form

$$\frac{\partial}{\partial t}(\bar{\rho}\bar{u}_i) + \left(\frac{\partial \bar{\rho}\bar{u}_i\bar{u}_j}{\partial x_i}\right) = -\frac{\partial \bar{p}}{\partial x_j} + \frac{\partial}{\partial x_i}\left(\mu\left(\frac{\partial \bar{u}_i}{\partial x_j} + \frac{\partial \bar{u}_j}{\partial x_i}\right)\right) + \frac{\partial \tau_{ij}}{\partial x_i} \quad i = 1,2,3 \; and \; j = 1,2,3 \quad (2.21)$$

where τ_{ij} is the small-scale stress defined as

$$\tau_{ij} = -\overline{\rho u_\iota u_j} + \bar{\rho}\bar{u}_i\bar{u}_j = 2\mu_{sgs}\bar{S}_{ij} + \frac{1}{3}\delta_{ij}\tau_{kk} \quad (2.22)$$

and $\bar{S}_{ij}$ is the large-scale strain rate tensor. The small-scale eddy viscosity μ_{sgs} is found from

$$\mu_{sgs} = \rho(C_w\Delta)^2 \frac{\left(S_{ij}^d S_{ij}^d\right)^{3/2}}{\left(\bar{S}_{ij}\bar{S}_{ij}\right)^{5/2} + \left(S_{ij}^d S_{ij}^d\right)^{5/4}} \quad (2.23)$$

in which C_w is a constant and $\Delta = (element\ volume)^{1/3}$. The tensor S_{ij}^d can be written in terms of the strain-rate and vorticity tensors:

$$S_{ij}^d = \bar{S}_{ik}\bar{S}_{kj} + \bar{\Omega}_{ik}\bar{\Omega}_{kj} - \frac{1}{3}\delta_{ij}(\bar{S}_{mn}\bar{S}_{mn} - \bar{\Omega}_{mn}\bar{\Omega}_{mn}) \quad (2.24)$$

where the vorticity tensor $\bar{\Omega}_{ij}$ is defined as

$$\bar{\Omega}_{ij} = \frac{1}{2}\left(\frac{\partial \bar{u}_i}{\partial x_j} + \frac{\partial \bar{u}_j}{\partial x_i}\right) \quad (2.25)$$

Table 2.1
Dimensionless constants used for the turbulence models.

Model	Constant	Value
$\kappa - \varepsilon$	$C_{\varepsilon 1}$	1.44
	$C_{\varepsilon 2}$	1.92
	C_{μ}	0.09
	σ_{κ}	1.0
	σ_{ε}	1.3
$RNG\ \kappa - \varepsilon$	$C_{\varepsilon 2RNG}$	1.68
	$C_{\mu RNG}$	0.085
	β_{RNG}	0.012
	$\sigma_{\kappa RNG}$	0.7179
	$\sigma_{\varepsilon RNG}$	0.7179
$\kappa - \omega$	α_1	5/9
	β_1	0.09
	β	0.075
	σ_k	2.0
	σ_{ω}	2.0
SST	α_1	0.31
	α_3	4/5
	β_1	0.09
	β	0.075
	σ_{ω}	2
	$\sigma_{\omega 2}$	1/0.856
	$\sigma_{\kappa 3}$	1/0.85
LES (WALE)	C_w	0.5

2.4 Numerical Solutions

The numerical solutions for each of the five turbulence models were obtained by means of ANSYS-CFX 16.1 software. This package discretizes the governing partial differential equations by the finite-volume method to create algebraic equations. The mesh created for the final solutions of the governing equations consisted of approximately 6,875,700 nodes. Other meshes having different numbers of nodes were used in a mesh independence study to verify that the final mesh was sufficient to provide highly accurate results. The metric used in the mesh independence study was the overall pressure drop from the inlet to the outlet cross sections of the solution domain. When the solution was run with a grid consisting of 4.4 million nodes, the overall pressure drop differed by only 0.02% from that in which the grid contained 6.9 million nodes.

Representative views of the mesh are presented in Fig. 2.5. The diagram at the left shows the mesh at the inlet cross section and the dense nodal layer situated adjacent to the upper bounding wall of the straight duct. The right-hand diagram corresponds to a location near the opening boundary downstream of the conical diffuser.

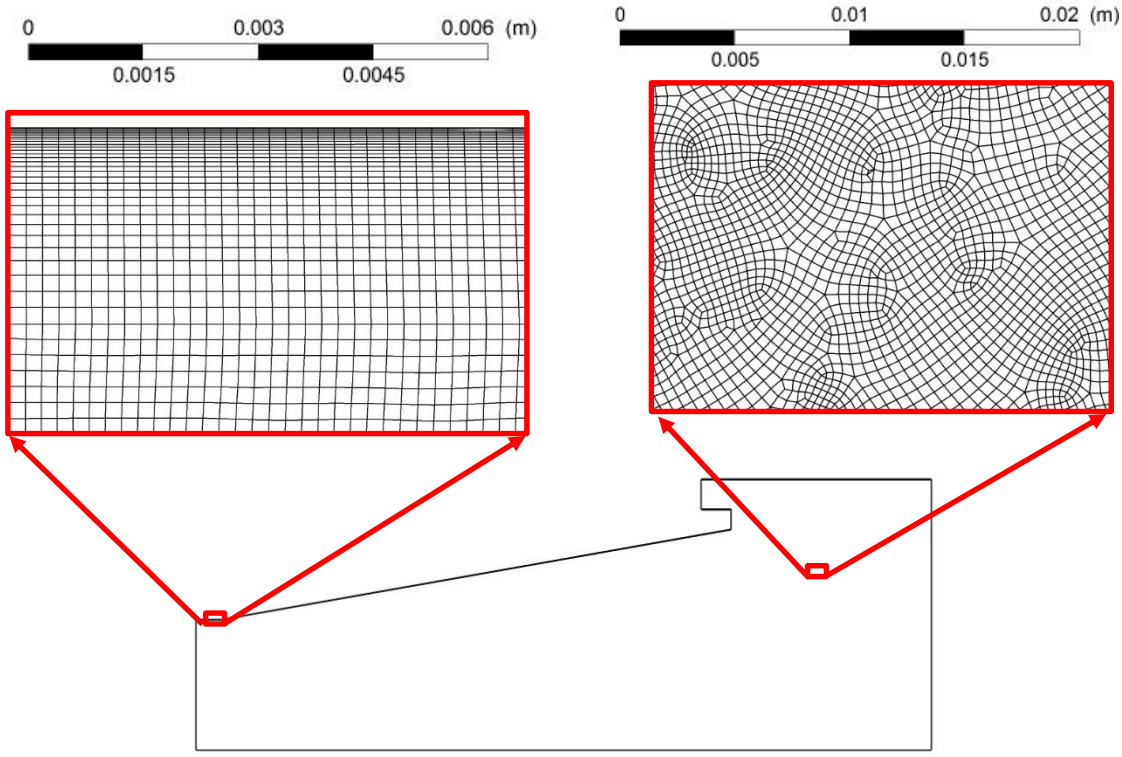

Fig. 2.5: Representative views of the computational mesh.

2.5 Results and Discussion

The focus of the presentation of results is the comparison of velocity profiles from the numerical simulations with those of the experimental data of [9]. These comparisons are displayed in Figs. 2.6-2.10, respectively for the κ-ε, *RNG* κ-ε, κ-ω, *SST* κ-ω, and *LES* models. Each of these figures has an (a) and (b) part. In part (a), comparisons are made between numerically predicted and experimental axial velocity profiles at selected streamwise locations. Similar comparisons are made in the respective (b) parts for the profiles of the circumferential velocity. The results of the numerical predictions are displayed by means of solid lines in the figures. In contrast, the experimental data are conveyed by circle and square symbols, respectively for the axial and circumferential velocity profiles.

Attention will first be turned to the predictions of the original κ-ε model and the corresponding experimental data. These results are displayed in Figs. 2.6(a) and (b), respectively for the profiles of the axial and circumferential velocities. In each of these figures, the dimensionless velocity profiles are plotted as a function of the dimensionless distance y/D from the wall of the diffuser at selected axial cross sections x at which experimental information is available.

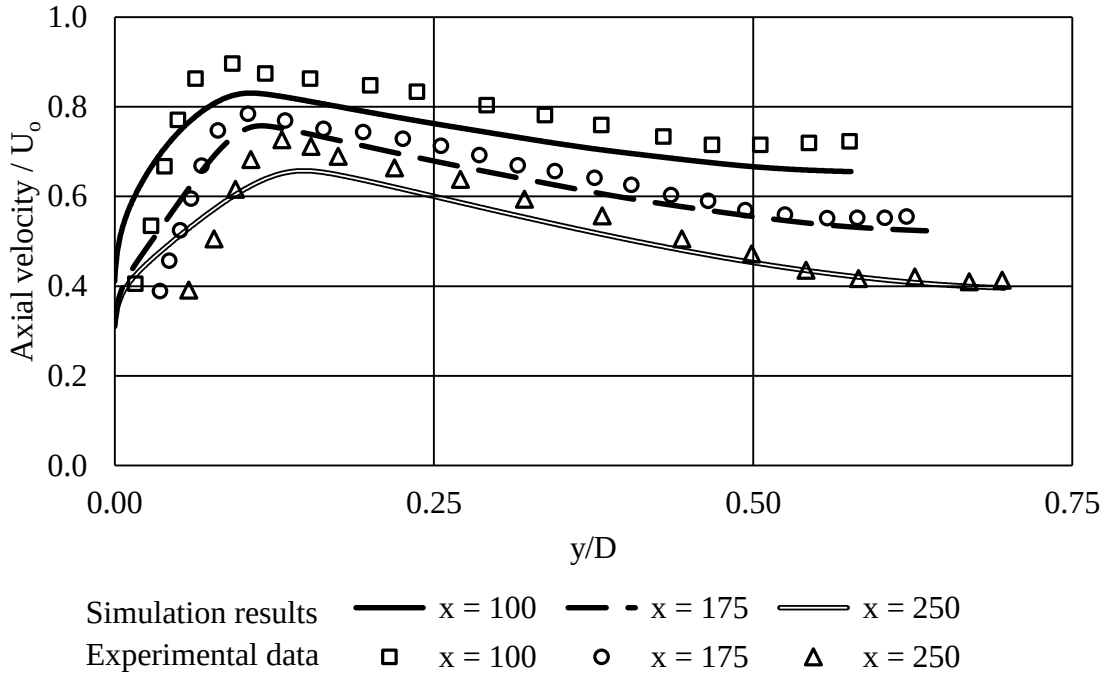

Fig. 2.6(a): Profiles of the axial velocity at selected cross sections in the diffuser. The curves depict the numerical results provided by the κ-ε turbulence model, and the discrete symbols are experimental data. The values of the axial coordinate *x* are in mm.

An overall view of all the results figures indicates that neither the numerical predictions nor the experimental data appear to fulfill the no-slip condition at the diffuser wall ($y = 0$). For the numerical simulations, the no-slip condition was properly imposed but the graphics package was unable to resolve the very rapid changes in the velocity in the near neighborhood of the wall. The near-wall velocity maxima are attributable to the low velocities that characterize the core of swirling flows.

Inspection of Fig. 2.6(a) shows significant disparities between the numerical results and the data for the axial velocity in the neighborhood of the wall, with the numerical solutions over predicting the data. In contrast, the numerical results significantly under predict the data over a substantial portion of the cross section at all three cross sections. In Fig. 2.6(b), which shows the circumferential velocity results, somewhat different deviations between the predictions and the data are in evidence. Near the wall, the predictions are low, whereas far from the wall they continue to be moderately low at the $x = 100$ mm location but are slightly high at $x = 405$ mm. All told, it appears that the κ-ε model does not handle the swirl situation very well.

Focus is now redirected to the predictions of the *RNG* κ-ε which are displayed in Figs. 2.7(a) and (b). When the results conveyed in those figures are compared with the counterpart Figs. 2.6(a) and (b), it is remarkable that the differences are so moderate. It would appear that the *RNG* κ-ε platform is not a suitable means for the obtainment of accurate predictions for flows with strong swirls.

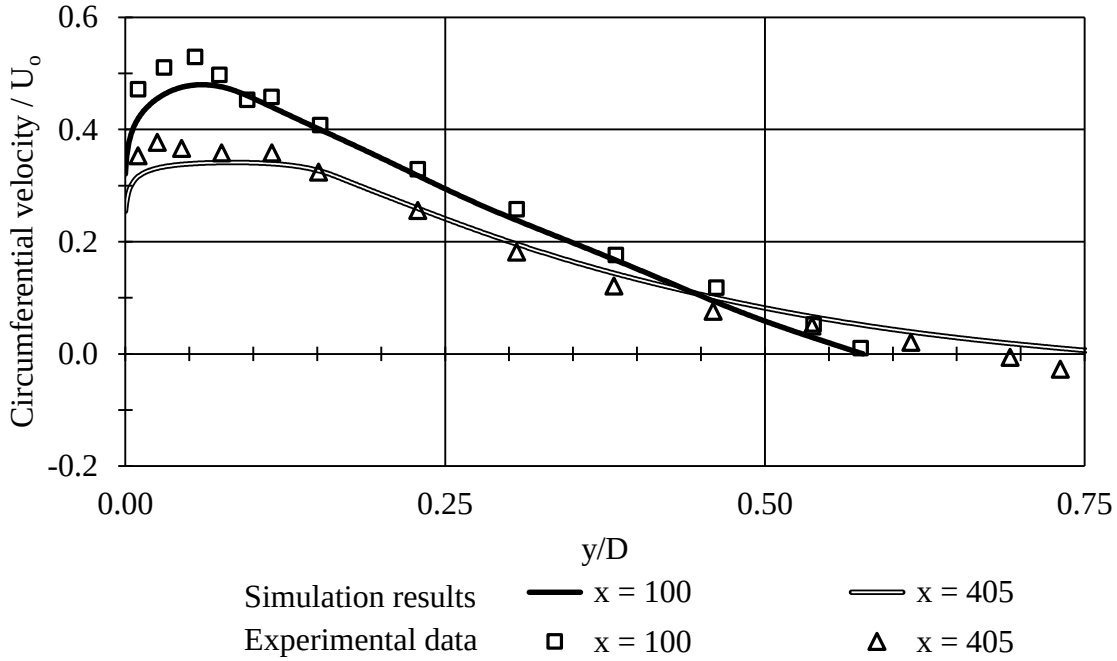

Fig. 2.6(b): Profiles of the circumferential velocity at selected cross sections in the diffuser. The curves depict the numerical results provided by the κ-ε turbulence model, and the discrete symbols are experimental data.

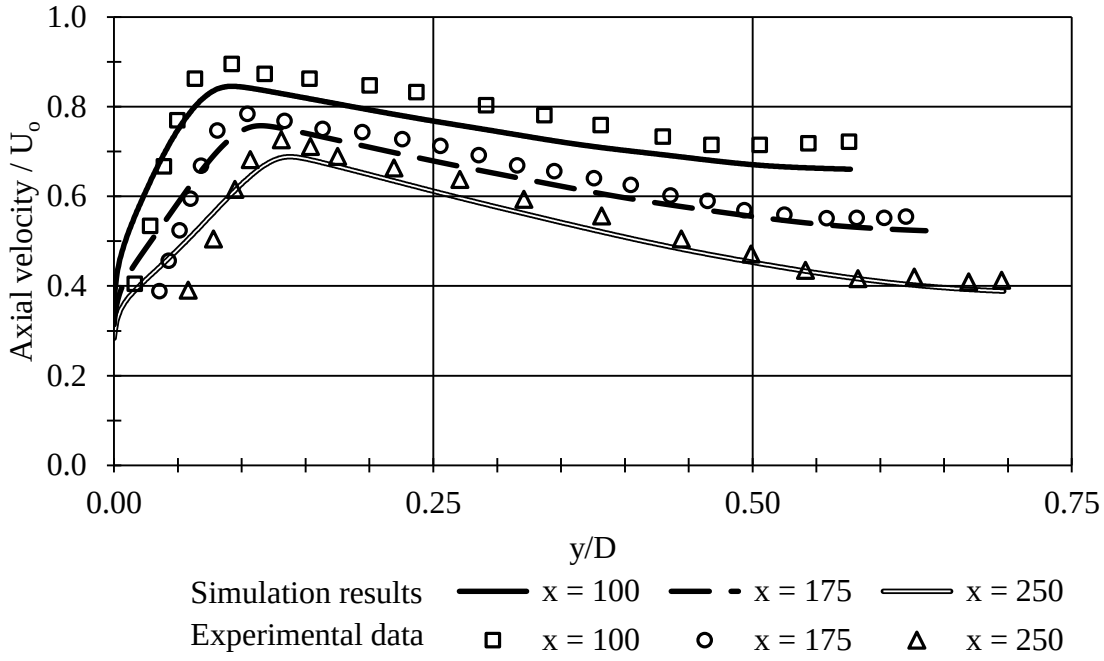

Fig. 2.7(a): Profiles of the axial velocity at selected cross sections in the diffuser. The curves depict the numerical results provided by the *RNG* κ-ε turbulence model, and the discrete symbols are experimental data. The values of the axial coordinate x are in mm.

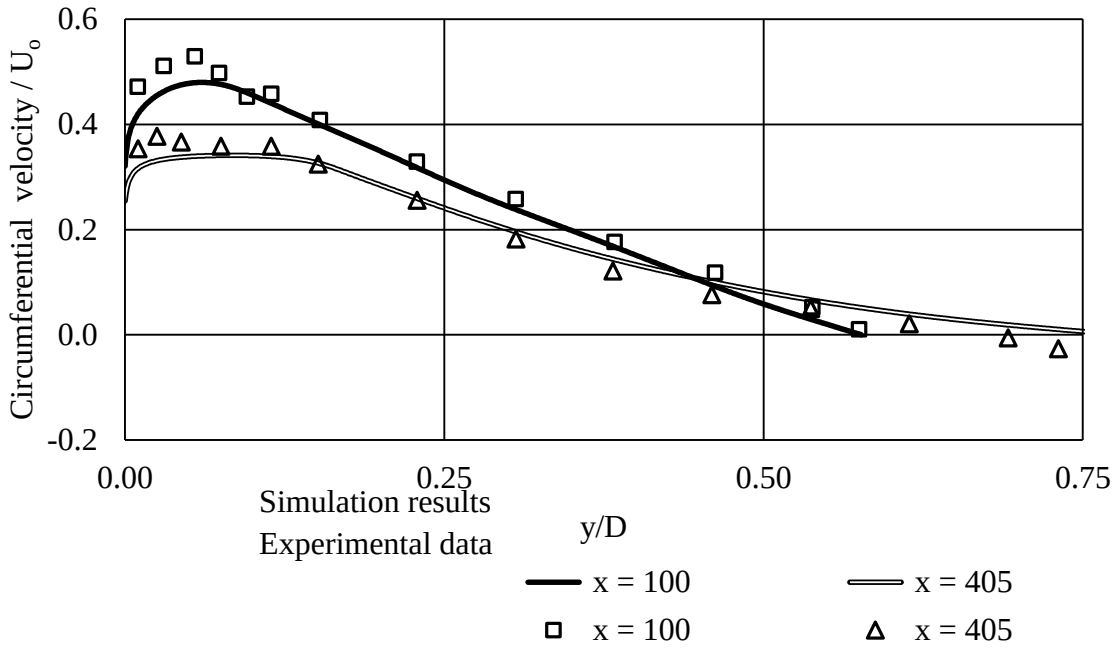

Fig. 2.7(b): Profiles of the circumferential velocity at selected cross sections in the diffuser. The curves depict the numerical results provided by the RNG κ-ε turbulence model, and the discrete symbols are experimental data.

Next, attention will now be directed to comparisons between the predictions of the original κ-ω model and the experimental data. These comparisons are made in Figs. 2.8(a) and (b), respectively for the axial and circumferential velocity profiles. From Figure 2.8(a), it is seen that there are large disparities between the numerical predictions and the data. These disparities are somewhat greater than those of Fig. 2.7(a) where the predictions were provided by the *RNG* κ-ε model. Near the wall, the prediction fall above the data, whereas away from the wall, the reverse relationship is in evidence. In Fig. 2.8(b), the deviations between the numerical predictions and the data for the circumferential velocity are more or less the same as were displayed in Fig. 2.7(b). Overall, it may be concluded that the original κ-ω model is somewhat less capable than the *RNG* κ-ε model as a means of dealing with swirling flows.

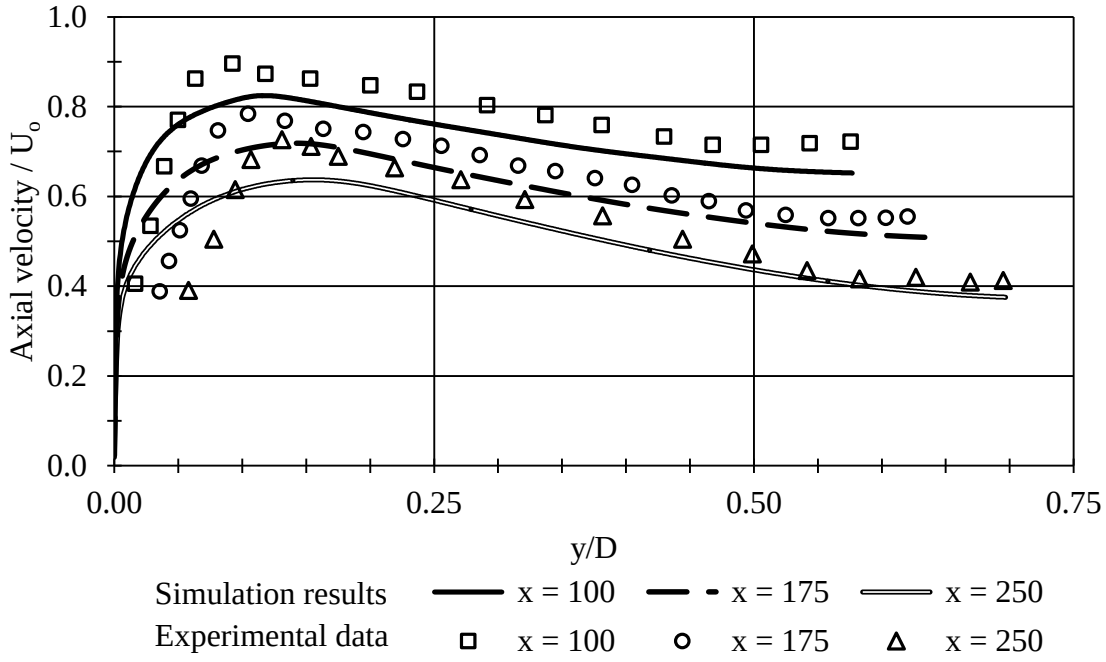

Fig. 2.8(a): Profiles of the axial velocity at selected cross sections in the diffuser. The curves depict the numerical results provided by the original κ-ω turbulence model, and the discrete symbols are experimental data.

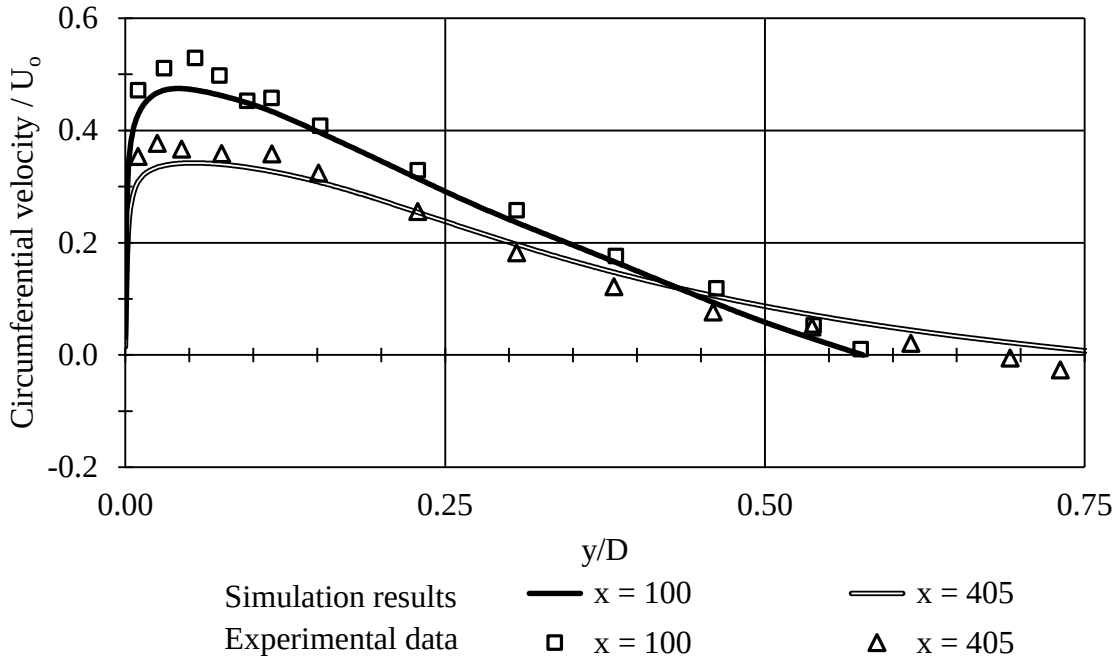

Fig. 2.8(b): Profiles of the conferential velocity at selected cross sections in the diffuser. The curves depict the numerical results provided by the original κ-ω turbulence model, and the discrete symbols are experimental data.

The next comparisons bring together the predictions of the *SST* κ-ω model and the experimental data. These comparisons are made in Figs. 2.9(a) and (b), respectively for the axial velocity profiles and the circumferential velocity profiles. In Fig. 2.9(a), it can be seen that the predictions are in very good agreement with the experimental data in the neighborhood of the wall, an achievement which eluded the other investigated turbulence models. The special importance of the near-wall accuracy of the *SST* κ-ω model is that heat transfer is especially sensitive to the near-wall velocities. Away from the wall, the *SST* κ-ω predictions are in better agreement with the data than are those of the other models. The comparisons shown in Fig. 2.9(b) also confirm the superior performance of the SST κ-ω model, especially in the neighborhood of the wall.

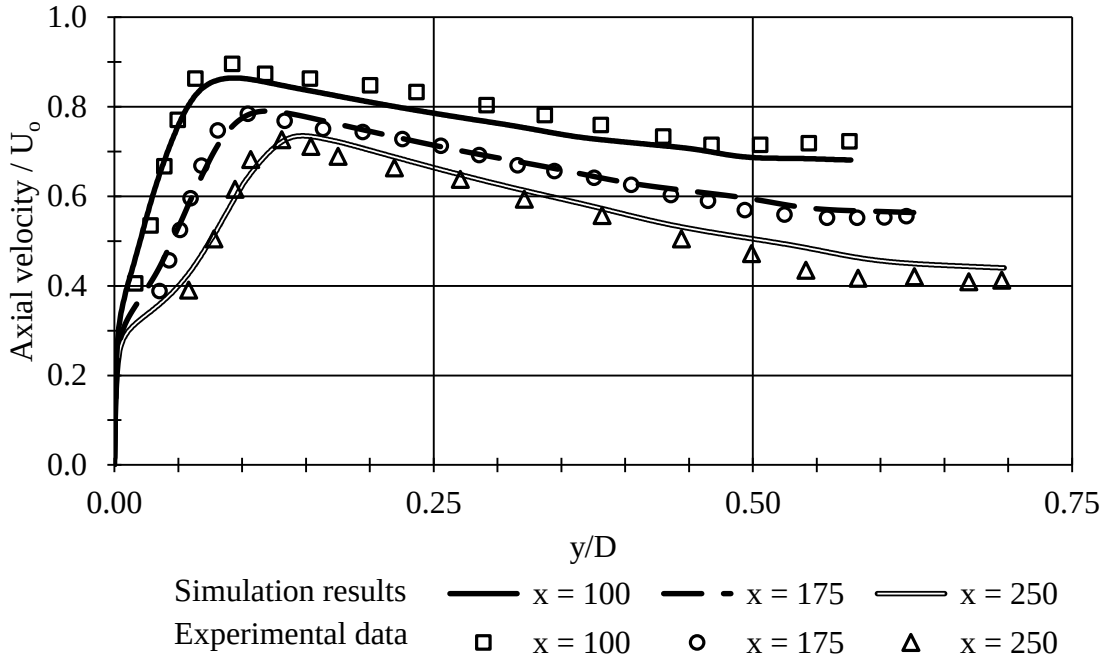

Fig. 2.9(a): Profiles of the axial velocity at selected cross sections in the diffuser. The curves depict the numerical results provided by the *SST* κ-ω turbulence model, and the discrete symbols are experimental data.

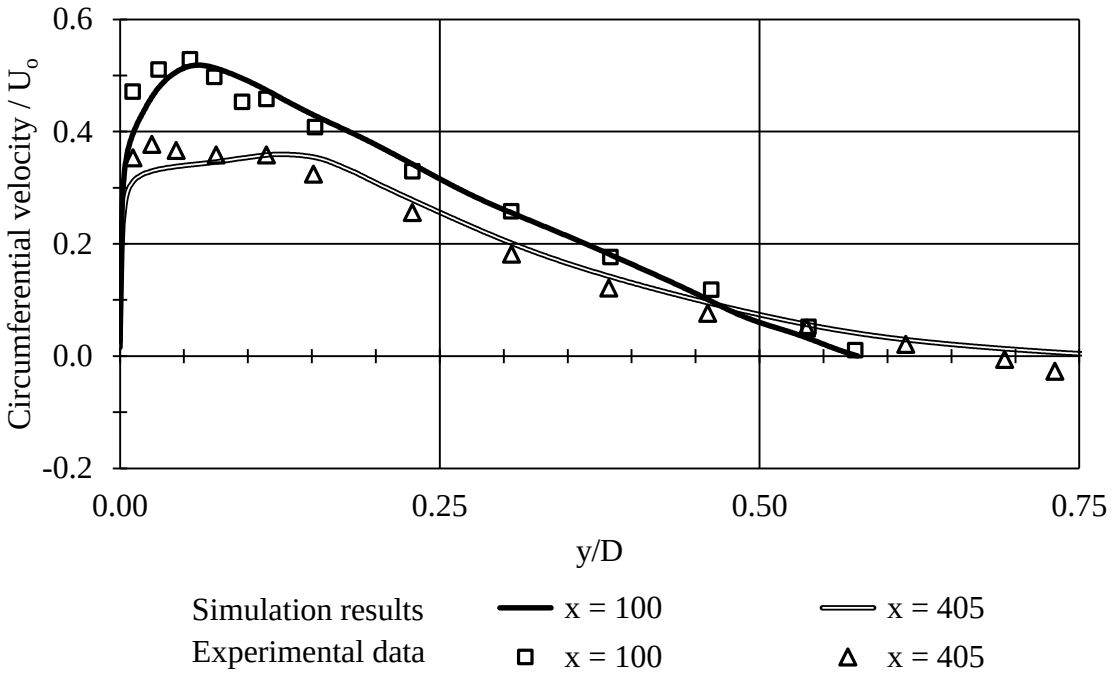

Fig. 2.9(b): Profiles of the circumferential velocity at selected cross sections in the diffuser. The curves depict the numerical results provided by the *SST* κ-ω turbulence model, and the discrete symbols are experimental data.

The last comparison between the experimental data and the results of the numerical simulation is made in Figs. 2.10(a) and 2.10(b) for the case in which the simulations were performed by mean of the LES turbulence model. That model is not a member of the category of two-equation turbulence models that were explored in the foregoing figures. Rather, the LES model is not based on isotropic turbulence nor on the RANS equations. It is widely regarded as a higher-order turbulence model compared with the RANS-based models. As was pointed out in the literature survey, the LES model requires extremely long computational times and extensive computing resources.

Inspection of Fig. 2.10(a) along with comparison with the best of the two-equation models, the SST κ-ω model, reveals a slightly better agreement of the LES predictions with the experimental results. This better agreement is modest. With regard to Fig. 2.10(b), the advantage of the LES predictions is even less than that already noted with regarded to Fig. 2.10(a). Another relevant fact is the comparison of CPU time needed to achieve SST κ-ω results compared with that required for the LES solutions. For the SST κ-ω model, the results were obtained in 14.2 days of CPU time compared to the 155.3 days of CPU time to obtain the LES results. It is deemed that the very moderate differences between the two sets of predictions is not worthy of the considerably greater time and recourses needed to execute the LES solutions.

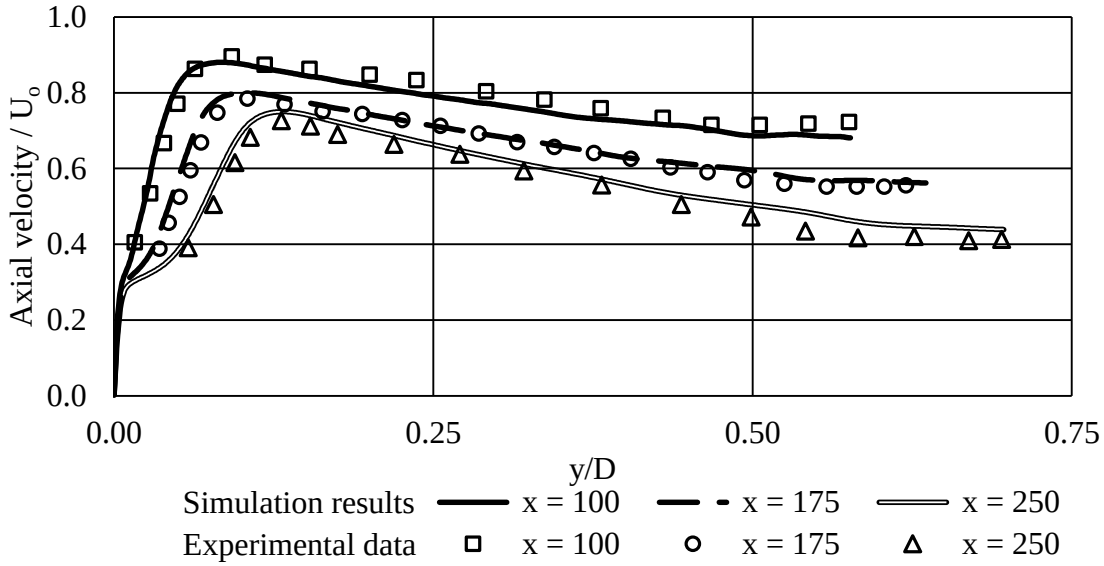

Fig. 2.10(a): Profiles of the axial velocity at selected cross sections in the diffuser. The curves depict the numerical results provided by the *LES (WALE)* turbulence model, and the discrete symbols are experimental data.

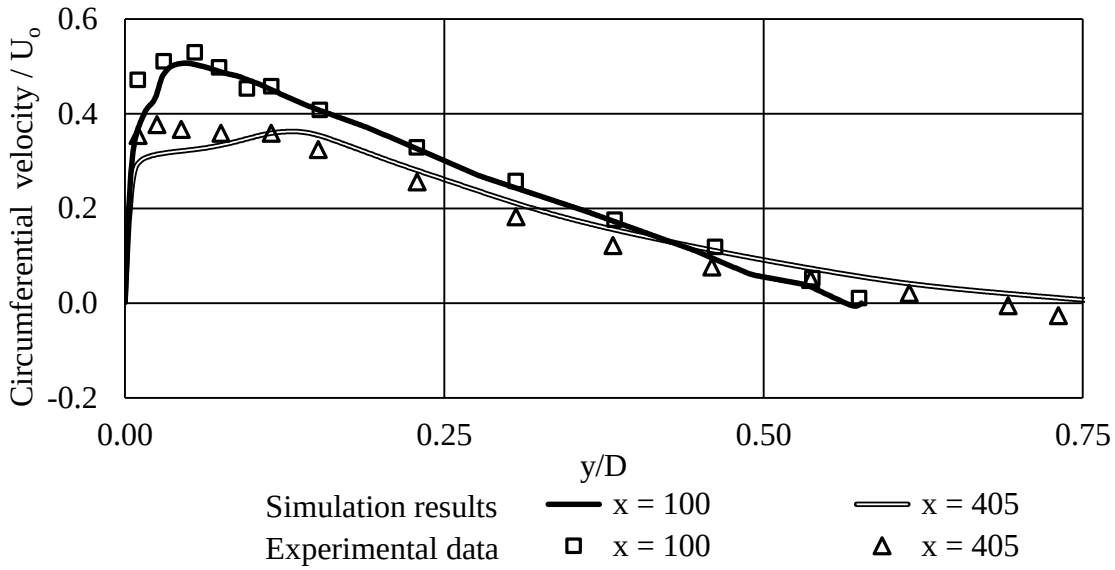

Fig. 2.10(b): Profiles of the circumferential velocity at selected cross sections in the diffuser. The curves depict the numerical results provided by the *LES (WALE)* turbulence model, and the discrete symbols are experimental data.

2.6 Retrospective Summary of Chapter 2

As engineering design is advanced by the use of numerical simulation, it is relevant to take steps to ensure the accuracy of its implementation. This matter is especially relevant since many of the applications practitioners are not well skilled in the optimal use of the numerical approach. There are two categories of issues to be considered: (a) numerical sufficiency of the discretization and (b) modeling of the physical situation. In the first category is mesh quality which relates to the number of nodes used in the discretization. Another issue in the same category is the convergence criterion required to define an acceptable solution. Still another is the "word length," which relates to the number of significant figures used for the actual calculations. These issues can be more readily dealt with than are modeling issues.

In the modeling category, the issue of the fidelity of the simulation model to the actual physical situation is the key matter. Since the majority of real-world, fluid-flow applications are turbulent, the use of the most appropriate turbulence model is most relevant. Rather than interrogate each separate application with respect to the most appropriate turbulence model, the approach taken here is to focus attention on a category of fluid flows within which there are a number of significant specific applications. The category selected for study here is flows with swirl. This selection reflects the authors' interest in rotating-fan-supplied flow to heat exchangers, bends in which fluid rotation is intrinsic, combustion, rotating machinery, and others.

In this investigation, turbulence models which are readily available in commercial packages and which can be implemented on moderate-capacity computers have been selected for study. These are generally well-known, two-equation models and are often classified as RANS-based models. In addition to those turbulence modes, the LES model was also used to obtain a set of solutions. The LES model is a higher-order model which is not in the RANS category and does not assume that the turbulence is isotropic.

The evaluation methodology was based on comparing velocity profile predictions based on the selected models with those of a highly comprehensive experimental study from the published literature. The special feature of that study is the completeness of the quantitative description of the turbulence at the inlet of the experimental apparatus.

It was found that among the investigated two-equation turbulence models, the *SST* κ-ω model predicted axial and circumferential velocity profiles that agreed best with those of the experiments. Of particular relevance with respect to heat transfer is that the *SST* κ-ω predictions of the velocities near the wall of the apparatus were especially excellent compared with the predictions of the other models. Since convective heat transfer is very sensitive to the near-wall velocity field, this finding augurs well for the determination of heat transfer predictions in swirl-flow situations when the *SST* κ-ω is used. The velocity profile predictions obtained from the LES turbulence model were slightly in better agreement with the experimental data than were those from the SST κ-ω model. However, there was an enormous difference in the CPU time required to obtain a solution by use of these respective methods. The CPU time needed for the LES solution was 155.3 days. By comparison, only 14.2 days of CPU time were required for the SST κ-ω solution. In this light, it is believed that is the SST κ-ω model is the most efficient of those investigated.

Chapter 3

EFFECT OF FAN-GENERATED SWIRL: APPLICATION TO HEAT TRANSFER IN A DNA SAMPLING DEVICE

3.1 Introduction

Present medical and forensic practice makes great use of the nature of DNA samples. Consequently, there has been considerable effort to device and perfect equipment that increases the rapidity by which DNA samples are processed and which leads to outcomes of higher accuracy. The equipment that most favored by both medical and forensic professionals is thermocyclers. That equipment subjects DNA samples to a protocol which defines a temperature variation between prescribed upper and lower bounds at a chosen frequency. Multiple DNA samples are processed simultaneously with each sample contained in a vial which, in turn, is situated in a recess in a large block. The temperature cycling creates a Polymerize Chain Reaction (PCR). Enzymes are introduced into the respective DNA samples to facilitate the uncoiling of the DNA helix.

Temperature control is crucial to the success of the DNA evaluation. Control is achieved by separate heating and cooling processes. A number of heating means are presently employed. For the heating part of the thermal cycle, current modalities include thermoelectric chips, electrical resistive heating, convection, and induction. In contrast, the cooling process is performed in a unique manner in all of the present equipment. That cooling is carried out in a finned heat exchanger for which air is the coolant. That heat exchanger is often referred to as a heat sink. Although considerable attention has been paid to the various heating modalities, it appears that a cooling phase of the operation of the equipment has never either been analyzed in the laboratory or by numerical simulation. A lack of knowledge of the performance of the finned heat exchanger has made it impossible to create a highly efficient, rational design of the thermocycler.

The absence of any substantive work relating to the heat sink seems not to have any explanations in the published literature. One possible explanation is that the researchers involved with the overall process are not knowledgeable about heat transfer design and analysis.

In current design practice, two powerful tools are available: laboratory experimentation and numerical simulation. It has been the experience of the author that there are distinct benefits when the simulation is performed first and the experimentation later. A main reason for this conclusion is that the predictions of the simulations can provide considerable guidance for the formulation of a fruitful experimental protocol. The reverse has not yielded as rich a harvest of results because experimentation cannot provide results to the same degree of detail as can numerical simulation. It is in this light that it was deemed proper to develop a highly detailed numerical simulation as the first step in attacking a problem that has never before seen other qualitative, Edisonian approaches.

A literature search did not prove to be highly fruitful because the majority of the work on thermocyclers is guarded intellectual property by companies competing for market share in a market whose medical and forensic involvements are expected to grow enormously.

The only open-literature publication that was found to pay any heed to heat sink issues is due to Zhang [15]. The envisioned cooling mode was to blow air into the fin array through the plane of the fin tips. However, the stated model was for air blown longitudinally in the direction of the fin length. More to the point, the totality of the analysis consisted of stating the oversimplified solution for the longitudinal fin case taken directly from undergraduate heat transfer texts. That solution is not only inappropriate and incorrect, it is rife with incorrect assumptions. No quantitative use was made of that solution.

Other open-literature publications identified by the author did not include any issue relevant to the present work. In [16], heating was accomplished by thermoelectric modules but no attention was paid to the heat sink. The issue of the time required for the processing

of the DNA was the focus of [17]. To reduce the time taken to complete a DNA analysis, a hybrid control was designed to rapidly track the thermal cycling protocol. Fins are pictured but not analyzed. As an alternative to either thermoelectric or resistive heating, the use of induction heating was proposed and evaluated [18]. The heat-sink role of fins was not identified. As a different alternative to conventional heating methods, convectively driven-closed loop thermocycling was set forth as a rapid inexpensive and simplified approach to ameliorate lengthy time scales and extensive energy requirements [19].

In some thermocyclers, the block housing the vials of DNA is configured to be isothermal. On the other hand, [20] has proposed that the block housing the vial samples be subdivided into separate segments, with each segment thermally decoupled from the others. Another proposal suggested [21] the use of automation to enable the reaction to be carried out simultaneously for many vials and thereby to produce precise results. The invention set forth in [22] relates to continuous flow systems, particularly to thermocyclers for the automated and continuous cycling. A control system is set forth in [23] for the heating or cooling of many samples in order to maintain a uniform specific temperature for an extended period of time. Many thermocyclers are based on the principle of temperature uniformity in the block housing the vials of DNA. To this end, [24] proposed the use of a second heat source as a means for maintaining the temperature of the vial block as uniformly as possible.

The foregoing literature review has established the absence of heat transfer knowledge with regard to the cooling portion of the thermal cycle that is inherent in the DNA analysis device. The goal of the research to be described here is to perform the first step of such an analysis utilizing the method of numerical simulation.

3.2 Physical Model

To introduce the physical situation to be analyzed here, it is convenient to turn attention to Fig. 3.1. That figure is an enhanced CAD drawing of a prototypical DNA analysis device. The actual functional components are contained within the casing displayed in the figure. In normal operation, the device is commonly situated on a table top with an airspace between the base of the device and the table. As indicated by the callout vectors, air is drawn from the surroundings through the airspace into the functional part of the device. After the airflow has passed through the appropriate components in the device, it exits into the environment thorough grills which form the front and back faces of the casing of the device. Situated atop the casing is an aluminum block which contains carefully machined perforations, each of which houses a vial of the sample being analyzed. That block is heated by thermoelectric modules situated beneath the block but are hidden in the figure.

A front-face view of the device is displayed in Fig. 3.2. Through the openings of the grill, a structure is visible which can be identified as the heat transfer fins whose purpose is to cool the airflow. Also seen in the figure is the temperature-controlled aluminum block and the clear space beneath the device through which air enters it. Of particular relevance to the solution methodology to be applied here is a large rectangular enclosure which bounds the device. That enclosure defines the volume in which the solution will be sought. It is commonly designated as the solution domain.

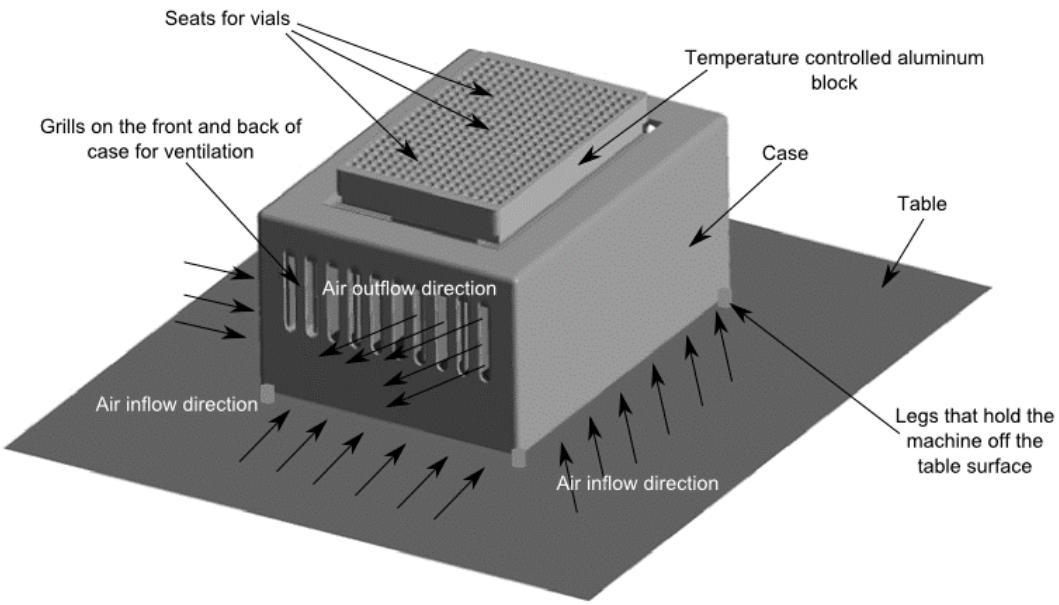

Fig. 3.1: Enhanced CAD drawing of a prototypical DNA analysis device.

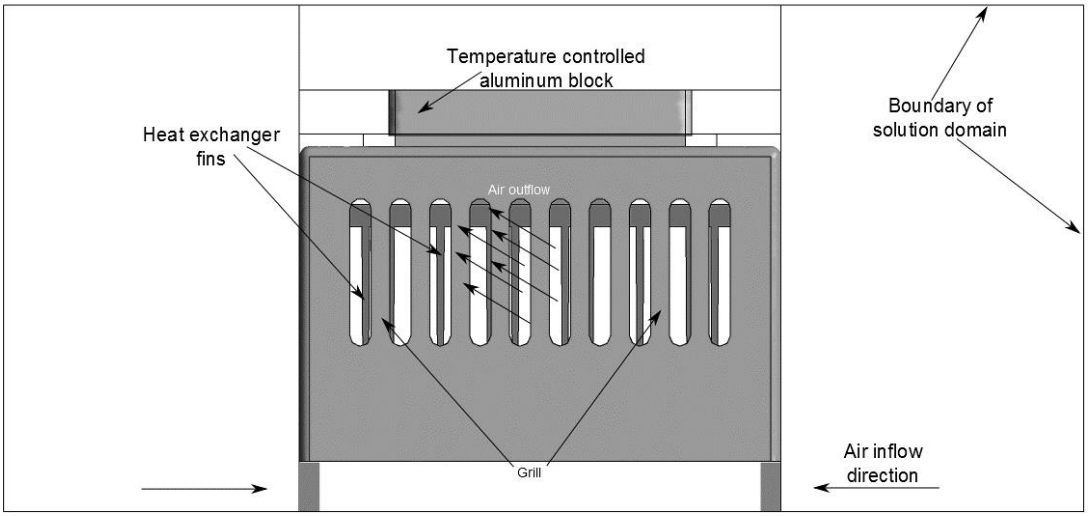

Fig. 3.2: Front face view of the device.

The configuration of the functional components of the device are shown in Fig. 3.3. By observing the figure from bottom to top, the encountered elements are the table top, a clear space through which air is drawn, the housing of the fluid mover which draws air into the interior of the device, the air that flows from the fluid mover through the fin array. The fin array consists not only of an assemblage of 16 fins but includes a base plate which is integral to the fins. Directly atop the base plate is thermoelectric module which functions as a heater. To ensure that the thermal energy provided by the module is uniformly distributed, an aluminum block serves as a heat spreader. The uppermost component is the temperature controlled block whose upper portion houses the seats for the specimen vials.

An alternative view of the components that were displayed in Fig. 3.3 is presented in Fig. 3.4. The latter is a side view. The succession of components, from bottom to top, is the same as that of the preceding figure. Of particular note in Fig. 3.4 is the direction of the air that is discharged from the finned heat exchanger. When it is recognized that the air enters the interfin spaces from below and exits from the respective ends of the array, it can be surmised that the air executes a 90º turn. In this figure, the heat exchanger is represented by the outboard fin in the array.

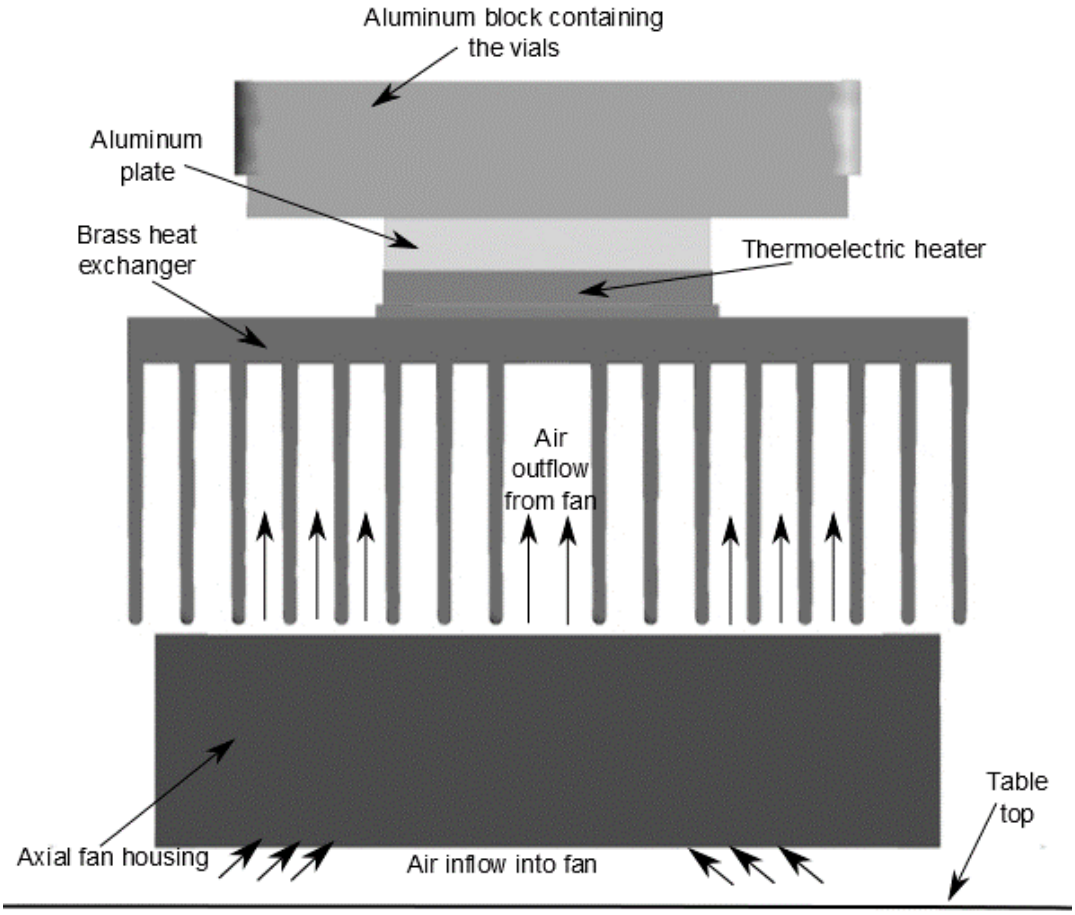

Fig. 3.3: Configuration of the functional components of the device.

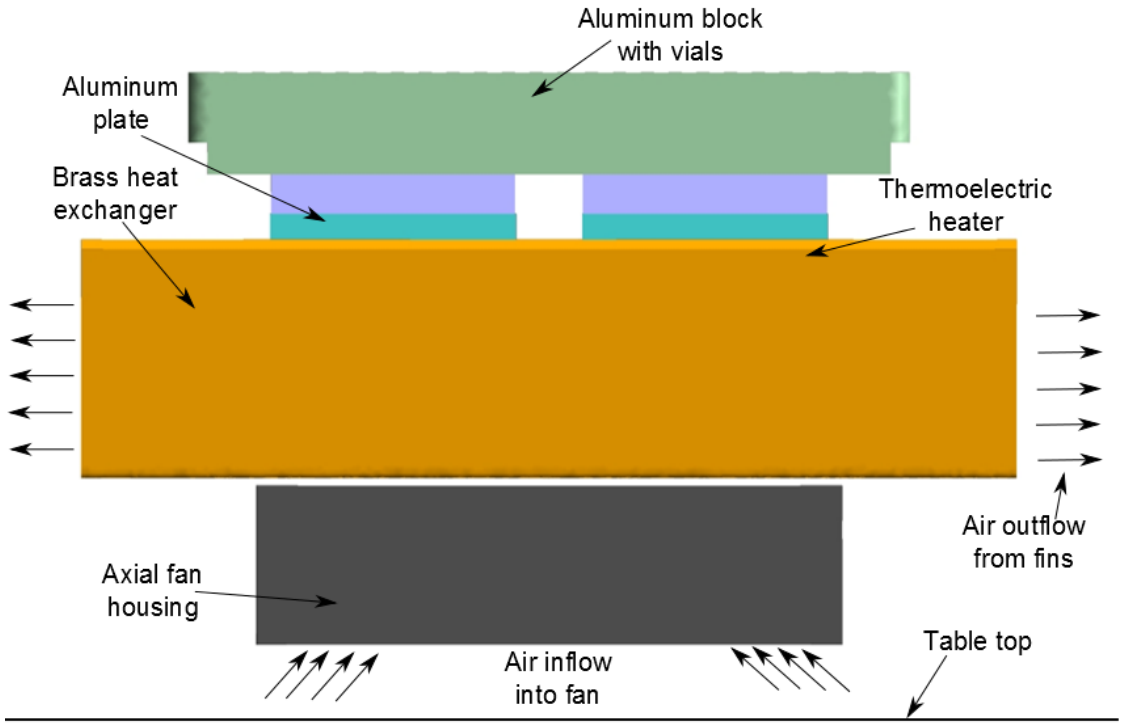

Fig. 3.4: Side view of the configuration of the functional components of the device.

The next figure, Fig. 3.5, is focused on the fluid mover and its relationship to the fin array. The figure is a view from below looking upwards toward the fan and at the fin array as seen through the openings of the fan. The type of fan in question is termed a muffin fan. The standard design includes a square frame which envelops a circular opening which contains the blades and the hub to which the blades are attached. The hub normally houses a motor (usually DC).

The fin array can be identified by the succession of ridges which represent the fin tips. The spaces between the fins are flow passages.

Focus will now be shifted from a bottom vantage point looking upward to a top vantage point looking downward. Such a top down orientation gives rise to the view displayed in Fig. 3.6. The inner rectangle is a plan view of the heated aluminum block which houses the sample vials. Seen in the figure are the perforations in which the vials are housed. The larger rectangle is the base plate to which the fins are attached.

The internal components of the device are presented pictorially in Fig. 3.7. Seen there is the table top, fan housing, heat exchanger, and temperature controlled aluminum block.

The next two figures are included to convey the dimensions that pertain to the model that was employed in the numerical simulations. Figure 3.8 is a head-on view of the face of the fan. The depth of the fan in the direction perpendicular to the page is 2.59 cm.

The final figure in this series, Fig. 3.9, is concerned with the dimensions of the fin array. As can be seen in the figure, there are 16 fins and 15 interfin spaces which constitute the passages through which the coolant air flows. The fin length-to-thickness ratio, which is a key dimensional characterization of fins, is approximately 18. The depth of the array is 15.24 cm.

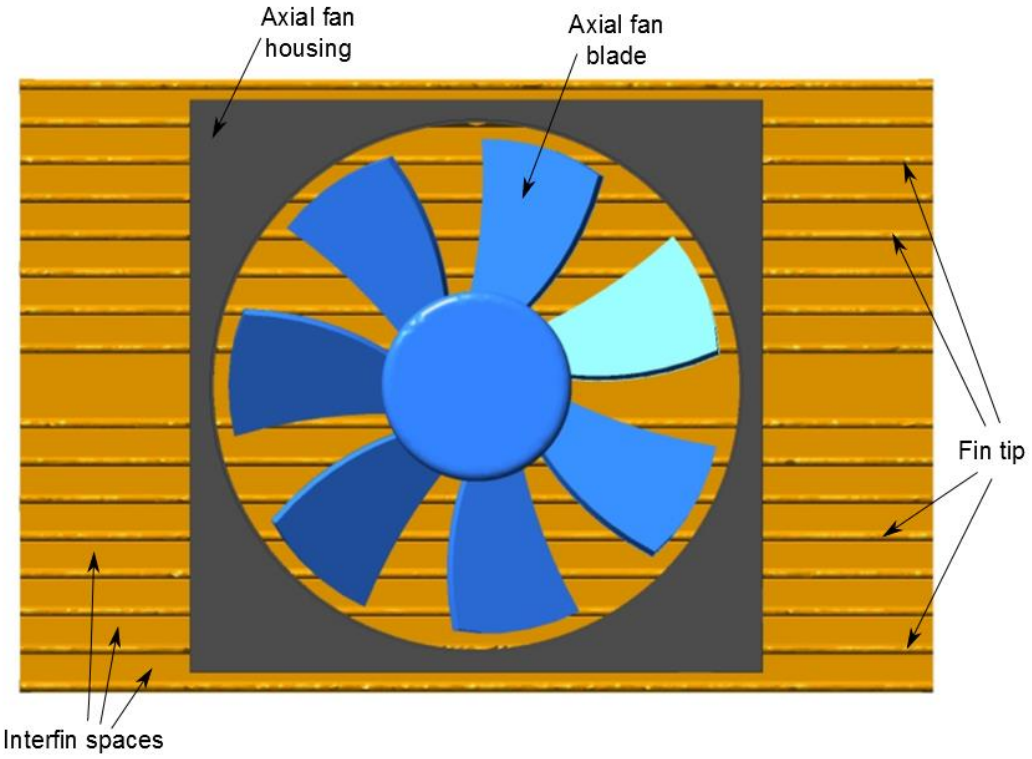

Fig. 3.5: Fluid mover and its relationship to the fin array.

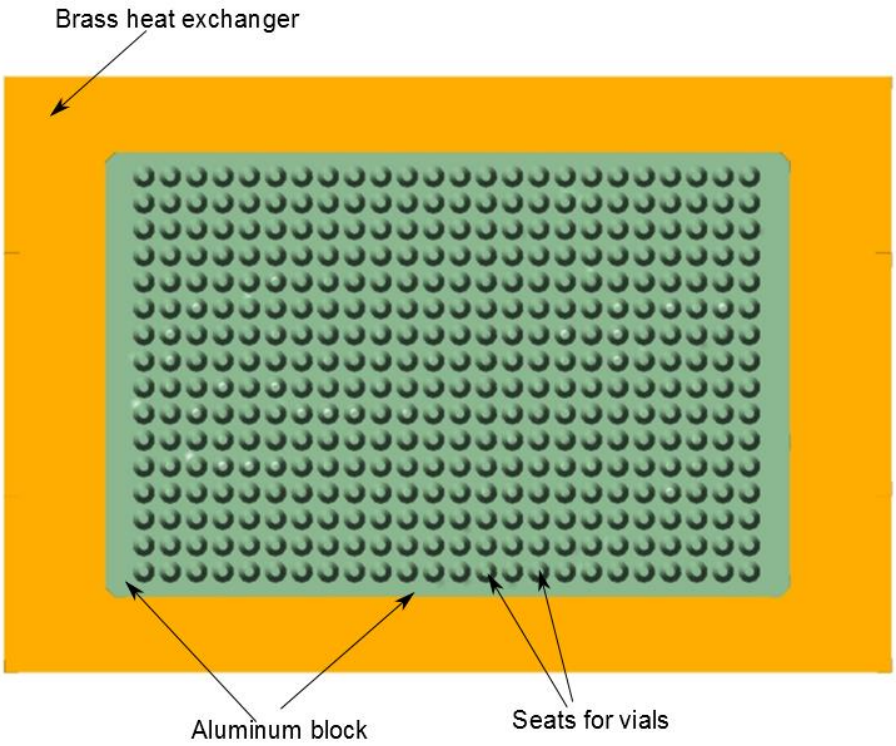

Fig. 3.6: Plan view of the sample-housing block and the base plate of the heat exchanger.

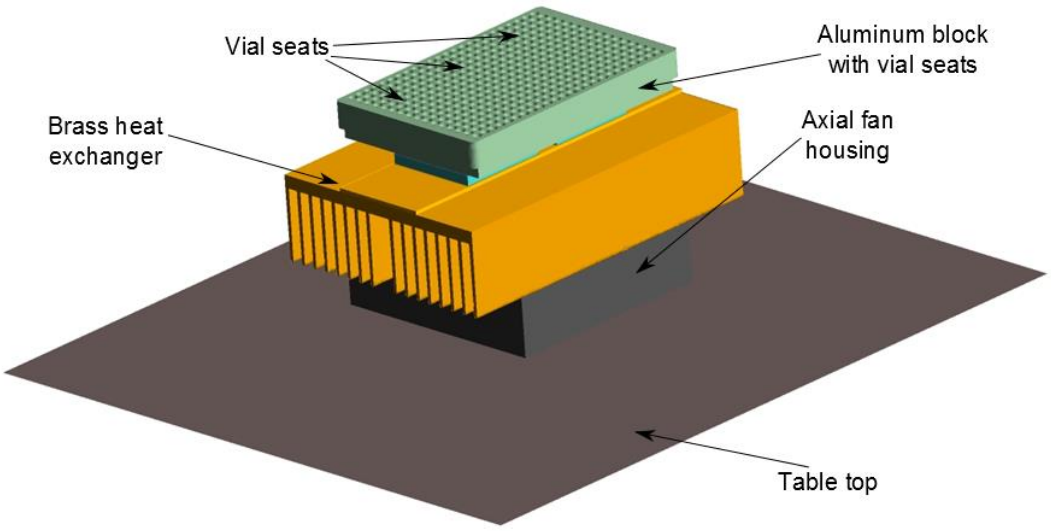

Fig. 3.7: Pictorial view of the internal components of the device.

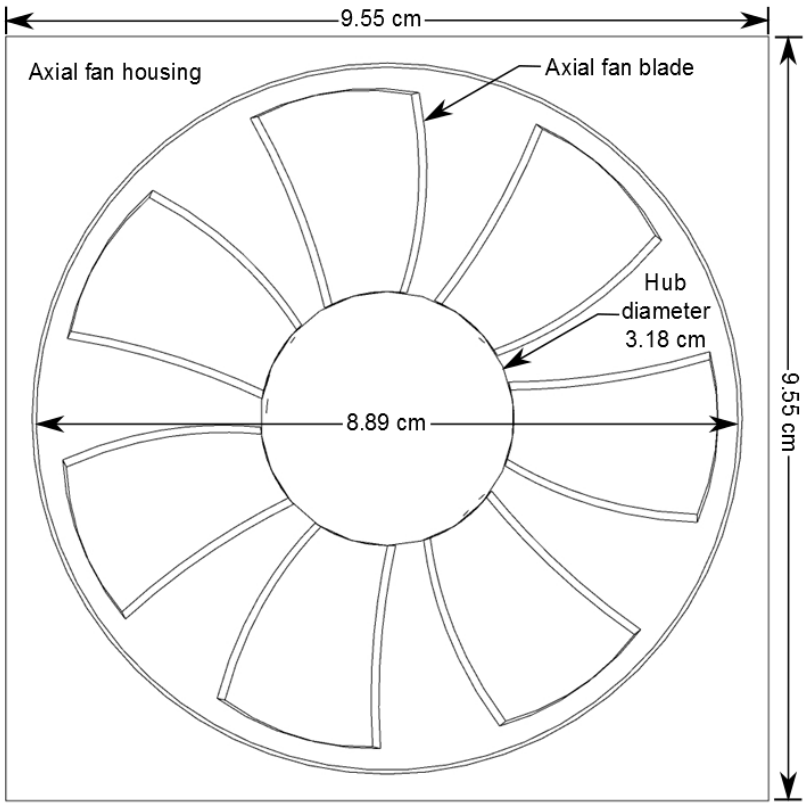

Fig. 3.8: Head-on view of the face of the fan displaying dimensions.

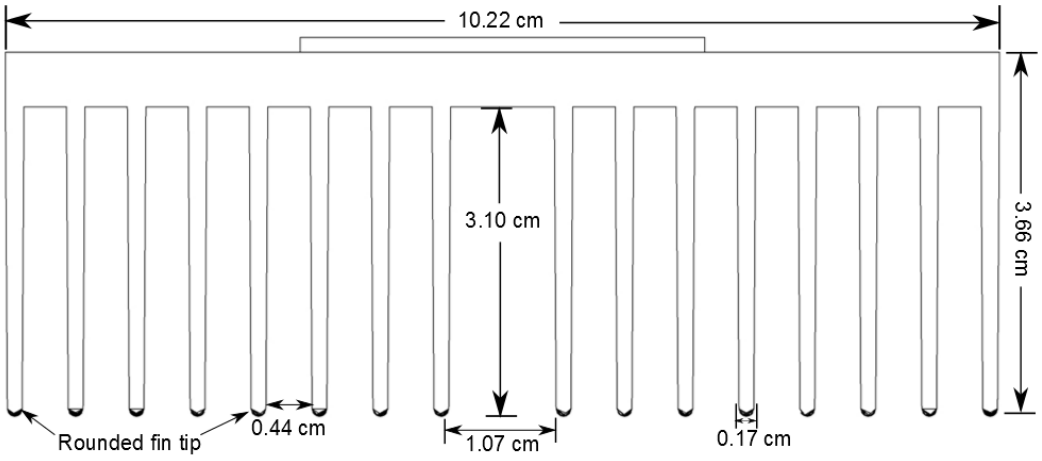

Fig. 3.9: Dimensions of the fin array.

3.3 Mathematical Model

3.3.1 Fluid Flow

The state of the fluid flow passing through the device is expected to be turbulent. As a consequence, the conventional Navier-Stokes equations which represent Newton's Second Law for flowing fluid are not directly applicable. As an alternative, use is frequently made of the Reynolds-Averaged Navier-Stokes equations.

The link between these two sets of equations is the decomposition of a velocity component u_i(x,y,z,t) into a time-averaged part $\overline{u_i}$(x,y,z) and a fluctuating part u_i'(x,y,z,t). When this decomposition is introduced into the conventional Navier-Stokes (N-S) equations and a time-averaging operation is performed, some terms that have no counterparts in the N-S equations appear. Those terms are normally termed the Reynolds stress terms.

At this point, a model attributed to Boussinesq is introduced whereby each of the Reynolds stress terms is set equal to a form that resembles the stress-viscosity relation for a Newtonian fluid. The Boussinesq suggestion was to replace the conventional molecular viscosity μ with a so-called turbulent viscosity μ_{turb}. This reasoning resulted in the replacement of the Reynolds stress by terms involving μ_{turb}. The equations that emerge from these manipulations is displayed below.

$$\rho\left(u_i \frac{\partial u_j}{\partial x_i}\right) = -\frac{\partial p}{\partial x_i} + \frac{\partial}{\partial x_i}\left((\mu + \mu_{turb})\frac{\partial u_j}{\partial x_i}\right) j = 1,2,3 \; i = 1,2,3 \qquad (3.1)$$

In these equations, the participating fluid properties are the density ρ and the viscosity μ. The three velocity components are represented by u_i and the coordinates by x_i.

Whereas Newton's Second Law for a fixed mass system embodies the condition that mass is conserved, the Second Law for a flowing fluid does not. As a consequence, a separate statement of mass conservation is needed for fluid flow as follows

$$\frac{\partial u_i}{\partial x_i} = 0 \tag{3.2}$$

The quantity μ_{turb} is not a physical quantity but a construct of convenience. It is necessary to find ways to determine it. The history of the various approaches to the determination of μ_{turb} extends over a century. A breakthrough occurred in 1972 when Launder and Spalding [10] created a turbulence model involving the turbulence kinetic energy κ and the turbulence energy dissipation ε. They created governing equations containing advection, diffusion, and source/sink terms. Their model is identified as the κ- ε model. That model contained five tunable constants whose numerical values were determined from experimental data. Numerous enhancements extending over a period of about 40 years have led to a plethora of two-equation models. These later models contain many features that enable more accurate predictions to be made of fluid flow phenomena based on their use. Despite these advances, the original κ-ε model remains as the most used two-equation turbulence model.

Among the latter-day turbulence models, the Shear Stress Transport model (SST) that was formulated by Menter [13] in 1994 has been shown to provide numerical simulation results that are well supported by experimental data, as shown in Chapter 2, especially for fluid flows that encompass swirl. In addition, it is the only turbulence model that reduces to laminar flow when the actual flow is in the laminar regime. The SST model has been adopted here. The relevant equations are

$$\frac{\partial(\rho u_i \kappa)}{\partial x_i} = P_\kappa - \beta_1 \rho \kappa \omega + \frac{\partial}{\partial x_i}\left[\left(\mu + \frac{\mu_{turb}}{\sigma_\kappa}\right)\frac{\partial \kappa}{\partial x_i}\right] \tag{3.3}$$

$$\frac{\partial(\rho u_i \omega)}{\partial x_i} = A\rho S^2 - \beta_2 \rho \omega^2 + \frac{\partial}{\partial x_i}\left[\left(\mu + \frac{\mu_{turb}}{\sigma_\omega}\right)\frac{\partial \omega}{\partial x_i}\right] + 2(1 - F_1)\rho \frac{1}{\sigma_{\omega^2}\omega}\frac{\partial \kappa}{\partial x_i}\frac{\partial \omega}{\partial x_i} \quad (3.4)$$

Once the solutions for κ and ω have been obtained, the turbulent viscosity μ_{turb} follows from

$$\mu_{turb} = \frac{\alpha \rho \kappa}{max(\alpha\omega, SF_2)} \quad (3.5)$$

The nomenclature particular to Eqs. (3.3) – (3.5) is

A	model constant
F_1, F_2	blending functions in the SST model
P_k	production term for the turbulent kinetic energy
S	absolute value of the shear strain rate
u_i	local velocity
x_i	tensor coordinate direction
α	SST model constant
β_1, β_2	SST model constants
ω	turbulent eddy frequency
κ	turbulence kinetic energy
μ	molecular viscosity
μ_{turb}	turbulent viscosity
σ	Prandtl-number-like diffusion coefficient
ρ	fluid density

The governing equations, Eqs. (3.1) – (3.5) were discretized by means of the finite volume method which is embedded in ANSYS CFX 14.5 software. After discretization and meshing, the number of nodes utilized for the solution was approximately eight million. As a validation of the sufficiency of the nodal count, a mesh independence study was performed. The metric used to quantify the mesh independence study was the mass flow rate. A comparison was made between the mass flow rates predicted by using meshes of

six and eight million nodes. The outcome of the comparison was a difference of 0.8%, which was judged as being of sufficient accuracy.

A special feature of the numerical simulation was the modeling of the rotating parts of the fan that was used as fluid mover. The actual fan in question is displayed in Fig. 3.10 (Sofasco D9225). As seen there, the fan is seven bladed and is contained in a square frame. The hub and the blades rotate while the other parts of the assembly are stationary. The geometric modeling of the fan started with a CAD drawing supplied by the manufacturer.

A creative portion of the modeling was to subdivide the solution domain into a rotating section and a stationary section. The rotational speed of the blades was set at 2000 rpm. Another issue relating to the problem setup was to create a solution domain of sufficient size so as not to constrain the natural air motion.

The pattern of fluid flow created by fans of the type utilized here is very complex. To illustrate the nature of the fluid flow, a fan discharging into free air has been numerically simulated, and the corresponding flow pattern is displayed in Fig. 3.11. The figure is an elevation view of the side of the fan. Air is drawn into the fan from the left and is discharged to the right. Since the fan is not shrouded, the pressure field that it creates also draws air over it as well as through it. At the right of the fan, a unique flow pattern can be observed. That flow is characterized by a direction towards the fan (a backflow) rather than away from it. This unexpected flow direction is created by a tornado-like swirl that is due to the rotating downstream face of the hub. The fluid adjacent to the face of the hub is also rotating. From a knowledge of the pressure field in a tornado, it is known that the center of rotation experiences a pressure that is so low as to draw fluid into it. This is the means by which the backflow is created.

It is not expected that the fan discharge in free air would be identical to the discharge in a confined space such as occurs in the present application. However, there is every reason to expect that the discharge will continue to be complex, albeit a different nature.

Fig. 3.10: Photograph of the fan used as the basis of the numerical simulations.

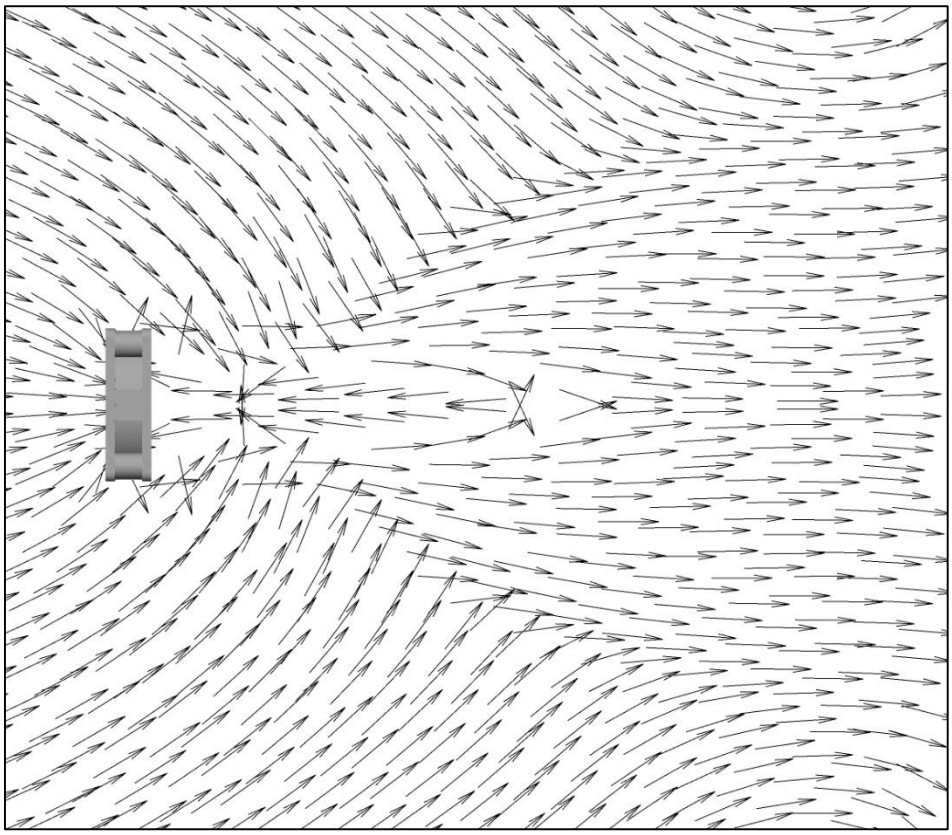

Fig. 3.11: Vector diagram displaying the pattern of fluid flow created by an axial fan discharging into free air.

3.3.2 Heat Transfer Analysis

The First Law of Thermodynamics for a constant-property, turbulent flowing fluid, supplemented by the Fourier law of heat conduction, is

$$\rho c_p \frac{\partial T}{\partial t} + \rho c_p \frac{\partial (u_i T)}{\partial x_i} = \frac{\partial}{\partial x_i}\left[(k + k_{turb}) \frac{\partial T}{\partial x_i}\right] \tag{3.6}$$

in which the quantity k_{turb} is used to quantify the contribution of turbulence to the transfer of heat. This quantity, in common with μ_{turb}, is not a true property of the fluid. To obtain numerical values for k_{turb}, the turbulent Prandtl number Pr_{turb} is used, where

$$Pr_{turb} = c_p \mu_{turb} / k_{turb} = 0.85 \tag{3.7}$$

The numerical value 0.85 is based on comparisons of predicted heat transfer coefficients with those of experiment [39,40].

The heat transfer problem is conjugate in that convection in the flowing fluid interacts with conduction in the pin fins. As a consequence, the heat conduction equation for the pin fins must be solved simultaneously with the fluid energy equation, Eq. (3.6). For unsteady fin conduction,

$$(\rho c)_{fin} \frac{\partial T_{fin}}{\partial t} = k_{fin} \frac{\partial^2 T_{fin}}{\partial {x_i}^2} \tag{3.8}$$

3.4 Heat Transfer Results and Discussion

The overall heat transfer result will be the first outcome to be discussed. That quantity was determined from the overall rate of heat transfer divided by the total surface area of the fins and the temperature difference between the base surface and the ambient air temperature. The final result is that h_{ave} = 4.07 W/m^2-^{o}C. This value is surprisingly low and requires some explanation. Careful examination of the pattern of fluid flow by means of vector diagrams, to be displayed shortly, revealed that some of the heated air exiting from the fin array was sucked into the fan inlet and was thereby returned to the fin array. This means, in reality, that the fins were washed by air of a higher temperature then that of the ambient. Now, with the reason for the poor performance understood by means of the velocity solution, the information needed to improve the performance is at hand. Clearly, the geometry of the airflow path has to be altered so that the heated air exiting the fin spaces is not able to be sucked into the fan inlet.

Attention will now be turned to the per-fin heat transfer results. The rate of heat transfer at each face of a given fin was determined and the results plotted in Figure 3.12. The vertical axis of the figure is the ratio of the rate of heat transfer at each face of each fin divided by the average value for each face of each fin. The fin numbers are distributed along the horizontal axis. The left-hand face of each fin is denoted as being the A-face and the right-hand face of each fin is the B-face. An overall inspection of the figure indicates that, aside from the neighborhood of the outboard fins, there is not a consistent pattern of difference between the A and B faces. With regard to the outboard fins, the out-facing surface of each such fin experiences higher rates of heat transfer than does the in-facing surface of that fin.

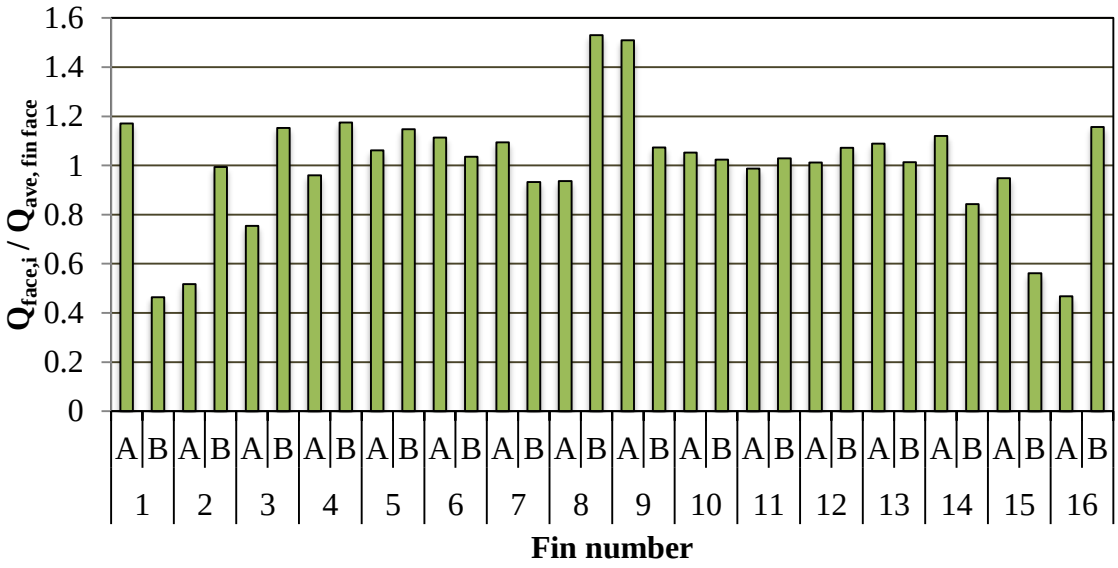

Fig. 3.12. Ratio of the heat transfer rate per fin face to the average fin rate of heat transfer.

Figure 3.13 provides a different viewpoint of the results of Figure 3.12. In the new figure, the heat transfer rates for the A and B sides of each fin are added and then plotted as a single per-fin value. It is seen from Figure 3.13 that 10 of the 16 fins are providing a heat transfer rate that is more or less equal to the average rate. The deviations from this pattern occur near the outboard ends of the fin array and also at the center of the array where the interfin spacing is larger than for the other fins. This non-uniformity in the spacing can readily be seen in Figure 3.9.

Further depth of exposition will reveal other insights into the nature of the heat transfer. To achieve the desired further depth, a color (graytone) contour diagram of the distribution of the heat flux on each of the two faces of each fin was extracted from the numerical solutions. Sample results from among the totality of the available color contour diagrams will now be presented, respectively in Figures 3.14, 3.15, and 3.16. See Appendix A for a complete set of heat flux contours for all of the fins surfaces. Figure 3.15 shows a pair of color contour diagrams (in gray tones) respectively for fin surfaces 3B and 4A. These surfaces bound the third flow passage, viewed from the left side outboard fin. Each of the two parts of Figure 3.14 has a grayscale connected with the heat flux value represented by each color. Both parts of the figure have the same color scale.

Note that the color scale expresses the heat flux values as a negative number which, in the convention used here, indicates the heat flow from the fin to the airflow.

The upper edge of each of each fin face corresponds to the location of the tips, whereas the lower edge of the face corresponds to the junction of the fin and the base. Inspection of the two parts of Figure 3.14 reveals a color pattern that is virtually the same. The highest heat fluxes occur in the neighborhood of the fin tips, and lowest fluxes occur in the neighborhood of the fin base. This observation suggests that the air entering the flow channel from the tip end does not have sufficient momentum to propel it to a strong impingement on the base.

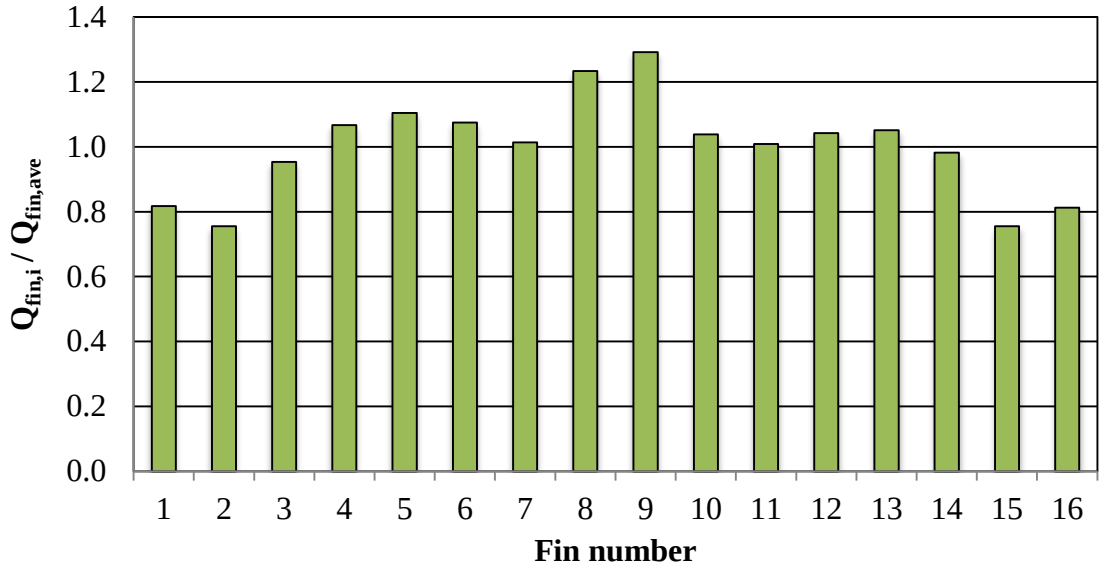

Fig. 3.13. Ratio of heat transfer rate per fin to the average per-fin heat transfer rate.

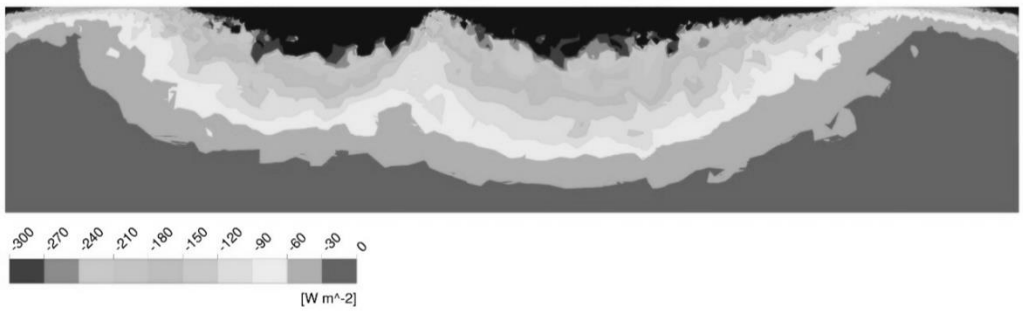

Fin 3, side B

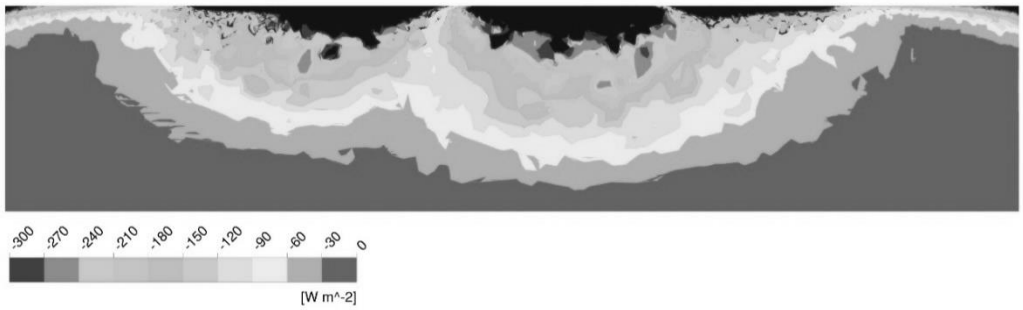

Fin 4, side A

Fig. 3.14. Color (graytone) contour diagrams showing the spatial variation of the heat flux on the surfaces of Fins 3B and 4A. These fins bound the third flow passage as viewed from the left outboard fin.

Information of the type conveyed by Figure 3.14 for the third flow passage is presented in Figure 3.15 for the flow passage seven. This flow passage is bounded by Fins 7B and 8A. Examination of Figure 3.15 shows that the two bounding fins exhibit heat flux distributions that are only slightly different from each other. Once again, in concert with Figure 3.14, the highest heat flux occurs in a narrow band in the neighborhood of the fin tips. There is a wider band of low heat flux in the neighborhood of the fin base.

The final figure in this sequence, Figure 3.16, exhibits information on the surfaces of Fins 13B and 14A. These surfaces bound the 13th flow passage. It is seen from this figure that, once again, the two fins that bound a flow passage experience very similar heat flux patterns. In fact, an overview of Figures 3.14, 3.15, and 3.16 indicates that there is consist flow pattern for all of these situations.

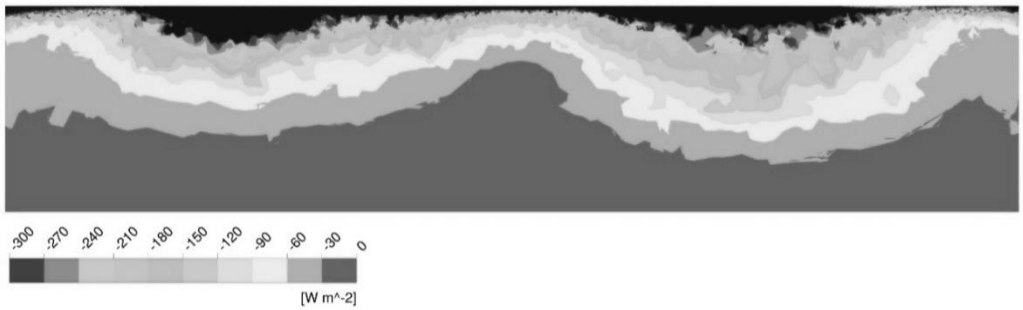

Fin 7, side B

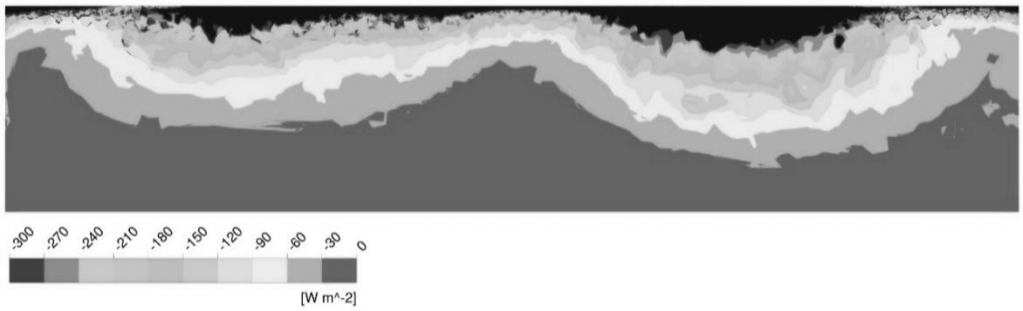

Fin 8, side A

Fig. 3.15. Color (graytone) contour diagrams showing the spatial variation of the heat flux on the surfaces of Fins 7B and 8A. These fins bound the seventh flow passage as viewed from the left outboard fin.

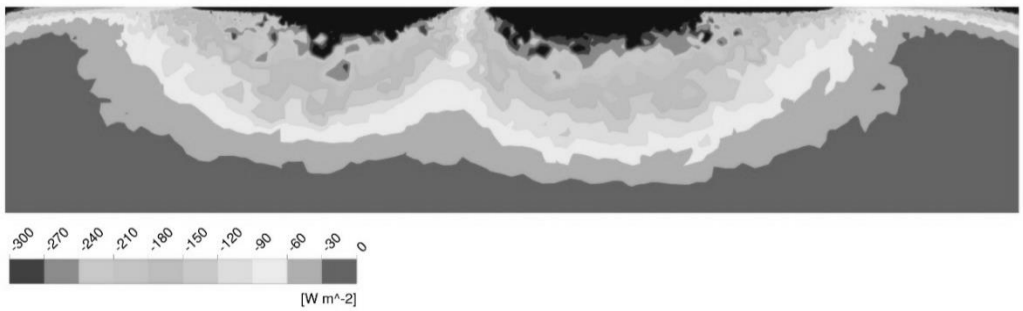

Fin 13, side B

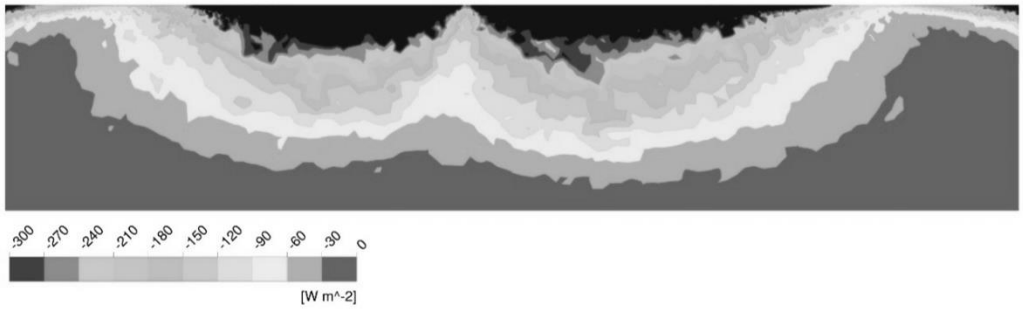

Fin 14, side A

Fig. 3.16. Color (graytone) contour diagrams showing the spatial variation of the heat flux on the surfaces of Fins 13B and 14A. These fins bound the 13th flow passage as viewed from the left outboard fin.

3.5 Fluid Flow Results and Discussion

3.5.1 Mass Flowrate

The fluid mover performs two functions: one is to impart motion to the fluid and other is to increase the pressure of the fluid. This pressure increase is to match the pressure drops that are necessarily experienced by the flowing fluid passing through the numerous resistances along its path. Those resistances are caused by friction, momentum change, and recirculation. Atmospheric air is drawn into the system, and once traversing the system, the air exits into the surroundings at atmospheric pressure. It is this balance that requires that the pressure rise due to the fan must match the internal pressure drops.

The rate of fluid flow is not known *a priori*, but rather is one of the major results of the numerical simulation. Its value depends on the rotational speed of the fan, the number of blades, and the shape of the blades. Once a fan is selected, its geometry is fixed, and the produced mass flow rate is only a function of the rotational speed. In this light, for the fixed rotational speed of 2000 rpm that was used for the numerical simulations, there is a unique value of the mass flow rate. That value is 5.19×10^{-7} kg/s.

Although the most efficient heat exchange configuration would have the same heat transferred by each one of the fins, this ideal operation is rarely encountered in practice. To obtain perspective on the degree of inefficiency of the present fin assemblage and for guidance for a possible improved design, the mass flow rate passing thorough each of the interfin spaces will be displayed and discussed. As a first step to clarify the notation, Fig. 3.17 has been prepared. It is seen that each interfin space presents four possible exits to the fluid supplied to it by the rotating fan. These exits are carefully labeled in the figure. To clarify the geometric notation with regard to the exits, a schematic diagram has been prepared and is presented in Fig. 3.17.

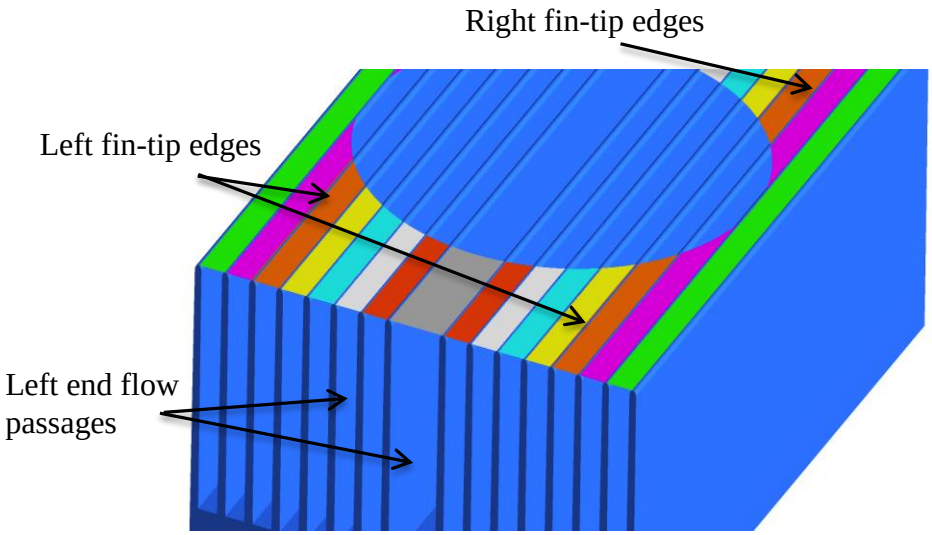

Fig. 3.17: Definition of nomenclature for fluid outflows from the fin array.

The actual numerical mass flowrate results are presented in Fig. 3.18. The figure is a bar graph in which the mass flow rates for each of the 15 interfin spaces is displayed by a unique bar. As seen in the figure, each bar is constructed of four segments, each of which corresponds to a given exit direction as defined in Fig. 3.18.

Inspections of Fig. 3.18 reveals an ordered pattern which is dependent on the direction of rotation of the fan. First of all, it can be seen that the outflows that cross the plane of the fin tips is of little consequence. The major outflows occur at the outboard ends of the fin-formed flow passages. For those passages which lie to the right of the central one, it appears that the main outflow direction is at the forward end of these passages. An opposite direction of outflow holds sway for the passages that are left of center.

Also of significance is the fact of the non-uniformity of the mass flow rate that passes through the individual channels. The practical ramifications of this observation are twofold; (a) the pressure drop due to the mass flow non-uniformity is greater than that which would correspond to a uniform mass flow rate and (b) the rate of heat transfer would be characterized by a non-uniformity which reflects the non-uniformity of the rates of fluid flow. This outcome suggests the need for redesign of the coolant portion of the overall DNA characterization device.

A final observation of Fig. 3.18 relates to the mass flow at the central passage. It can be seen that the outflow is confined to the plane of the fin tips.

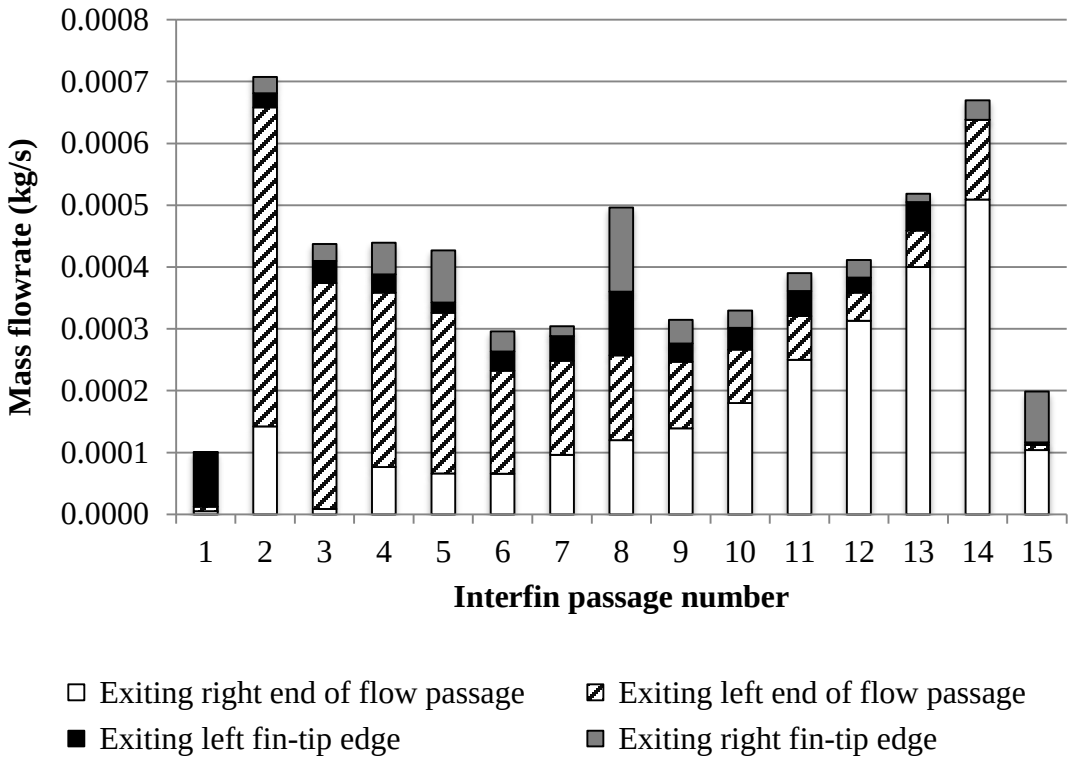

Fig. 3.18: Mass flow rate exiting each of the flow channels of the fin array. See Fig. 3.17 for a definition of terms.

3.5.2 Pressure Drop

To obtain the pressure rise provided by the fan, it is appropriate to make reference to its characteristic operating curve which is displayed in Fig. 3.19.

From the mass flow rate that was stated in the previous paragraph in units of kg/s, the volumetric flow rate can be deduced to be 2.6×10^{-5} m^3/min. From Fig. 3.19 and curve L, the corresponding pressure rise provided by the fan is 2.2 mm of H_2O. This pressure rise is the maximum that this fan can provide.

3.5.3 Fluid Mechanic Insights

To illuminate the pattern of fluid flow, it is fruitful to create vector diagrams. In that regard, there are two forms of vector diagrams: (a) normalized and (b) un-normalized. In the normalized format, all vectors are given a common length. This format gives rise to an unambiguous presentation of the directions of the fluid flow. In contrast, the un-normalized format displays the local magnitudes of the flow. Figure 3.20 exhibits the pattern of fluid flow in a typical channel in the array in the normalized format. The figure is annotated using designations that were previously employed in Fig. 3.17. Inspection of Fig. 3.20 clearly shows the directions of fluid flow. Of particular interest are the recirculation zones which are creators of pressure drop without compensating by motion in the streamwise direction. A more competent design would be guided by the motivation to eliminate these zones of recirculation.

Figure 3.21 is the non-normalized counterpart of Fig. 3.20. In the non-normalized display, zones of virtually stagnant flow are revealed. In particular, above the aluminum sample block, such a quiescent zone can now be seen. Also revealed in the figure is the virtual absence of fluid leaving the interfin flow passage through the plane of the tips. Finally displayed is the different flow magnitudes on the frontend side and backend side.

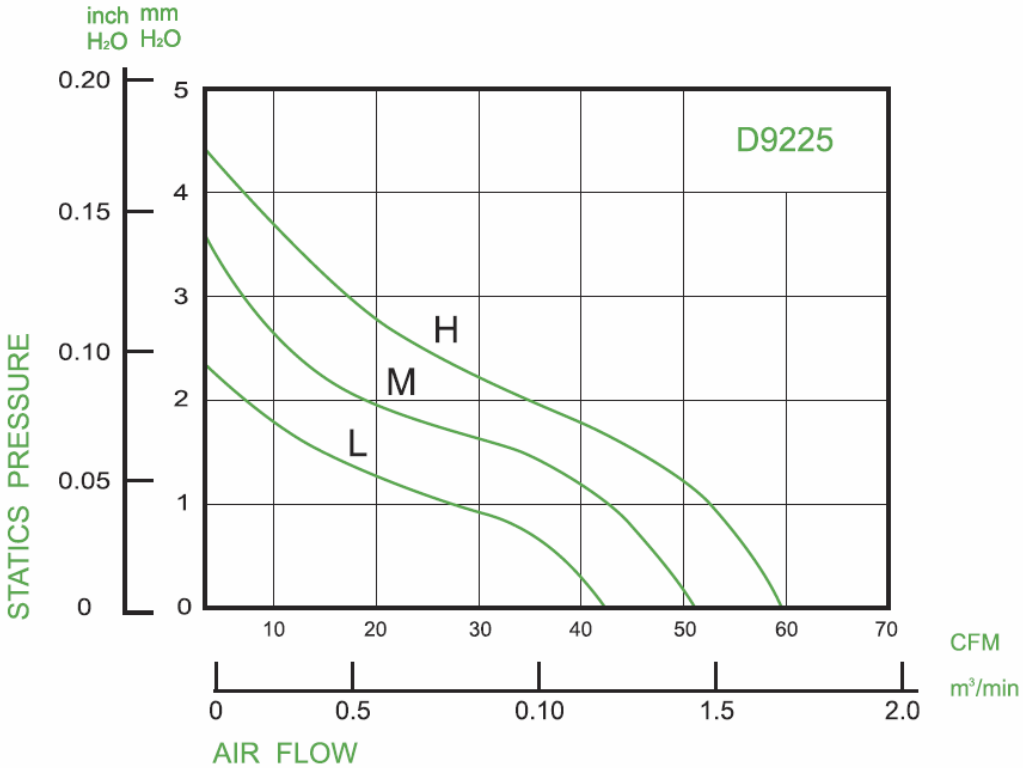

Fig. 3.19: Characteristic operating curve for the fan used in the numerical simulations.

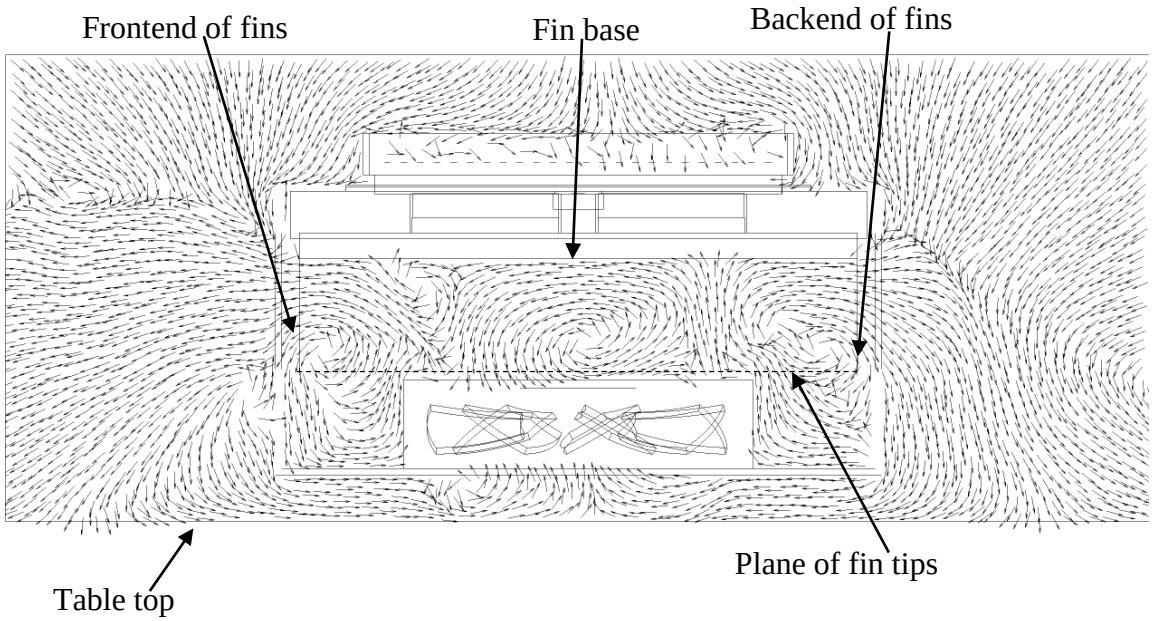

Fig. 3.20: Normalized vector diagram corresponding flow channel nine.

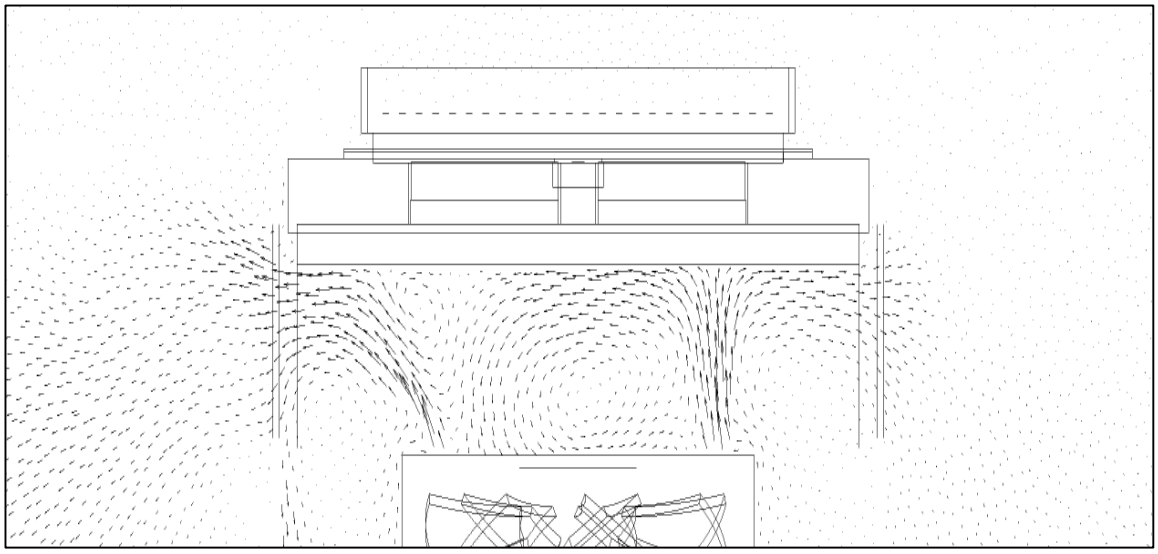

Fig. 3.21: Non-normalized vector diagram corresponding flow channel nine.

3.5.4 Turbulence Magnitudes

It is a maxim that turbulence plays an important affirmative role as an enhancement of the rate of heat transfer. The downside of intense turbulence is a significant increase in pressure drop. The author has introduced a new metric to characterize the strength of the turbulence in the flow passages formed between adjacent fins. The metric is the ratio μ_{turb}/μ. When this ratio is much less than one, the turbulence is either non-existent or irrelevant. On the other hand, typical turbulent flows in passages such as pipes experience ratios well over a hundred.

Values of μ_{turb}/μ have been extracted from the numerical solutions. As a prelude to the display of these results, a geometrical specification of the locations of where this ratio is to be displayed is presented in Fig. 3.22.

As can be seen from Fig. 3.22, the selected locations are: (a) at the center plane directly aligned with the hub of the fan, (b) 50% of the distance between the center and the outboard end of the fin in both directions, (c) 95% of the distance between the center and the outboard end of the fin in both directions.

Figure 3.23 shows a color contour diagram corresponding to the foregoing location (a). All 15 flow passages are displayed. Below the diagram is a color strip that is keyed to the numerical values of the ratio μ_{turb}/μ. Of particular note are the values ranging from 0.5 to 13 that are spanned by the ratio. The value 0.5 demonstrates that strictly laminar flow is not achieved anywhere at the chosen location. On the other hand, it reflects a very modest turbulence. Even the maximum value of the ratio, 13, does not correspond to a highly vigorous turbulence.

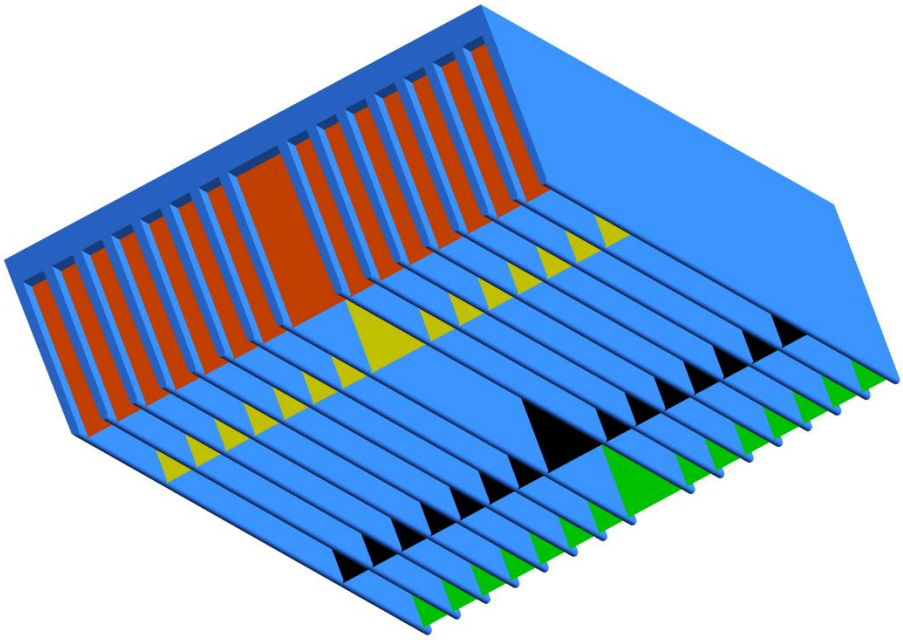

Fig. 3.22: Geometric specification of the locations where the ratio μ_{turb}/μ is to be presented.

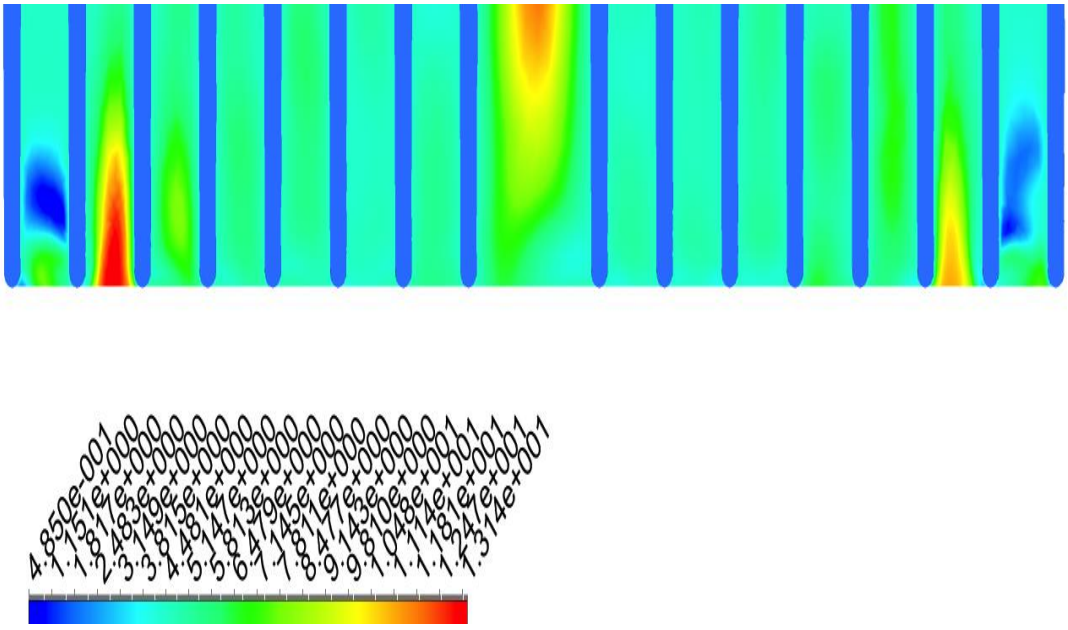

Fig. 3.23: Color contour diagram showing the ratio μ_{turb}/μ at the center plane of the fin array directly aligned with the hub of the fan.

The next figure, Fig. 3.24, corresponds to a location that is 50% of the distance between the center and the frontend of the fin. Examination of the color strip indicates an incremental increase in the turbulence level but of no practical significance.

The counterpart of Fig. 3.24, but in the direction of the backend, is presented in Fig. 3.25. Although the upper and lower values displayed in Fig. 3.25 are hardly different from those of Fig. 3.24, the distribution of the values of the ratios differ between the figures. In particular, there are more high turbulence zones in evidence in Fig. 3.25. This difference in pattern can be attributed to the higher velocities that prevail in the latter case.

The next two figures correspond to locations that are 95% of the distance between the center and the respective frontend and backend of the fin array. Figure 3.26 conveys results for the μ_{turb}/μ ratio for the frontend location. From an inspection of the figure, it can be seen that the center channel is the only one among the channels where high turbulence prevails. The counterpart of Fig. 3.26 is Fig. 3.27 which corresponds to the backend location. The two figures are virtually identical in the information that they convey.

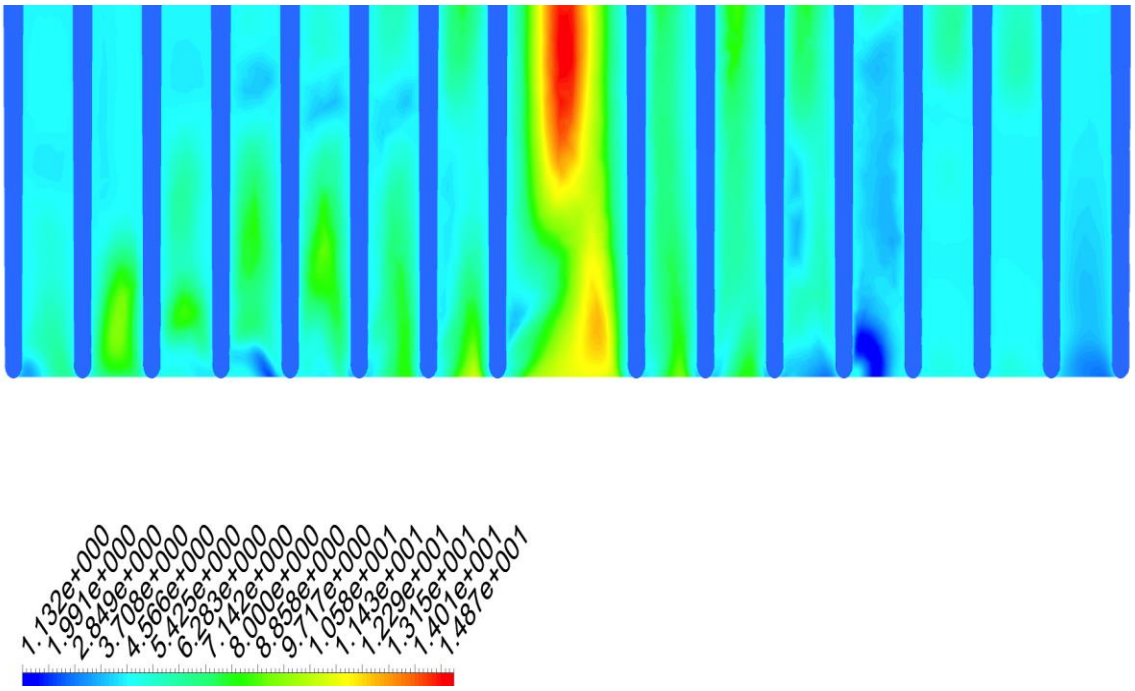

Fig. 3.24: Color contour diagram showing the ratio μ_{turb}/μ at a location that is 50% of the distance between the center and the frontend of the fin.

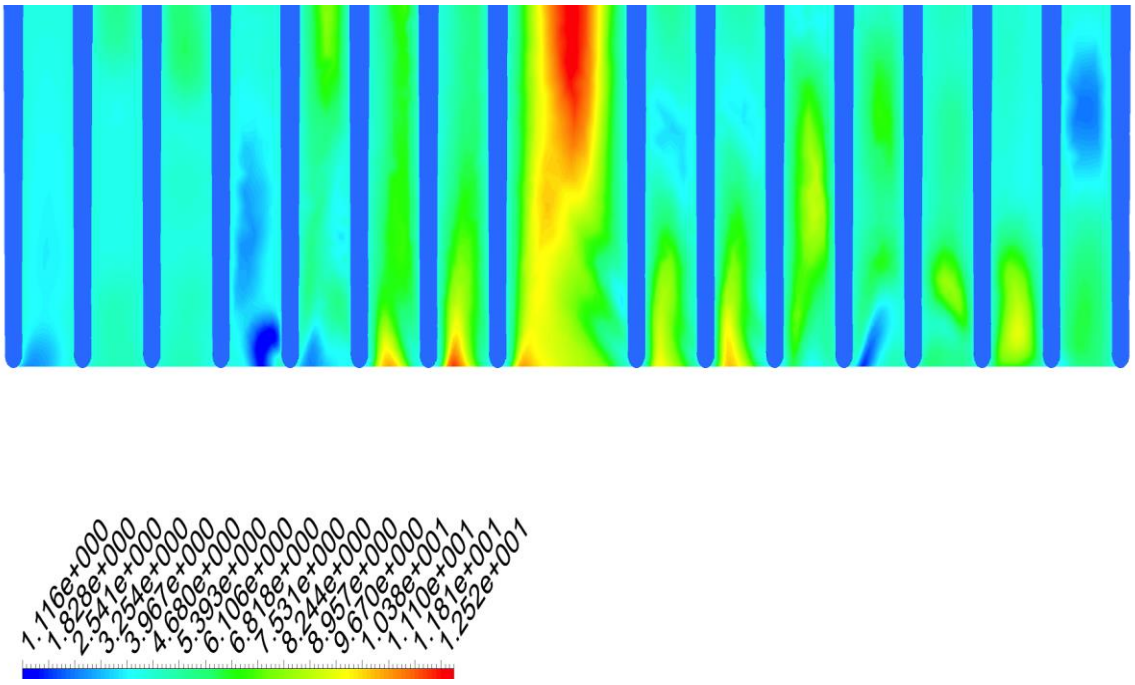

Fig. 3.25: Color contour diagram showing the ratio μ_{turb}/μ at a location that is 50% of the distance between the center and the backend of the fin.

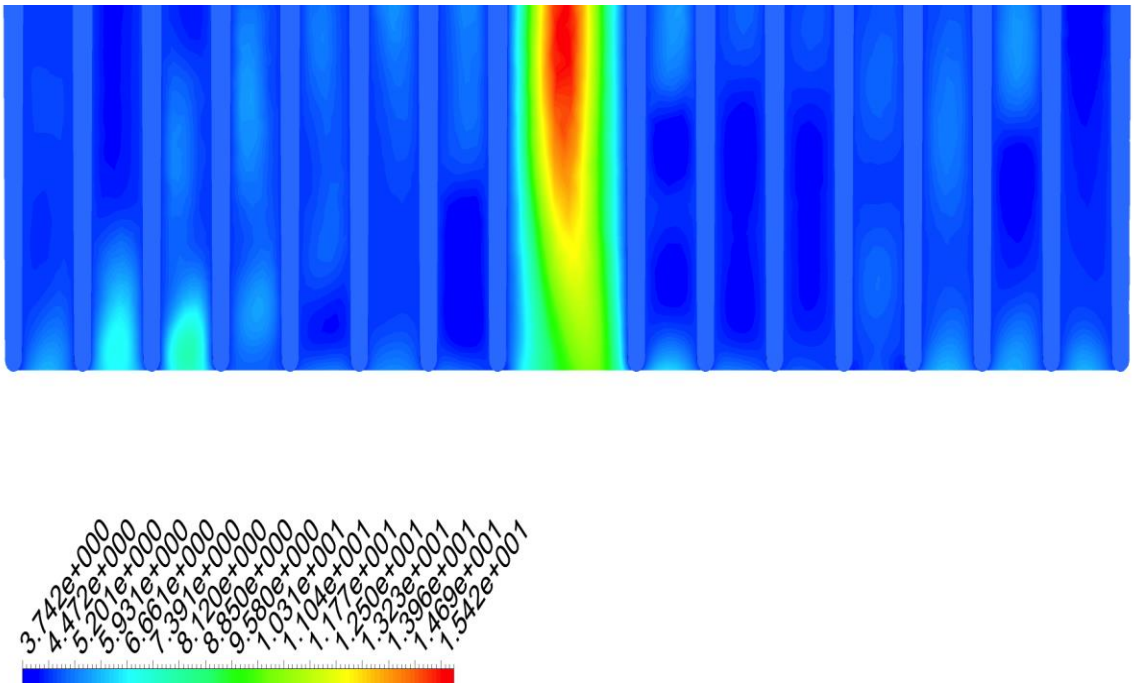

Fig. 3.26: Color contour diagram showing the ratio μ_{turb}/μ at a location that is 95% of the distance between the center and the frontend of the fin.

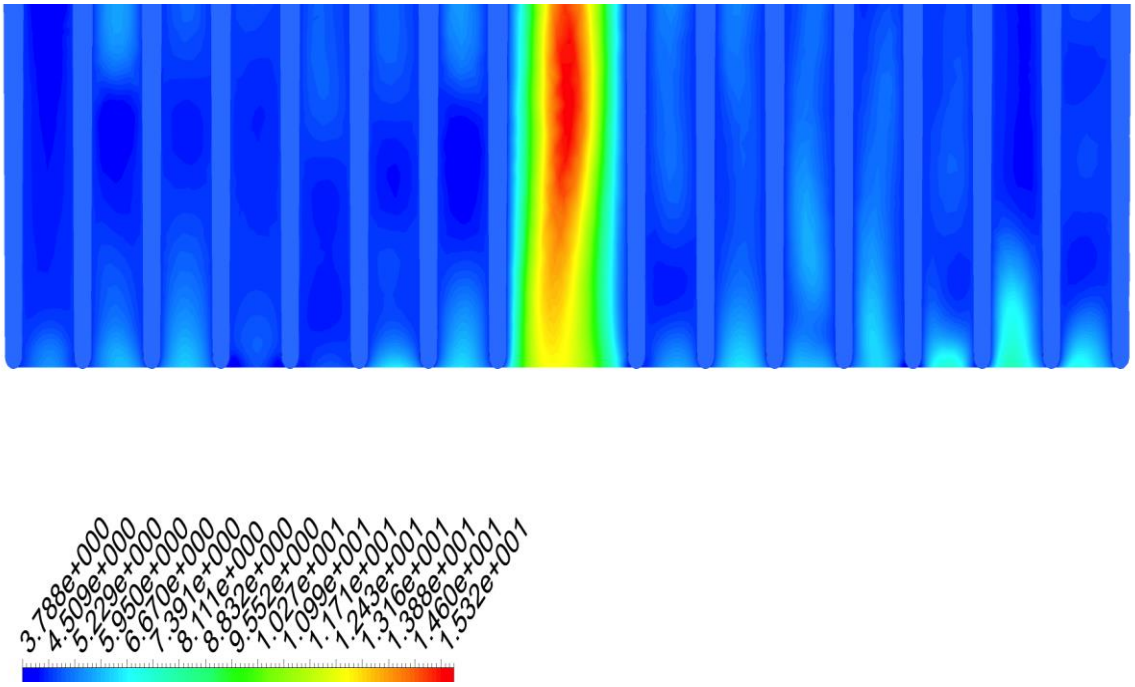

Fig. 3.27: Color contour diagram showing the ratio μ_{turb}/μ at a location that is 95% of the distance between the center and the backend of the fin.

3.6 Retrospective Summary of Chapter 3

From the heat transfer literature, very little heed has been paid to the effect of turbulence level on convective heat transfer coefficients. Therefore, only intuitive-based comments are possible. It is the belief of the author that the relatively low values of the μ_{turb}/μ ratio impose a penalty on the heat transfer rates that are possible in this device. This outcome suggests the need to a redesign which accentuates the turbulence level.

There are a number of turbulence promoters that may be envisioned to increase the turbulence level. One category is to interrupt the boundary layer adjacent to the bounding walls of the flow passages. The greatest resistance to convective heat transfer is lodged in a very narrow wall-adjacent region. If the interruption means is confined to that narrow region, heat transfer enhancement can be achieved with a minimal increase in pressure drop.

Chapter 4

EFFECT OF FAN-GENERATED SWIRL ON TURBULENT HEAT TRANSFER AND FLUID FLOW IN A PIPE

4.1 Introduction

In a commonly encountered situation, fluid is ducted to a heat exchanger from a fan, blower, or pump that may be somewhat distant from the inlet of the exchanger. In that case, the attributes of the flow entering the exchanger are affected both by the swirling nature of the fan-produced flow and its subsequent interactions with the delivery duct. In another practical situation, the fan may be situated at the inlet of a pipe where heat transfer is taking place and blows its swirling discharge directly into the pipe. Both of these situations serve to motivate the research that is reported in this chapter.

The specific situation to be dealt with here is an axial fan with *rotating blades* situated at the upstream end of a round pipe and blowing into the pipe without the presence of an intervening flow-modifying medium. The temperature of the inflowing fluid is different from the temperature of the pipe wall, thereby creating heat transfer.

There is a rich literature on the use of inserted swirl-producing objects to enhance heat transfer in pipes. Among the utilized methods are twisted-tape inserts [25-29] and stationary or fluid-driven rotating blades [30-34]. On the other hand, a literature search failed to produce any published articles which dealt with a fan with rotating blades discharging flow into a round pipe where heat transfer was occurring. The swirl produced by the aforementioned inserted objects differs from that created by moving, rotating fan blades.

The method used in the analysis and solution of the just-defined problem is numerical simulation. To facilitate the work, an actual axial fan was modeled without approximation and with strict account being taken of the rotation of the blades. Special focus was directed

to the friction-related decay of the swirl that is produced by axial fans. There is evidence [35] that a swirling flow entering a pipe can be long lasting.

The investigation encompasses both fluid flow and heat transfer characteristics. For fluid flow, the circumferential variations of shear and pressure were identified as functions of the downstream distance from the rotating blades. In particular, the degree of frictional resistance attributable to rotation was determined. With regard to heat transfer, the circumferential variations of the heat flux and the circumferential average of the wall heat flux were obtained, both as a function of axial position. The extent of heat transfer enhancement due to rotation was carefully documented. For comparison purposes, two cases characterized by non-swirling, uniformly distributed fluid inflows were investigated. One of these was based on the use of the blower curve for the particular fluid mover in question. The other case made use of the mass flow rate delivered by the actual rotating fan but envisioned that the flow entering the pipe has a uniform velocity profile. Comparisons among these cases enabled the effect of swirl to be viewed from different perspectives.

4.2 The Physical Situation

A schematic diagram of the physical situation to be considered here is presented in Fig. 4.1. As seen there, an axial fan is situated at the inlet of a round pipe. The fan draws air from the upstream space and discharges it directly into the pipe inlet. The air experiences frictional interaction with the pipe wall with the outcome that the fan-imparted swirl decays. The temperature of the flow entering the pipe is different from that of the pipe wall, so that heat transfer occurs. It is expected that the heat flux would vary both circumferentially and longitudinally.

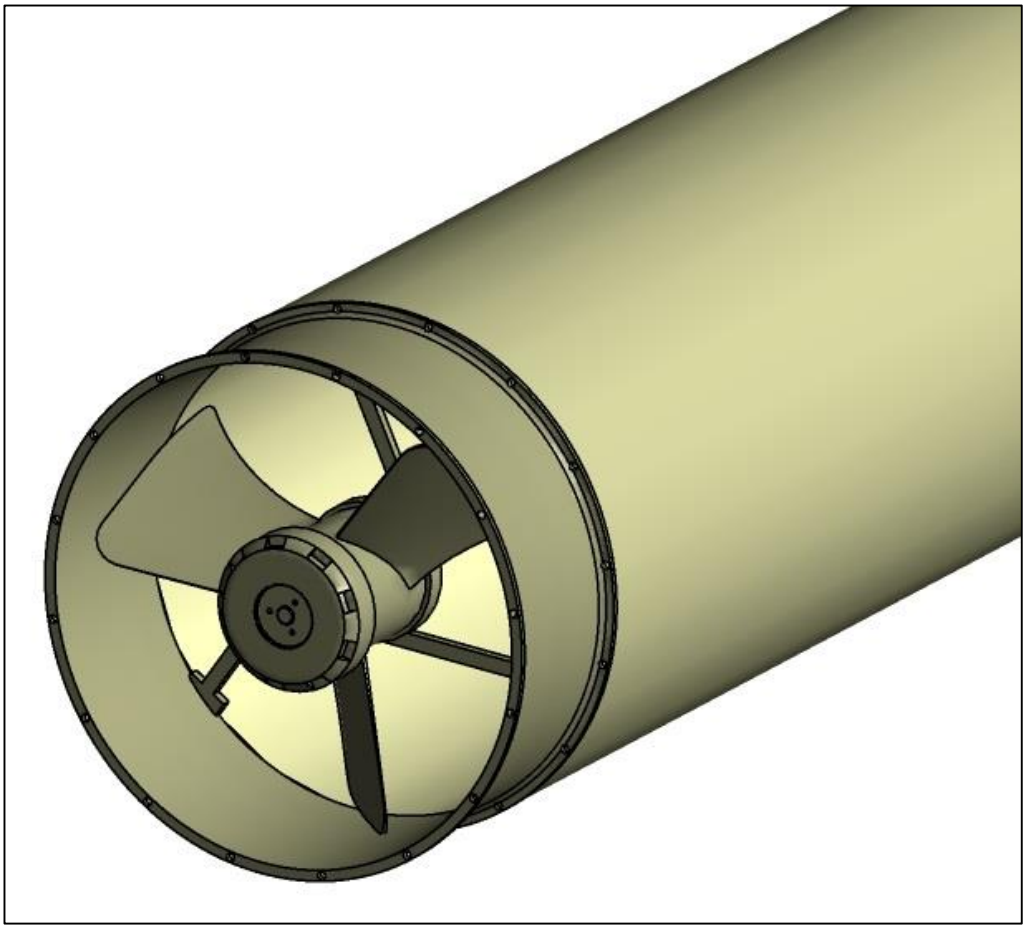

Fig. 4.1: Schematic diagram of the problem under consideration showing a rotating fan discharging swirling flow into a round pipe.

The flow is intrinsically turbulent, so that a turbulence model is a necessary part of the solution methodology. It is expected that the turbulence level would be greatest in the fan discharge and would decrease in the downstream direction. It is also reasonable to expect that the flow pattern and the heat transfer would depend on the length of the pipe into which the fan discharges.

Three different situations are to be investigated. The primary problem is the one in which the fan discharges into the pipe. For comparison purposes, two relatively simpler situations will also be considered. One of these is based on applying the blower curve for the fan in question to provide a flow rate which is uniformly distributed across the pipe inlet. That flow does not contain swirl. A second comparison case is based on utilizing the flow rate delivered to the pipe inlet by the actual rotating fan. However, for this comparison case, it is assumed that that flow rate is uniformly distributed across the pipe inlet and that there is no swirl.

The solution methodology is based on modeling and subsequent numerical simulation. The flow provided to the pipe inlet by the rotating fan is auto-determined. For the other two cases, the flow rates are as described in the preceding paragraph. Since the flow rates cannot be arbitrarily specified, the Reynolds number cannot be arbitrarily varied as an independent parameter. The pipe length was varied parametrically and was the one prescribable independent variable.

4.3 Mathematical Modeling

In the considered physical situation, the fluid flow is three-dimensional, turbulent, and unsteady. The adopted simulation software is ANSYS CFX 15.0. This software is based on discretization by means of the finite-volume method. To ensure high accuracy, the discretized solution domain was meshed with approximately 40 million nodes.

There are a number of turbulence models that are believe capable of accurate modeling of the present situation. The Shear Stress Transport (SST) model has been utilized [13] with considerable success in the past, and experimental verification may be found in [36-38]. A unique feature of the SST model is its hybrid nature. It brings together the venerable κ-ε model and the relatively newer κ-ω model. The former has been demonstrated to give rise to accurate results away from bounding surfaces whereas the latter has been shown to be highly effective in the near neighborhood of the bounding walls. The quantity κ is the turbulence kinetic energy, ω is the specific rate of turbulence dissipation, and ε is rate of dissipation.

Another issue that is critical to the fidelity of the simulation model is the choice of the volume in which the solutions are carried out. The guiding principle for choosing the solution space is that the fluid have full freedom to execute its natural motions. In the present model, the fan draws air from its upstream and lateral surroundings and the selected solution domain must take this into account.

The relevant physical principles that govern the flow and heat transfer are: momentum conservation (Reynolds-Average Navier-Stokes equations), mass conservation, and the First Law of Thermodynamics. These equations are written for incompressible, constant property flow.

The RANS equations written in the compact Cartesian-tensor form are

$$\rho \frac{\partial u_j}{\partial t} + \rho \left(u_i \frac{\partial u_j}{\partial x_i} \right) = -\frac{\partial p}{\partial x_j} + \frac{\partial}{\partial x_i} \left((\mu + \mu_{turb}) \frac{\partial u_j}{\partial x_i} \right) \quad i = 1,2,3 \;\; j = 1,2,3 \tag{4.1}$$

and the mass conservation equation is

$$\frac{\partial u_i}{\partial x_i} = 0 \tag{4.2}$$

The u_i are the velocity components, x_i the coordinates, p the pressure, and ρ and μ the density and viscosity of air, respectively. The quantity μ_{turb} is designated as the turbulent viscosity.

The equations of the SST model are

$$\frac{\partial(\rho\kappa)}{\partial t} + \frac{\partial(\rho u_i \kappa)}{\partial x_i} = P_\kappa - \beta_1 \rho\kappa\omega + \frac{\partial}{\partial x_i}\left[\left(\mu + \frac{\mu_{turb}}{\sigma_\kappa}\right)\frac{\partial \kappa}{\partial x_i}\right] \tag{4.3}$$

$$\frac{\partial(\rho\omega)}{\partial t} + \frac{\partial(\rho u_i \omega)}{\partial x_i} = A\rho S^2 - \beta_2 \rho\omega^2 + \frac{\partial}{\partial x_i}\left[\left(\mu + \frac{\mu_{turb}}{\sigma_\omega}\right)\frac{\partial \omega}{\partial x_i}\right] + 2\rho(1 - F_1)\frac{1}{\sigma_{\omega 2}\omega}\frac{\partial \kappa}{\partial x_i}\frac{\partial \omega}{\partial x_i} \tag{4.4}$$

The solution of Eqs. (4.3) and (4.4) yields the values of κ and ω, which give the turbulent viscosity μ_{turb} from

$$\mu_{turb} = \frac{\alpha\rho\kappa}{\max(\alpha\omega, SF_{2)}} \tag{4.5}$$

The symbols that appear in Eqs. (4.3) – (4.5) were defined previously in the Nomenclature found in Chapter 3, Section 3.3.

The heat transfer problem is governed by the First Law of Thermodynamics in conjunction with the Fourier heat conduction law. For incompressible, constant property flow, the First Law can be written as

$$\rho c_p \frac{\partial T}{\partial t} + \rho c_p \frac{\partial(u_i T)}{\partial x_i} = \frac{\partial}{\partial x_i}\left[(k + k_{turb})\frac{\partial T}{\partial x_i}\right] \tag{4.6}$$

in which T is the fluid temperature, and c_p and k are, respectively, the specific heat and thermal conductivity of the fluid. The quantity k_{turb} is designated as the turbulent thermal conductivity. Its value is closely linked to that of the turbulent viscosity by means of the turbulent Prandtl number

$$Pr_{turb} = \frac{c_p \mu_{turb}}{k_{turb}} \tag{4.7}$$

Extensive experience has shown that a constant value of $Pr_{turb} = 0.85$ gives rise to highly accurate heat transfer results [39, 40].

The specific fan chosen for the investigation was based on its capability to deliver the flow rate and pressure rise suitable for the application. The chosen fan is Sofasco model D25089K 24V, which has an external frame diameter of 254 mm. The fan blade region (the portion of the solution domain inside of the fan housing and the corresponding mesh) was rotated at 1650 RPM as specified by the manufacturer.

The patterns of fluid flow provided by the fan are presented in Figs. 4.2(a) and (b). This information is conveyed by vector diagrams. In Fig. 4.2(a), the vectors are normalized to have a common length so that they are limited to showing the direction of flow. On the other hand, the vectors of Fig. 4.2(b) are unnormalized so that their lengths are proportional to the magnitude of the flow. The images displayed in Fig. 4.2 are plan views. As can be seen from Fig. 4.2(a), air is drawn unsymmetrically into the fan from the upstream space, with the asymmetry due to the bias imposed by the direction of fan rotation. The outflow of the fan is by no means straight and parallel. Figure 4.2(b) shows that the strongest fan-produced flow clings to the walls of the pipe.

(a)

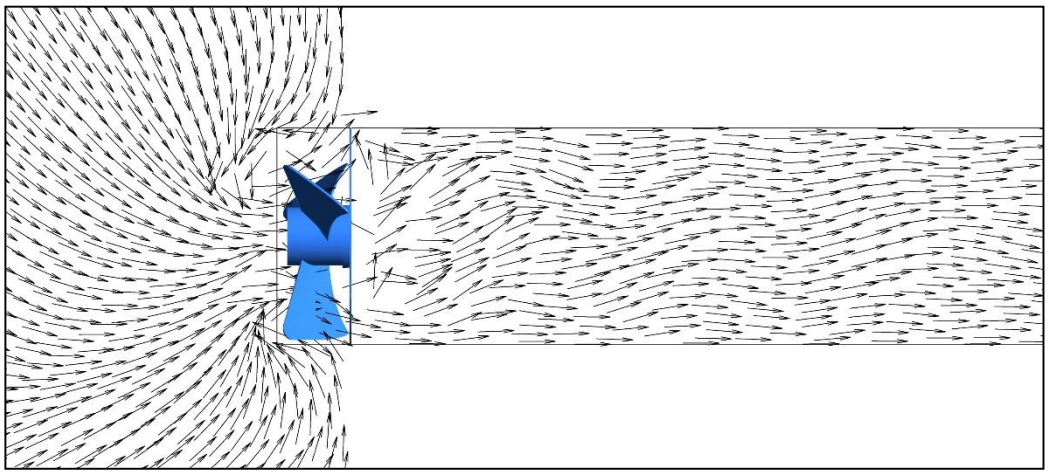

(b)

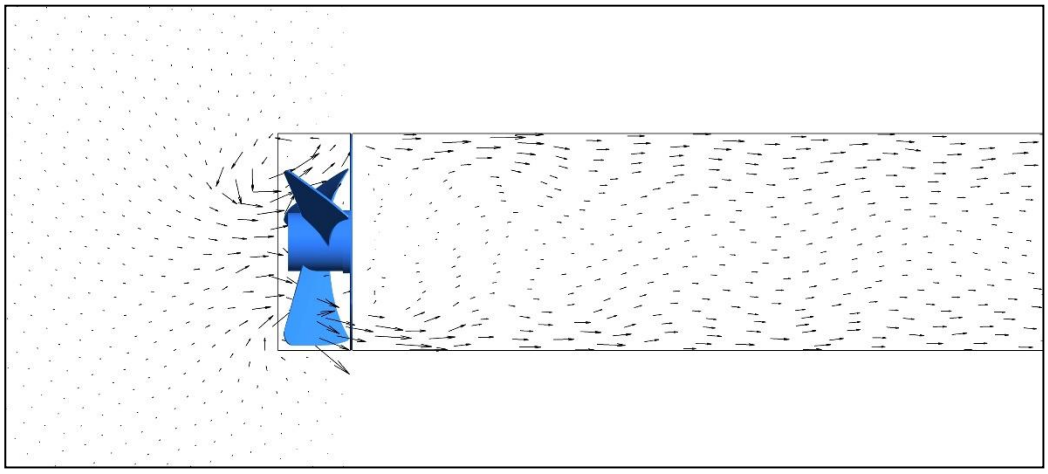

Fig. 4.2: Vector diagrams illustrating the characteristics of the flow provided by the rotating fan. (a) Vectors normalized to show the flow directions; (b) vectors unnormalized to show the magnitudes of the flow.

An alternative but relevant flow situation is based on the use of the blower curve for the fan in question. Figure 4.3 displays the blower curve, which starts at the upper left of the figure and proceeds downward toward the right. It is a graph in which the pressure rise accomplished by the blower is plotted as a function of the delivered volumetric flow rate. In addition to the blower curve proper, there are two system curves displayed, respectively corresponding to pipes of length L/D = 40 and 60.

A system curve displays the pressure drop experienced by a specified volumetric flow passing through a system. The two systems considered are pipes of L/D = 40 and 60. The intersection of the system curve and the blower curve defines the operating point. As can be seen from Fig. 4.3, the operating point for the 40 L/D pipe corresponds to a higher flow rate and lower pressure relative to the operating point for the 60 L/D pipe. The nature of the delivered inlet flow corresponding to the blower curve is uniformly distributed.

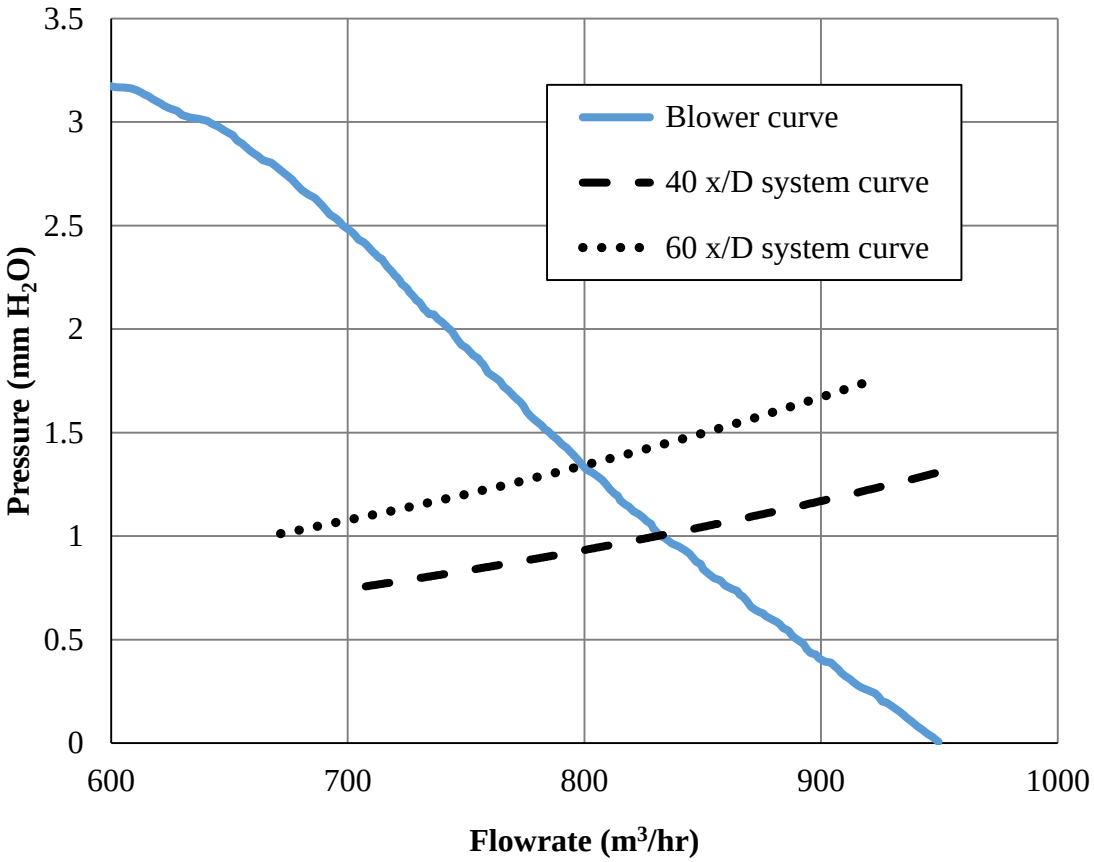

Fig. 4.3: Blower curve for Sofasco D25089K 24V and system curves for ducts of length L/D = 40 and 60 over the range of interest.

4.4 Heat Transfer Results and Discussion

The heat transfer results are of direct applicability. Although there is a circumferential variation of the local heat transfer coefficient, that information is difficult to apply in practice. Rather, attention will first be given here to the circumferential average heat transfer coefficient *h* defined as

$$h = \frac{1}{2\pi}\frac{\int_0^{2\pi} q(x,\theta)d\theta}{T_{wall}-T_{bulk,x}} \tag{4.8}$$

where $q(x,\theta)$ is the wall heat flux at an axial position *x* at an angle θ on the circumference, T_{wall} is the prescribed uniform wall temperature, and $T_{bulk,x}$ is the bulk temperature at *x*. The dimensionless value of *h* is conveyed by the Nusselt number $Nu_D = hD/k$.

Figure 4.4 displays the variation of the Nusselt number as a function of the dimensionless axial distance *x/D* for the pipe length of *L/D* = 40, while similar information for the *L/D* = 60 pipe is exhibited in Fig. 4.5. In each figure, there is a main graph and an inset, the latter presenting an expanded view for larger values of *x/D*.

Inspection of Figs. 4.4 and 4.5 provides an interesting set of impressions. First of all, fan rotation is seen to enhance the heat transfer coefficient. Compared to the results corresponding to the blower-curve model, the Nu_D values for the fan-rotation case are, respectively, 1.95, 1.76, 1.57, and 1.51 for *x/D* = 5, 10, 15, and 20. These ratios were determined specifically for the *L*/D = 40 case, but those for the case of *L*/D = 60 are virtually the same. In both figures, the axial variation of Nu_D for the rotating blower is monotonically decreasing. On the other hand, the other two cases, blower curve and matched flow rates, the Nusselt numbers experience an undershoot in the neighborhood of *x/D* = 15 and increase thereafter. This finding has been previously reported [41, 42]. Note that the latter two cases are characterized by uniform inlet velocities at the entrance of the pipe.

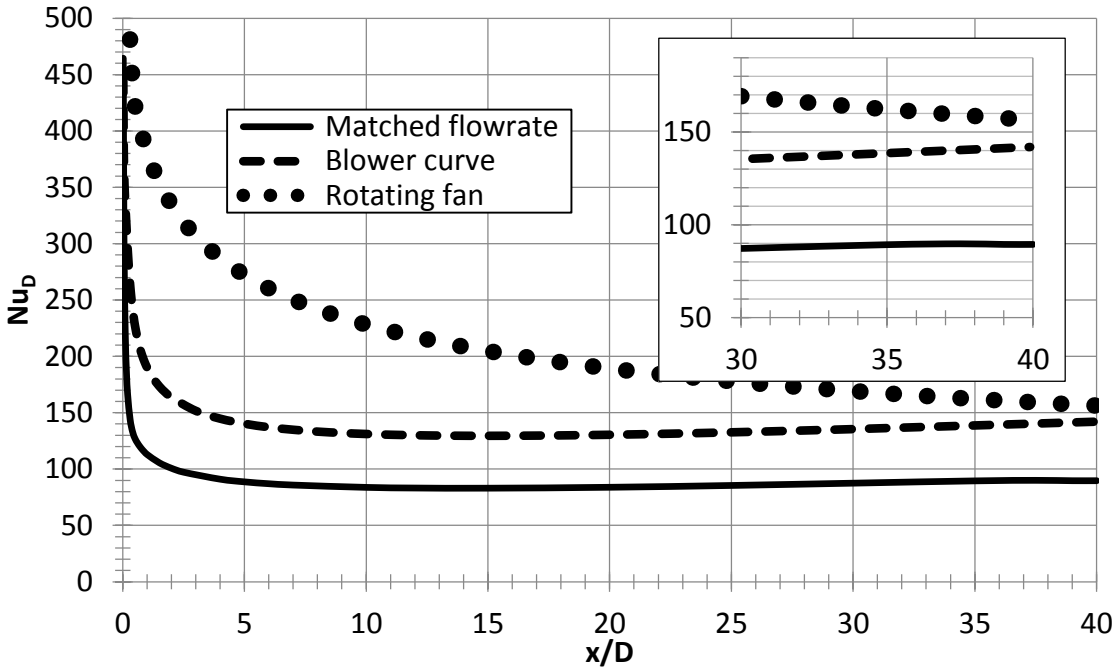

Fig. 4.4: Variation of the circumferential-averaged Nusselt number as a function of the axial coordinate *x/D* for a pipe length *L/D* = 40.

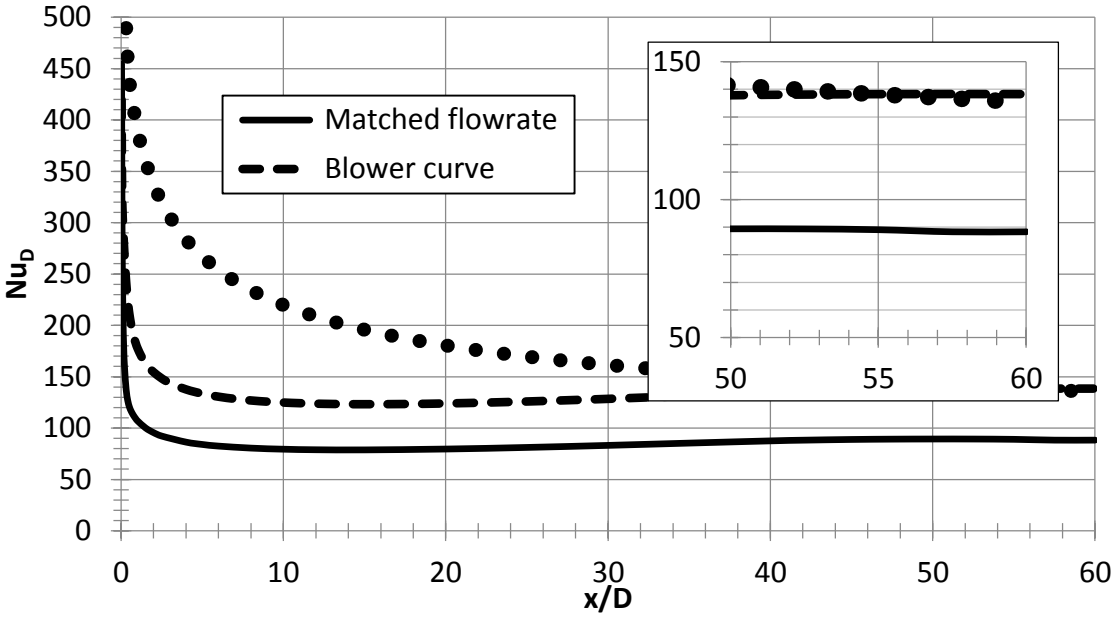

Fig. 4.5: Variation of the circumferential-averaged Nusselt number as a function of the axial coordinate *x/D* for a pipe length *L/D* = 60.

Further observation of these figures indicates that the fan-driven flow experiences a much longer thermal development length than do the other cases, both of which are initiated with a uniform inflow velocity without swirl. This extended development length may be attributed to the longevity of the swirl. This longevity has been noted in the past [11]. For the L/D = 40 pipe, none of the considered cases reaches the thermally developed regime. On the other hand, for the L/D = 60 pipe, only the blower-curved-based flow attains thermal development.

The next heat transfer result is a display of a typical pattern of circumferential variations of the local wall heat flux. This information is conveyed in Fig. 4.6 for the case of the L/D = 40 pipe for x/D locations of 5, 10, 20, and 30. At every such location, significant circumferential variations are in evidence. Broadly speaking, the ratio of the maximum to the minimum heat flux at a given axial location is a factor of two.

The final thermal-related result to be presented here are color-contour diagrams of the fluid temperature for the L/D = 60 pipe at selected cross sections x/D = 10, 30, and 55. These results are presented in Fig. 4.7. In interpreting this figure, it is relevant to point out that the inlet air temperature was specified to be 25^{o}C, and the wall temperature was assigned the uniform value of 60^{o}C. Furthermore, the color legends beneath each figure are different in that the left-hand end of the respective legends corresponds to the lowest temperature in each cross section. It is seen from the figure that the temperatures spanned in each cross section decreases with increasing downstream distance, reflecting the increase of fluid temperature. This reduced temperature span means that greater detail is displayed with increasing downstream distance. At x/D = 10, the temperature field is relatively symmetric despite the fan-produced swirl. With increasing downstream distance, the temperature distributions become less regular. The radial migration of the wall temperature magnitude in the direction of the axis is believed to have been aided by a radial inward flow driven by a radial pressure difference based on the pressure at the wall exceeding that of the axis (to be shown shortly).

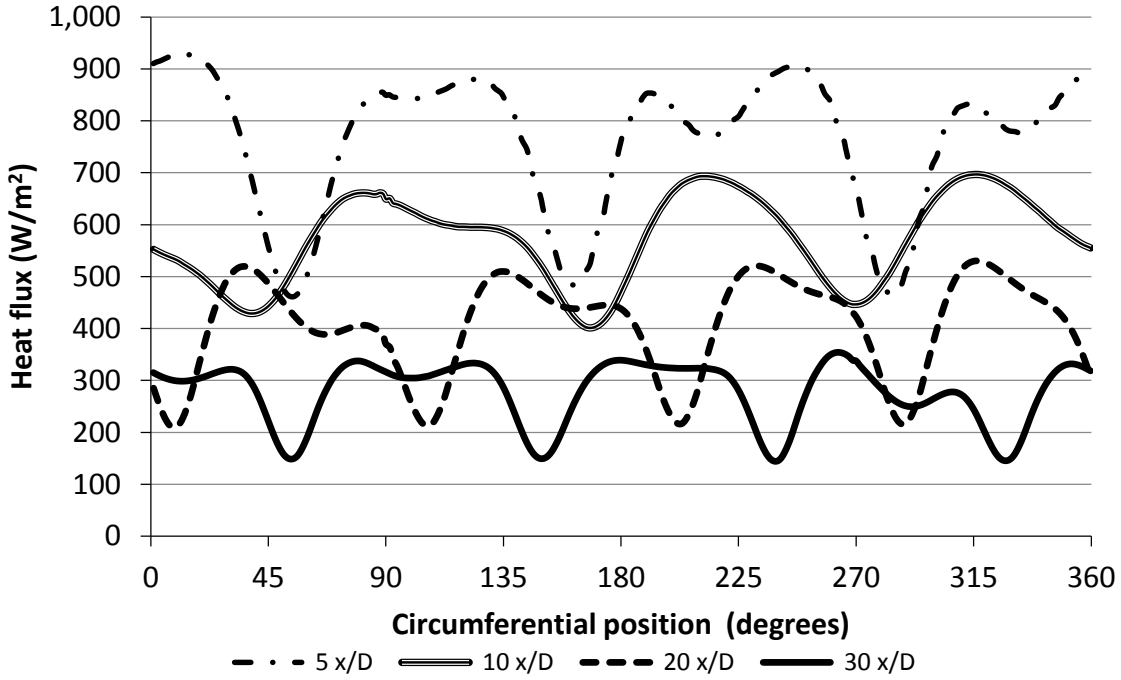

Fig. 4.6: Circumferential variations of the local wall heat flux at selected axial locations for the L/D = 40 pipe.

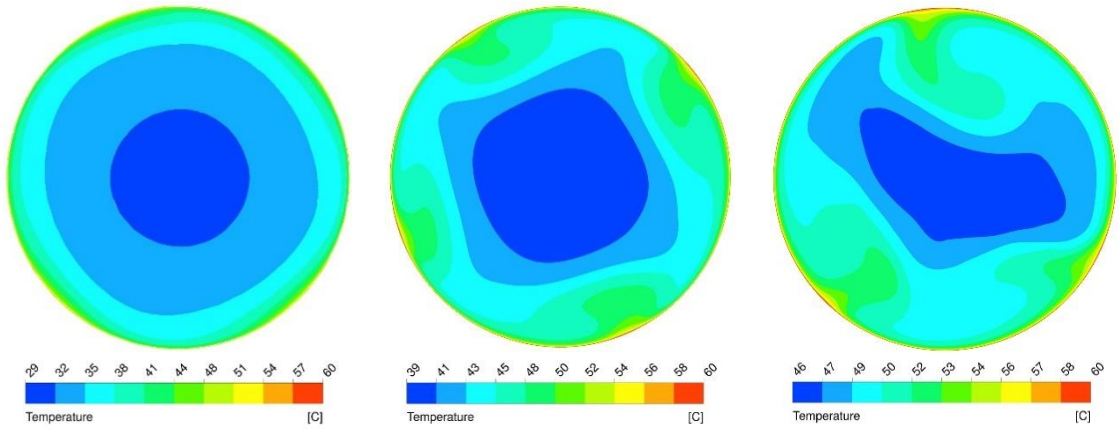

(a) (b) (c)

Fig. 4.7: Color contour diagrams of the fluid temperature for the *L/D* = 60 pipe: *x/D* = (a) 10, (b) 30, and (c) 55.

4.5 Fluid Mechanic Results

There are a number of fluid mechanic results that are of practical relevance. The first to be presented is cross-sectional distribution of the axial velocity at several selected axial locations. This information is displayed in Fig. 4.8. It is noteworthy that just downstream of the fan, the highest axial velocities are in the neighborhood of the pipe wall. This outcome can be directly attributed to the characteristics of the fan. With increasing downstream distance, friction acts to diminish the near-wall velocities with the result that the near-axis part of the cross section inherits the higher velocities. At the most-downstream displayed station, x/D = 50, the cross-sectional velocity distribution is approaching a more normal pattern wherein the lowest velocities are at the pipe wall and the largest velocities are found in the central part.

Of equal relevance is the decay of the swirl velocity that is imparted to the flow by the rotation of the fan blades. To illustrate the decay, focus may be directed to Fig. 4.9 where vector diagrams show the magnitude of the swirl by means of vector length. At the first exhibited station, x/D = 10, it is seen that the magnitude of the swirl increases with increasing distance from the axis of the pipe. The second station, x/D = 30, displays a much diminished swirl magnitude which continues the original radially outward swirl increase. Finally, at the most downstream station, x/D = 55, the swirl magnitude is near the point of vanishing.

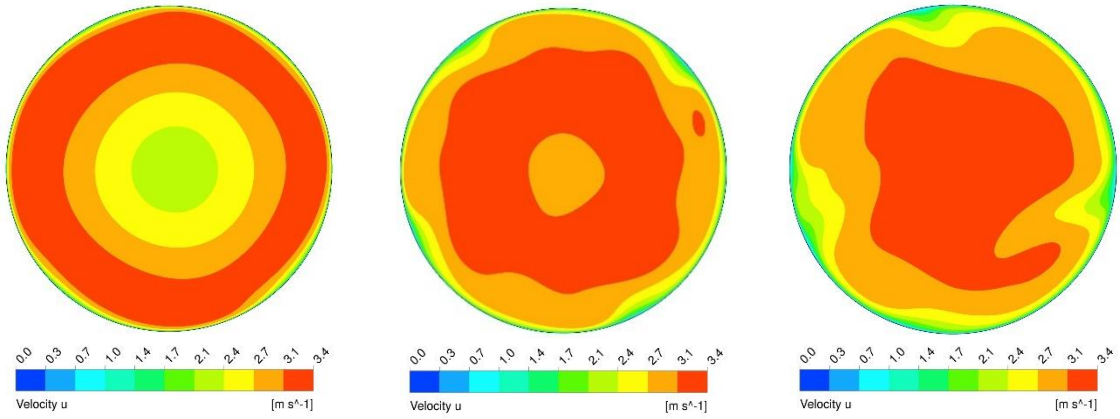

(a) (b) (c)

Fig. 4.8: Color contour diagrams showing the cross-sectional variations of the axial velocity for the *L/D* = 60 pipe: *x/D* = (a) 10, (b) 30, and (c) 50.

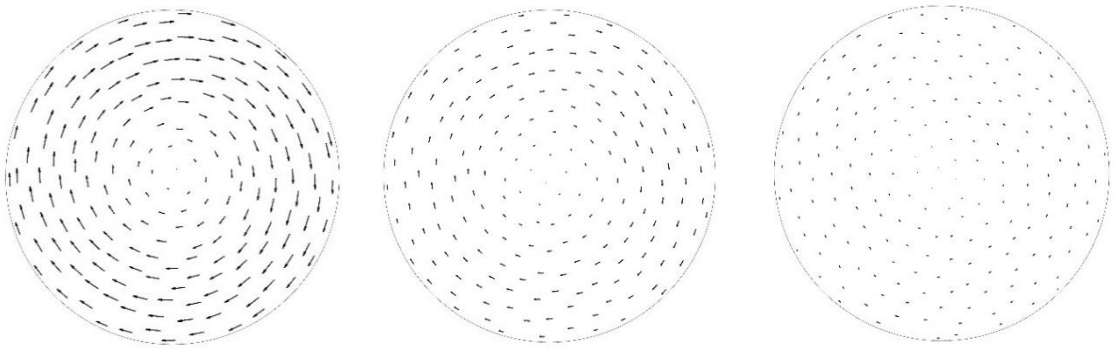

(a) (b) (c)

Fig. 4.9: Vector diagrams showing the magnitude of the swirl velocity for the *L/D* = 60 pipe: *x/D* = (a) 10, (b) 30, and (c) 55.

The cross-sectional variation of the pressure is closely linked to the swirling component of the flow. This link suggests that a tornado-like radial pressure distribution is to be expected, with the lowest pressure at the axis and with pressure increasing radially outward. This expectation is fulfilled by the information conveyed in Fig. 4.10 which displays color contour diagrams of the pressure at three axial stations. Also of note is that the extent of the radial pressure variation decreases with increasing downstream distance as does the swirl itself.

It is noteworthy that the wall shear stress displays an undershoot in common with that for the Nusselt number results of Figs. 4.4 and 4.5. To illustrate the axial variation of the wall shear stress, Fig. 4.11 has been prepared. In the figure, the local circumferentially averaged wall shear stress is plotted as a function of the dimensionless axial coordinate for the three investigated cases. The figure consists a main part and an inset whose function is to magnify the undershoot. Inspection of the figure shows that for the rotating fan case, the shear stress decreases monotonically with increasing downstream distance. However, for the two cases characterized by uniform velocities at the inlet cross section, undershoots of the shear stress are evident.

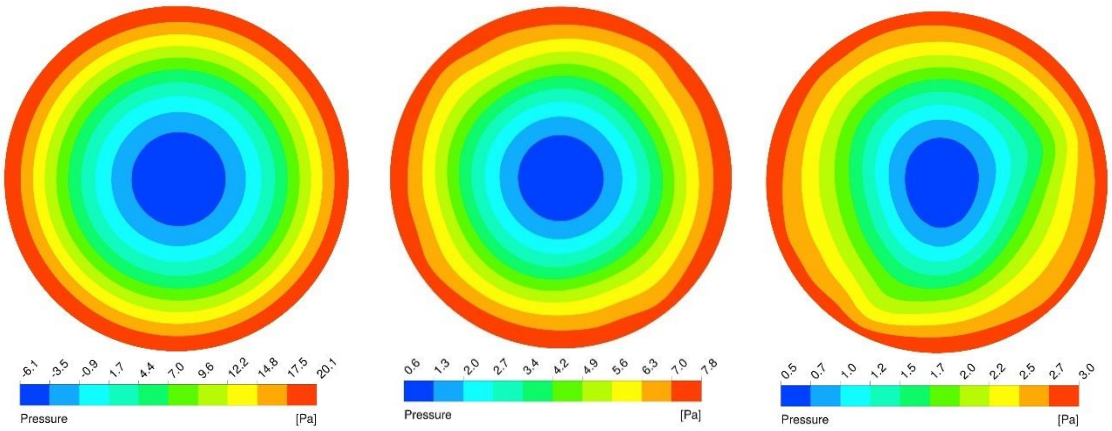

(a) (b) (c)

Fig. 4.10: Color contour diagrams showing cross-sectional pressure variations for the *L/D* = 60 pipe: *x/D* = (a) 10, (b) 30, and (c) 50.

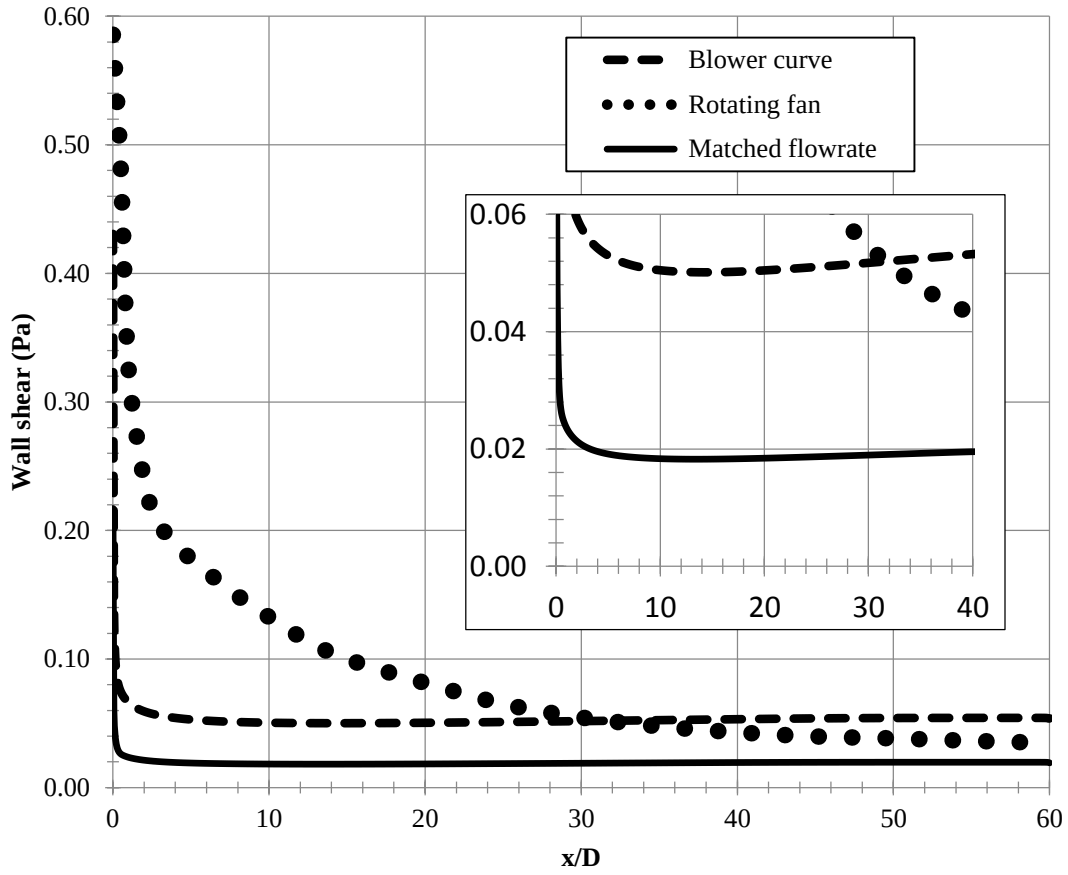

Fig. 4.11: Variation of the circumferential-averaged wall shear stress as a function of the axial coordinate *x/D* for a pipe length *L/D* = 60.

As an expansion of the information conveyed in Fig. 4.11, typical circumferential variations of the wall shear stress at selected axial locations are displayed in Fig. 4.12. It can be seen from the figure that the circumferential variations are major. At each cross section, the ratio of the maximum to the minimum shear stress ranges from about 1.5 to 2.

It is widely understood that axial fans spawn a highly irregular flow marked by vigorous mixing and high turbulence. To extend quantitative support to this understanding, a turbulence metric, the turbulence viscosity μ_{turb} has been evaluated and formed into a dimensionless ratio μ_{turb}/μ, where μ is the ordinary molecular viscosity. If this ratio is close to zero, the flow is laminar. For values of one and larger, turbulence plays a significant role. In order to characterize the fan-created turbulence and to trace its downstream decay, Fig. 4.13 has been created. The figure consists of three panels, each corresponding to an axial location *x/D*. The first panel shows the turbulence at a location slightly downstream of the fan. At that location, the maximum value of μ_{turb}/μ is 366. The decay of turbulence reduces the respective maxima at *x/D* = 30 and 50 to 122 and 80. This outcome provides further testimony to the longevity of swirl.

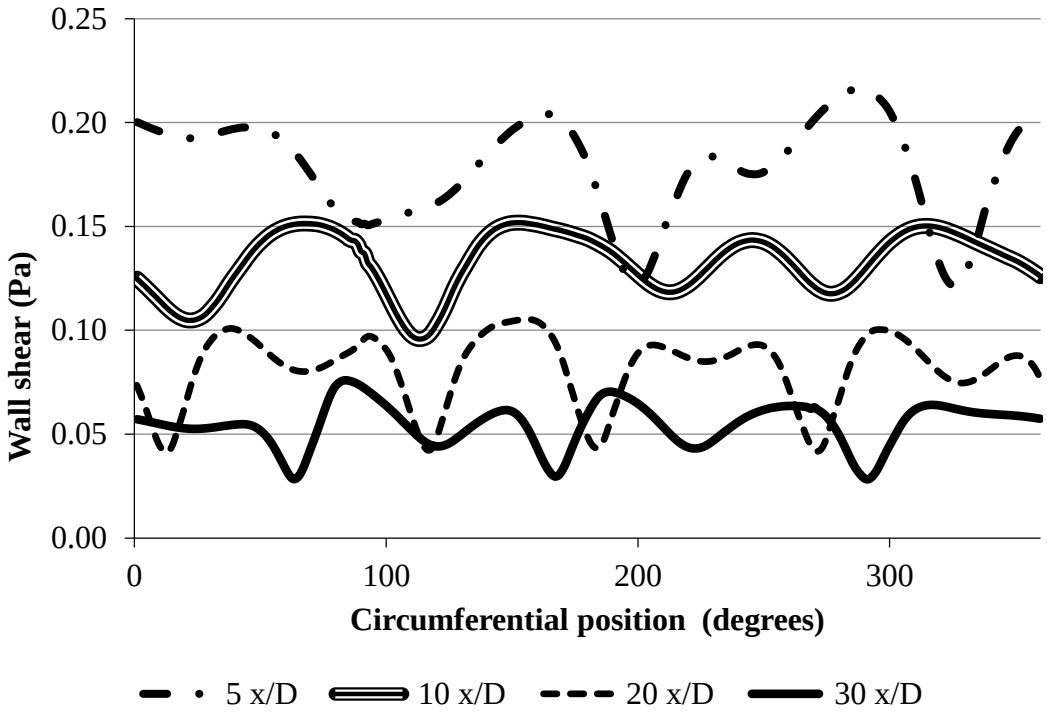

Fig. 4.12: Circumferential variations of the local wall shear stress at selected axial locations for the *L/D* = 40 pipe.

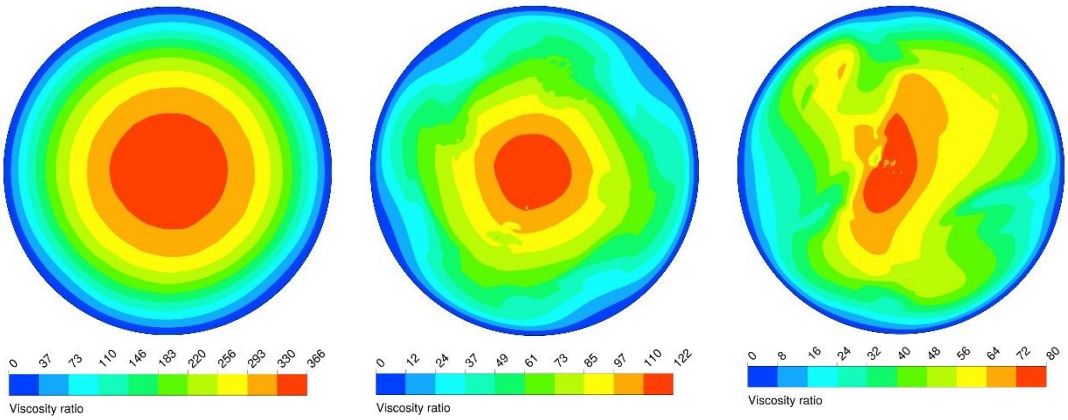

(a) (b) (c)

Fig. 4.13: Color contour diagrams showing cross-sectional variations of the viscosity ratio μ_{turb}/μ for the *L/D* = 60 pipe: *x/D* = (a) 10, (b) 30, and (c) 50.

4.6 Retrospective Summary for Chapter 4

There is a tendency to oversimplify the role of fans as a design component by making use of the blower curve for the fan in question. Careful consideration of the experimental setup used in the determination of a blower curve provides testimony that the complex, highly turbulent flow spawned by the fan is not maintained when the blower curve characteristics are determined. As a consequence, blower curve information is mostly used as a means for quantifying the magnitude of the delivered flow but the true nature of the flow is lost.

In this investigation, the seemingly simple situation of a fan-delivered flow to the inlet of a pipe has been studied by means of a model which takes full account of the rotation of the fan blades and of the true nature of the fan-delivered flow. It is believed that this is the first time that such a realistic approach has been used. In addition to treating the flow delivered by the rotating fan, comparison cases have also been investigated. One of these cases is based on the use of the blower curve for the fan in question, while the second has made use of the flow rate delivered by the rotating fan but modified to be a uniformly distributed, swirl-free flow.

The heat transfer problem was based on a uniform pipe-wall temperature and a different prescribed temperature of the fluid entering the pipe. Not unexpectedly, the wall heat flux varied both circumferentially and axially. Circumferentially averaged heat transfer coefficients were calculated and compared with those based on the use of the blower curve. It was found that the rotating-fan-based heat transfer coefficients were substantially higher than those based on the blower curve, the extent of the enhancement ranging from a factor of two to 50% between $x/D = 0$ and 20.

Cross-sectional temperature distributions at selected axial stations were displayed and interpreted. The movement of heat from the wall towards the axis of the pipe was conjectured to be enhanced by a pressure-driven radial inward flow. The axial velocity distributions showed a strong influence of the fan. In particular, in the cross sections just

downstream of the fan, the highest axial velocities occurred in the neighborhood of the wall.

Of particular interest is the strength and decay of the fan-imparted swirl. The swirl created a tornado-like tangential velocity distribution over the cross section such that the highest velocities were greatest in the neighborhood of the wall and least near the axis. This swirl distribution gave rise to a strong radial pressure variation, with the lowest pressures near the axis and the highest pressures near the wall.

The highly turbulent flow spawned by the rotating fan was quantitatively characterized, and the decay of the turbulence with increasing downstream distance was also quantified. The circumferentially averaged wall shear stress generally decayed with increasing downstream distance. However, for the comparison cases based on uniform inlet velocities and no swirl, the axial variation of the circumferentially averaged wall shear stress undershot the fully developed value.

Chapter 5

RETROSPECTIVE SUMMARY OF CONVECTIVE HEAT TRANSFER MODELING AND SIMULATION IN THE PRESENCE OF SWIRLING FLOWS

5.1 Concluding Remarks

The underlying motivation for this thesis work is to elucidate and clarify a fundamental issue in convective heat transfer. It is well recognized that there is an intimate relationship between fluid flow and convective heat transfer. In a course that I have taken, I recall a professor saying that the relationship between convective heat transfer and fluid flow is similar to the relationship between an orchestra and dancers. If the orchestra increases the tempo, those who wish to dance must dance faster. On the other hand, if the orchestra reduces the tempo, the dancers must follow suit or not dance.

It is an obvious realization that in order to obtain correct values for convective heat transfer, the velocity-field solution that is used in accordance with the governing equations of convective heat transfer must also be correct. In this context, the word "correct" means being in accord with reality and not simply correct within the adopted fluid-flow model. The laws of nature encompass not only the governing differential equations, but also the boundary conditions for any numerical simulation. Boundary conditions are always necessary prerequisite to model physical processes expressed by the governing differential equations, regardless of the specific problem of interest. It is the message of the thesis that the consistent use of certain universal inlet fluid-flow boundary conditions for pipe and duct flows has led to a plethora of results for the heat transfer coefficient that do not coincide with physical reality. This inlet boundary condition, namely a *flat* or *uniform* velocity profile, is still the most frequently encountered boundary condition in the published literature today.

A careful, but necessarily incomplete, survey of widely accepted and well-known fluid mechanic and heat transfer textbooks, from the last 50 years, written in any and all languages indicates that it is uniformly assumed that the flow entering a pipe or duct

possesses a uniform inlet velocity profile. This uniform profile assumption extends beyond textbooks and very often in contemporary papers and publications. This assumption appears to be mostly ignored and not yet fully questioned in a definitive manner.

Aside from engineering logic and understanding physically realistic fluid flow behavior, there are mathematically-founded reasons to have suspicions about the veracity of this inlet velocity profile. One such reason is a conflict between such a profile and the no-slip boundary condition at solid bounding walls. If the velocity profile were truly flat, the velocity at the wall would be non-zero, an outcome in direct conflict with the no-slip condition. This conflict can be regarded as a mathematical singularity right at the inlet boundary.

There have been attempts to reproduce a flat velocity profile in the laboratory because of the corresponding advantage associated with simplifying the flow profile. One suggested approach is to suction off any boundary layer development that may have occurred upstream of the inlet cross section. Implementation of this idea is a very delicate activity which would hardly relate to engineering practice. The vacuum or suction would have to be precisely tuned in order to prevent significant disturbance to the main flow.

Thin, but not vanishing, boundary layers at the inlet cross section can be achieved by the use of upstream flow-delivery devices. For example, a conical contraction having a large ratio of inlet to exit cross sectional area can yield a very thin boundary layer at its exit. Another device which delivers a thin inlet-section boundary layer is a bellmouth shaped flow nozzle geometry formed by quarter ellipsoids having a large ratio of the major axis to the minor axis. Although these are known techniques, they are rarely used for constructing uniform velocity boundaries in textbooks or industry practice.

In the Chapter 4 of this thesis, it has been shown that the use of a uniform inlet velocity profile can lead to major errors in the heat transfer coefficients computed from fluid-flow solutions based on that profile. The situation dealt with there was an inlet fluid flow to a

circular pipe that was driven by a rotating fan. The fan rotation gives rise to a swirling motion superimposed on the axial flow.

To quantify the heat transfer errors that would accrue from the use of a flat, swirl-free inlet velocity profile, numerical simulations were performed and heat transfer results obtained by means of the currently standard model of prediction. That model makes use of a manufacturer-supplied fan curve or P-Q curve in which the fan pressure rise is plotted as a function of the volumetric flow output of the fan. The fan curve enables a velocity magnitude to be selected (from the volumetric flowrate) if the corresponding overall system pressure drop is known or determined. Common practice, as witnessed by the published literature, further assumes that that velocity is uniformly distributed across the inlet cross section of the pipe or heat exchanger. The logic of the aforementioned approach is believed to be flawed. Whenever an axial fan is used as a fluid mover, swirl is inevitable. Therefore, if a fan curve is used to obtain velocity magnitudes, it defies logic to ignore the swirl created by the fan. Since the resulting swirling flow is a result of a fan's specific blade design, it is not possible to prescribe a universal swirling velocity component to inlet boundaries. The inventible outcome is that the entire fan has to be modeled to capture the realistic fluid mechanics.

It is interesting to look back retrospectively with a view toward understanding this logical disconnect between physical reality and modeling practice. Since the typical flow leaving the exit plane of an axial fan is extremely complex and highly distorted due to swirl, backflow flow, and eddies, it was somehow recognized and judged impossible to measure the flow rate and the pressure rise produced by the fan by making measurements at the exit plane. To remedy this realization, one or more technical societies of practitioners established a widely accepted protocol for determining pressure-rise and flow rate relationships. In brief, that protocol involves passing the outflow of the fan through an array of screens, perforated plates, and flow straighteners. The thus-calmed flow is then utilized for flow and pressure measurements, and subsequently formed into a fan curve (P-Q curve or blower curve). It is the opinion of the author that the calmed flow is sufficiently

different from the flow that is actually produced and that the pressure and flow rate measured for the former is not assignable to the former.

Another concern relevant to the manufacturer-supplied fan curve is recent evidence that the output of an axial fan supplying air to a large fluid-flow resistance is different from that which corresponds to the fan discharging into free unobstructed space, as is the case when the fan's characteristics are measured. These considerations bear further witness to the author's opinion that the currently standard practice of using manufacturer-supplied fan curve information as input to heat transfer solutions is highly error prone.

On the simulation-side of engineering problem solving for convective heat transfer, it was not until the most recent years that computational power (hardware) and numerical capabilities (software) have been as amply available to practitioners and researchers. The earliest numerical works were very much limited in both hardware and software, which ultimately predicated the need for simplified modeling techniques. This need for simplicity allowed the uniform velocity profile to remain prevalent and migrate from the realm of analytical solutions to the reality of numerical analysis and simulation. Once established in the minds of practitioners of numerical simulations, the uniform velocity profile has become the most common, unquestioned and acceptable, inlet boundary condition.

The foregoing paragraphs have sharply highlighted the major message of this thesis and provided a qualitative historical-glimpse of the reasons for the present state-of-the-art. The outcome is that accurate heat transfer results are strongly dependent on the fidelity of inputted velocity solutions to coincide with realistic physical situations.

Other specific accomplishments in this thesis will now be identified. With regard to Chapter 2, a gold-standard approach for the verification of numerical-simulation solutions was established. In particular, a proper comparison of numerical predictions and experimental data requires a greater amount of experimental information than is usually available in the published literature. Within a narrow range of the published literature, it is

common to execute numerical simulations which utilize inlet velocity profiles provided by experimental measurements. However, if the fluid flow is turbulent, knowledge of inlet-section velocity profiles is not sufficient to fully describe the flow. What is needed is information about the state of turbulence of the flow at the inlet section. It is very rare that verifications of simulation results has taken note of this requirement. It is also difficult to obtain the needed turbulence quantities from experiments or published data. Typically, the verification performed by others in the published literature has to be satisfied with comparison solely based on information about the inlet velocity profiles. The verification set forth here in Chapter 2 has set a very high standard of accuracy of numerical simulation that pervades the entire thesis.

It was found in Chapter 2 that among the investigated two-equation turbulence models, the *SST* κ-ω model predicted axial and circumferential velocity profiles that agreed best with the chosen experiments. Of particular important, with respect to heat transfer applications, is that the *SST* model predictions of the velocities near the wall of the apparatus were especially excellent compared with the predictions of the other models. Since convective heat transfer is very sensitive to the near-wall velocity field, and this outcome augurs well for the determination of heat transfer predictions in swirl-flow situations when the *SST* κ-ω model is used. The velocity profile predictions obtained from the LES turbulence model were slightly in better agreement with the experimental data than were those from the SST κ-ω model. However, enormous difference in the CPU time required to obtain a solution by use of these respective methods made the SST κ-ω model is the most appropriate of those investigated here.

The investigation of the fluid mechanics and convective heat transfer of the biomedical diagnostic device in Chapter 3 illustrates the need for a higher depth of understanding of physical processes than is usually brought to bear in the design of this category of device. When a numerical simulation is performed using commercially available software, the discretized governing partial differential equations usually contain all of the participating physical processes. Normally, such investigations are performed by researchers whose

understanding of the fluid mechanics and heat transfer processes is rudimentary. It is believed that Chapter 3 stands as a model of how best to approach the design of such devices. The entire system was successfully modeled, including the rotating fan blades, with the participating heat transfer fins.

From the heat transfer literature, little attention has been given to the effect of turbulence levels on convective heat transfer coefficients. Therefore, only intuitive-based comments are possible. It is the belief of the author that the relatively low values of the μ_{turb}/μ ratio, present in the analysis of Chapter 3, impose a penalty on the heat transfer rates that are possible in this device. This outcome suggests the need to a redesign which accentuates the turbulence level.

Chapter 4 provides a vehicle for evaluating the extent of the inaccuracies that occur when the presently standard approach to convective heat transfer predictions is utilized. In that regard, it may be recalled that that approach is based on the use of a fan curve supplied by the manufacturer of the fan plus the additional assumption that the volumetric flow rate determined from the manufacture supplied fan curve is uniformly distributed across the inlet cross section of the heat exchange device. The issue of the attainment of a uniform inlet profile for pipe flow has been broadly discussed in Chapter 4, where it was concluded that such a profile is unlikely in real-world applications. Also relevant is that the simulation model employed there enabled a proper accounting of the nature of the turbulence delivered by the fan to the inlet of the pipe. As noted in connection with Chapter 2, it is unlikely that a numerical simulation can yield accurate fluid flow results for turbulent flow unless quantitative specification of the nature of the turbulence at inlet is provided. This realization is another of the major outcomes of the thesis research.

In Chapter 4, circumferentially averaged heat transfer coefficients were calculated and compared with those based on the use of the blower curve. It was found that the rotating-fan-based heat transfer coefficients were substantially higher than those based on the blower curve, the extent of the enhancement ranging from a factor of two to 50% between

x/D = 0 and 20. Cross-sectional temperature distributions at selected axial stations were displayed and interpreted. Of particular interest is the strength and decay of the fan-imparted swirl. The swirl created a tornado-like tangential velocity distribution over the cross section such that the highest velocities were greatest in the neighborhood of the wall and least near the axis.

REFERENCES

[1] Davis, P. L., A. T. Rinehimer, and M. Uddin. "A comparison of RANS-based turbulence modeling for flow over a wall-mounted square cylinder." In *20th Annual Conference of the CFD Society of Canada, Canmore, AL, Canada, May*, pp. 9-12. 2012.

[2] Meslem, Amina, Florin Bode, Cristiana Croitoru, and Ilinca Nastase. "Comparison of turbulence models in simulating jet flow from a cross-shaped orifice." *European Journal of Mechanics-B/Fluids* 44 (2014): 100-120.

[3] Zhang, Zhao, Wei Zhang, Zhiqiang John Zhai, and Qingyan Yan Chen. "Evaluation of various turbulence models in predicting airflow and turbulence in enclosed environments by CFD: Part 2—Comparison with experimental data from literature." *Hvac&R Research* 13, no. 6 (2007): 871-886.

[4] Li, Weihong, Jing Ren, Jiang Hongde, Yigang Luan, and Phillip Ligrani. "Assessment of six turbulence models for modeling and predicting narrow passage flows, part 2: Pin fin arrays." *Numerical Heat Transfer, Part A: Applications* 69, no. 5 (2016): 445-463.

[5] Engdar, Ulf, and Jens Klingmann. "Investigation of two-equation turbulence models applied to a confined axis-symmetric swirling flow." In *ASME 2002 Pressure Vessels and Piping Conference*, pp. 199-206. American Society of Mechanical Engineers, 2002.

[6] Lai, Yong G. "Predictive capabilities of turbulence models for a confined swirling flow." *AIAA journal* 34, no. 8 (1996): 1743-1745.

[7] Sharif, M. A. R., and Y. K. E. Wong. "Evaluation of the performance of three turbulence closure models in the prediction of confined swirling flows." *Computers & fluids* 24, no. 1 (1995): 81-100.

[8] Xia, J. L., G. Yadigaroglu, Y. S. Liu, J. Schmidli, and B. L. Smith. "Numerical and experimental study of swirling flow in a model combustor." *International journal of heat and mass transfer* 41, no. 11 (1998): 1485-1497.

[9] Clausen, P. D., S. G. Koh, and D. H. Wood. "Measurements of a swirling turbulent boundary layer developing in a conical diffuser." *Experimental Thermal and Fluid Science* 6.1 (1993): 39-48.

[10] Launder, B.E.; Spalding, D.B. (March 1974). "The numerical computation of turbulent flows". *Computer Methods in Applied Mechanics and Engineering* **3** (2): 269–289

[11] Yakhot, V., Orszag, S.A., Thangam, S., Gatski, T.B. & Speziale, C.G. (1992), "Development of turbulence models for shear flows by a double expansion technique", Physics of Fluids A, Vol. 4, No. 7, pp1510-1520.

[12] Wilcox, D. C. (1988). Multiscale model for turbulent flows. *AIAA journal*, *26*(11), 1311-1320.

[13] F. R. Menter, Two-equation eddy-viscosity turbulence models for engineering applications, AIAA Journal 32 (8) (1994) 1598-1605.

[14] Nicoud, Franck, and Frédéric Ducros. "Subgrid-scale stress modelling based on the square of the velocity gradient tensor." *Flow, turbulence and Combustion* 62.3 (1999): 183-200.

[15] Zhang, C., & Xing, D. (2010). Microfluidic gradient PCR (MG-PCR): a new method for microfluidic DNA amplification. *Biomedical microdevices*, *12*(1), 1-12.

[16] Cohen, D. A., Banerji, S., & Denninger, M. J. (2006). *U.S. Patent No. 7,051,536*. Washington, DC: U.S. Patent and Trademark Office.

[17] Qiu, X., & Yuan, J. (2006, January). Temperature control for PCR thermocyclers based on Peltier-effect thermoelectric. In *Engineering in Medicine and Biology Society, 2005. IEEE-EMBS 2005. 27th Annual International Conference of the* (pp. 7509-7512). IEEE.

[18] Pal, D., & Venkataraman, V. (2002). A portable battery-operated chip thermocycler based on induction heating. *Sensors and Actuators A: Physical*, *102*(1), 151-156.

[19] Agrawal, N., & Ugaz, V. M. (2007). A buoyancy-driven compact thermocycler for rapid PCR. *Clinics in laboratory medicine*, *27*(1), 215-223.

[20] Heimberg, W., Hermann, T., Knulle, M., Schurf, M., & Wagner, T. (2009). *U.S. Patent No. 7,611,674*. Washington, DC: U.S. Patent and Trademark Office.

[21] Atwood, J. G., Fawcett, A., Ferrara, K. S., Hetherington, P. M., Noreiks, R. W., Olsen, D. E., Widomski, J. R. & Wittmer, C. M. (2012). *U.S. Patent No. 8,246,243*. Washington, DC: U.S. Patent and Trademark Office.

[22] Stanley, K., & Corbett, J. (2012). *U.S. Patent No. 8,124,413*. Washington, DC: U.S. Patent and Trademark Office.

[23] Zoltan, B. J., & Leese, R. A. (1982). *U.S. Patent No. 4,312,835*. Washington, DC: U.S. Patent and Trademark Office.

[24] Brown, L. R. (2003). *U.S. Patent No. 6,657,169*. Washington, DC: U.S. Patent and Trademark Office.

[25] S.K. Agarwal, M. Raja Rao, Heat transfer augmentation for the flow of a viscous liquid in circular tubes using twisted tape inserts, Int. J. Heat Mass Transf. 39 (1996) 3547-3557.

[26] R.M. Manglik, A.E. Bergles, Swirl flow heat transfer and pressure drop with twisted-tape inserts, Adv. Heat Transfer 36 (2003) 183-266.

[27] S. Eiamsa-Ard, K. Wongcharee, S. Sripattanapipat, 3-D Numerical simulation of swirling flow and convective heat transfer in a circular tube induced by means of loose-fit twisted tapes, Int. Commun. Heat Mass Transf. 36 (2009) 947-955.

[28] R. Beigzadeh, M. Rahimi, M. Parvizi, S. Eiamsa-ard, Application of ANN and GA for the prediction and optimization of thermal and flow characteristics in a rectangular channel fitted with twisted tape vortex generators, Numer. Heat Tr. A-Appl. 65 (2014) 186-199.

[29] E.Y. Rios-Iribe, M.E. Cervantes-Gaxiola, E. Rubio-Castro, J.M. Ponce-Ortega, M.D. González-Llanes, C. Reyes-Moreno, O.M. Hernández-Calderón, Heat transfer analysis of a non-Newtonian fluid flowing through a circular tube with twisted tape inserts, Appl. Therm. Eng. 84 (2015) 225-236.

[30] B.A. Saraç, T. Bali, An experimental study on heat transfer and pressure drop characteristics of decaying swirl flow through a circular pipe with a vortex generator, Exp. Therm. Fluid Sci. 32 (2007) 158-165.

[31] M. Ahmadvand, A.F. Najafi, S. Shahidinejad, An experimental study and CFD analysis towards heat transfer and fluid flow characteristics of decaying swirl pipe flow generated by axial vanes, Meccanica 45 (2010) 111-129.

[32] A.E. Zohir, A.G. Gomaa, Heat transfer enhancement through sudden expansion pipe airflow using swirl generator with different angles, Exp. Therm. Fluid Sci. 45 (2013) 146-154.

[33] W. Duangthongsuk, S. Wongwises, An experimental investigation of the heat transfer and pressure drop characteristics of a circular tube fitted with rotating turbine-type swirl generators, Exp. Thermal Fluid Sci. 45 (2013) 8–15.

[34] H. Seo, S.D. Park, S.B. Seo, H. Heo, H., I.C. Bang, Swirling performance of flow-driven rotating mixing vane toward critical heat flux enhancement, Int. J. Heat Mass Transf. 89 (2015) 1216-1229.

[35] E.M. Sparrow, A. Chaboki, Swirl-affected turbulent fluid flow and heat transfer in a circular tube, ASME J. Heat Transf. 106 (1984) 766-773.

[36] E.M. Sparrow, J.M. Gorman, J.P. Abraham, Quantitative assessment of the overall heat transfer coefficient U, ASME J. Heat Transfer, 135 (2013) 061102.

[37] Y. Bayazit, E.M. Sparrow, D.D. Joseph, Perforated plates for fluid management: plate geometry effects and flow regimes, Int. J. Therm. Sci. 85 (2014) 104-111.

[38] A. Li, X. Chen, L. Chen, Numerical investigations on effects of seven drag reduction components in elbow and T-junction close-coupled pipes, Build. Serv. Eng. Res. T. 36 (2015) 295-310.

[39] S.W. Churchill, A reinterpretation of the turbulent Prandtl number, Ind. Eng. Chem. Res. 41 (2002) 6393-6401.

[40] W.M. Kays, Turbulent Prandtl number—where are we?, ASME J. Heat Transf. 116 (1994) 284-295.

[41] A.F. Mills, Experimental investigation of turbulent heat transfer in the entrance region of a circular conduit, J. Mech. Eng. Sci. 4 (1962) 63-77.

[42] F. Kreith, M. Bohn, Principles of Heat Transfer (6th ed.), Boston, MA: Brooks/Cole (2001).

APPENDIX A: Heat flux contour diagrams

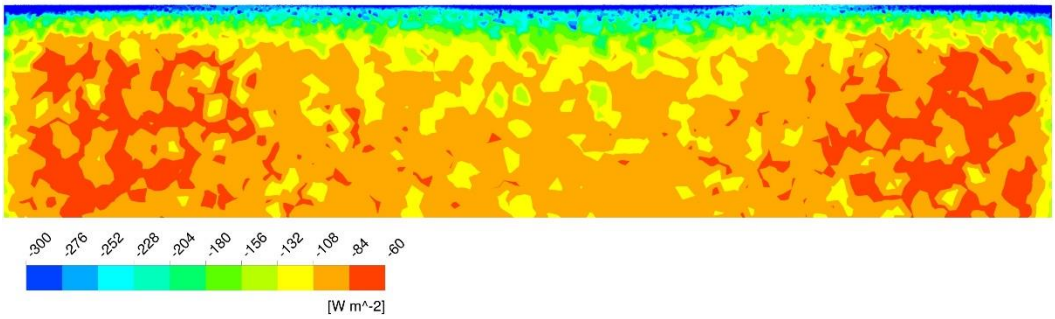

Fin 1, Side A

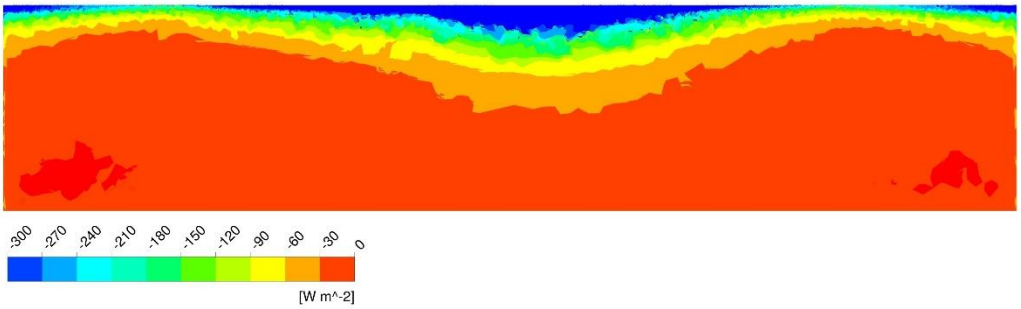

Fin 1, Side B

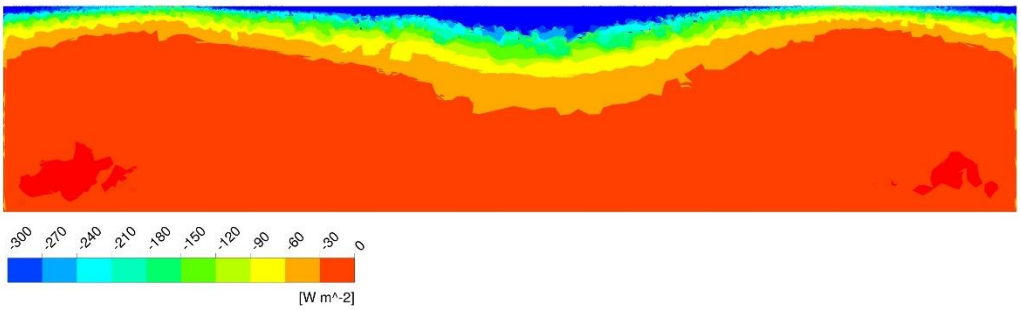

Fin 2, Side A

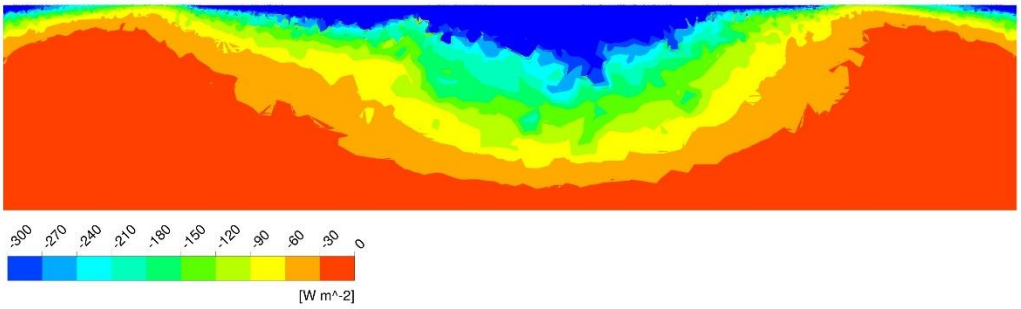

Fin 2, Side B

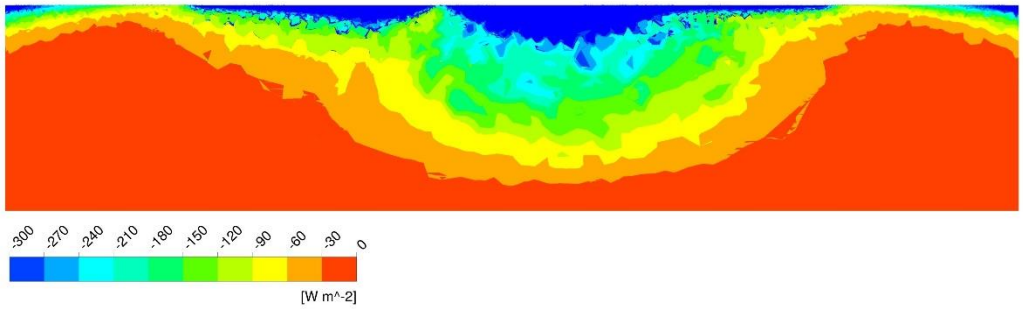

Fin 3, Side A

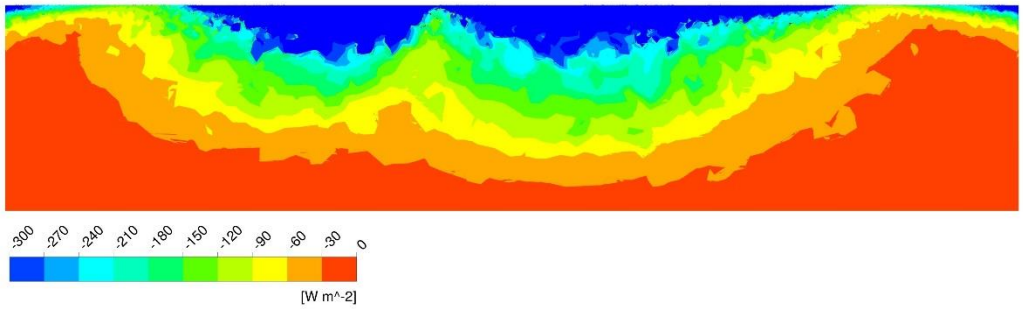

Fin 3, Side B

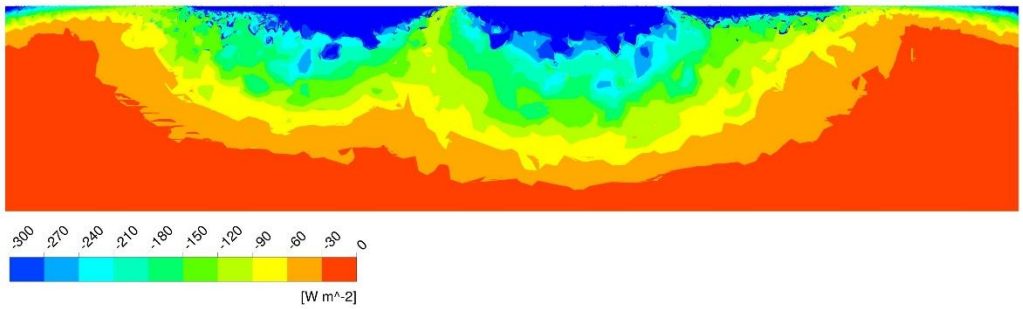

Fin 4, Side A

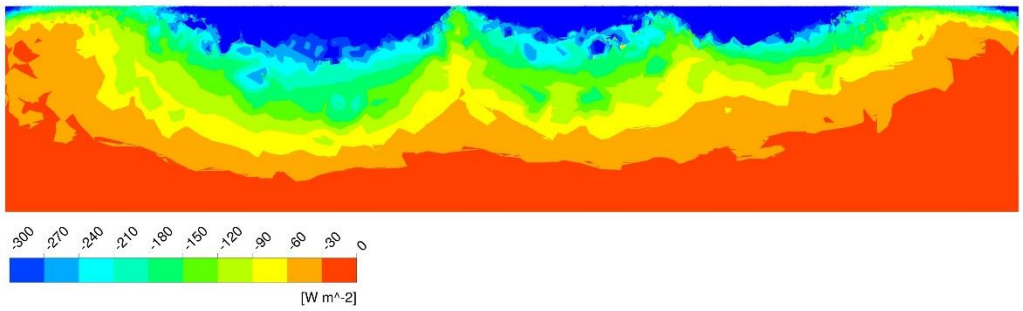

Fin 4, Side B

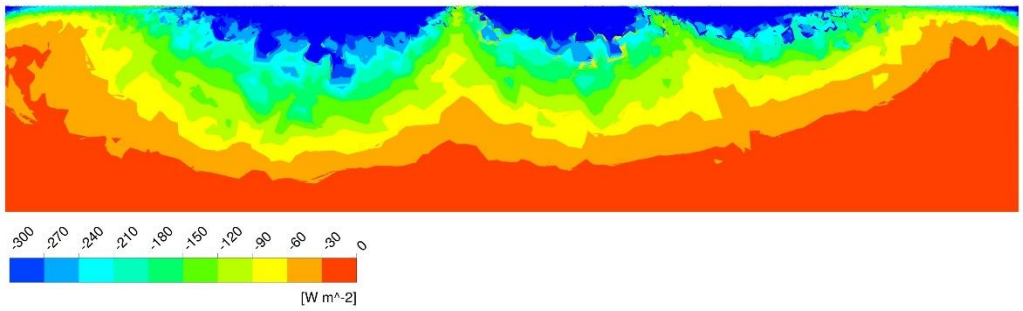

Fin 5, Side A

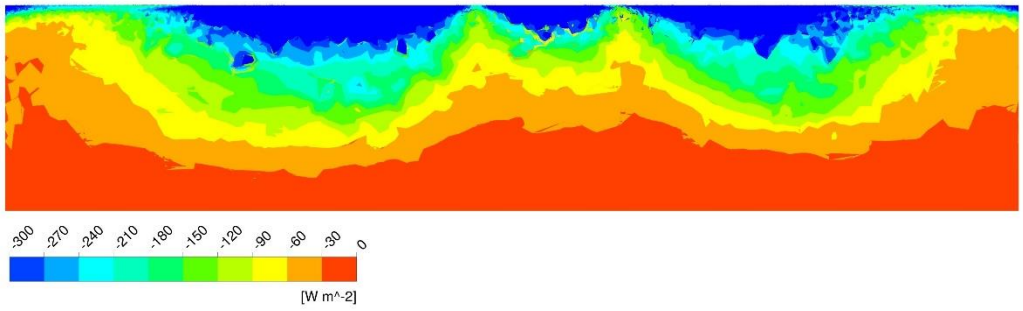

Fin 5, Side B

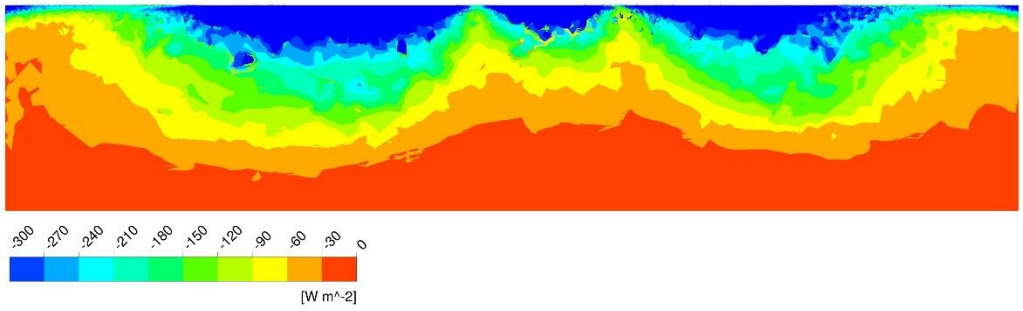

Fin 6, Side A

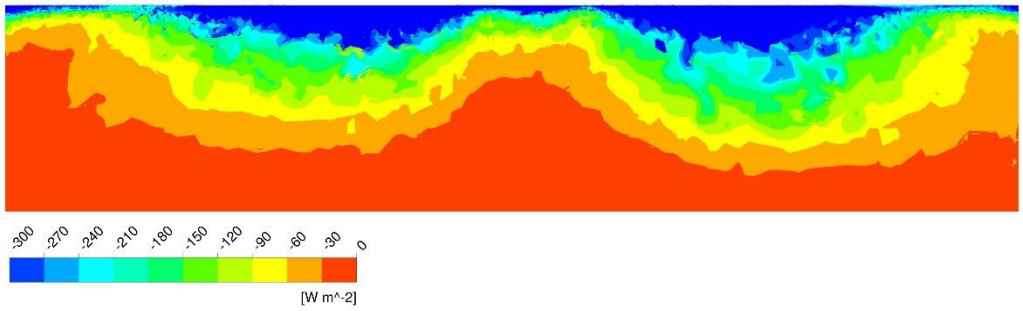

Fin 6, Side B

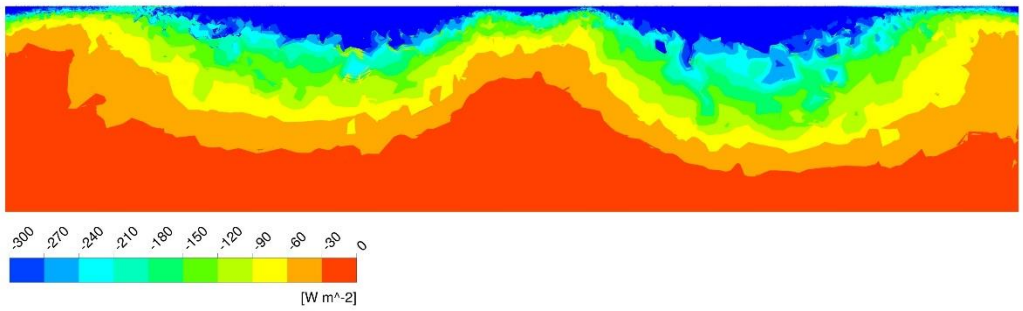

Fin 7, Side A

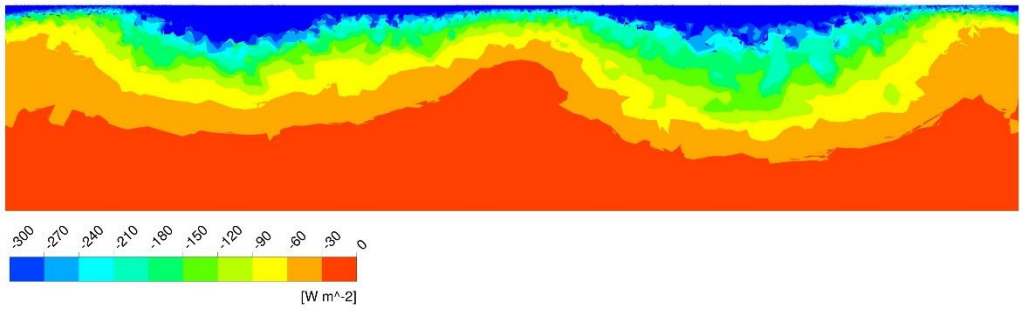

Fin 7, Side B

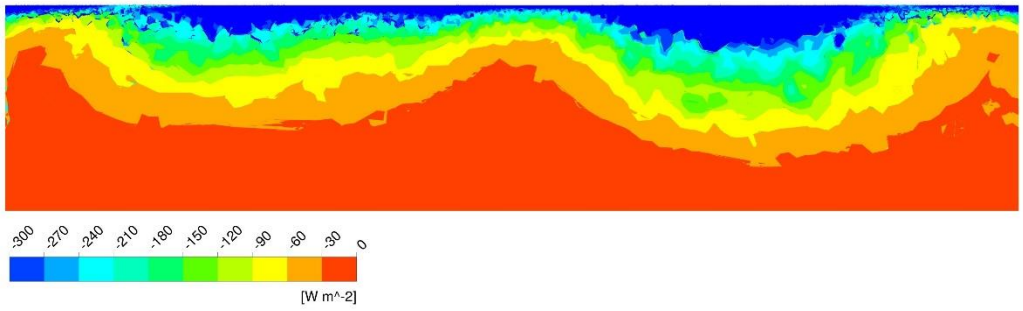

Fin 8, Side A

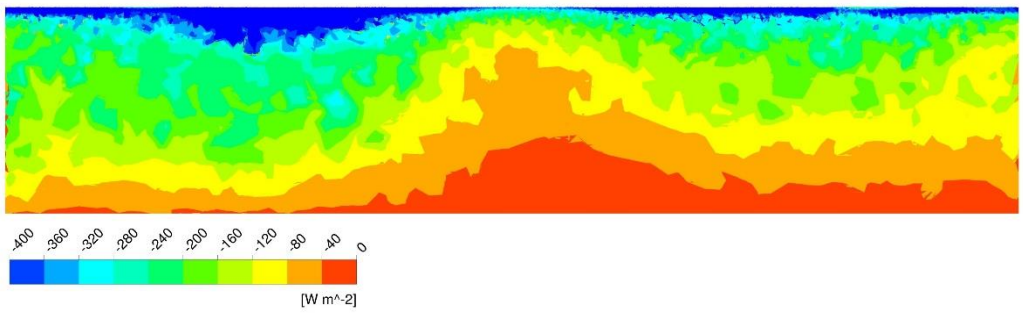

Fin 8, Side B

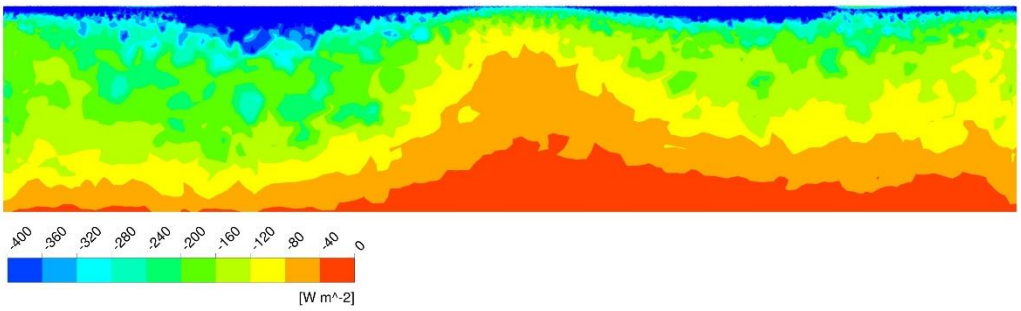

Fin 9, Side A

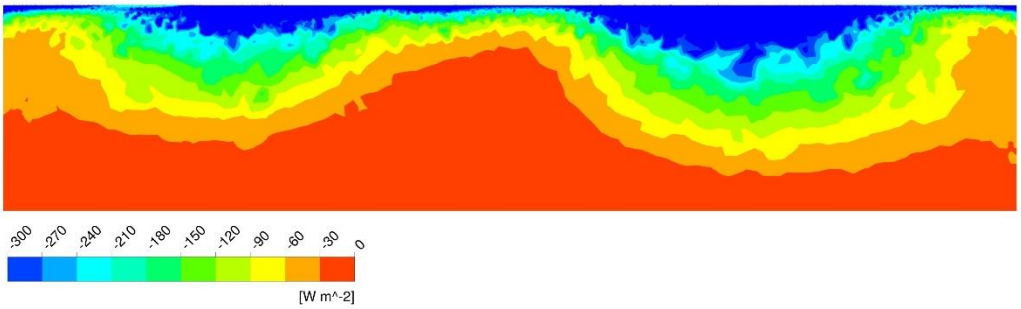

Fin 9, Side B

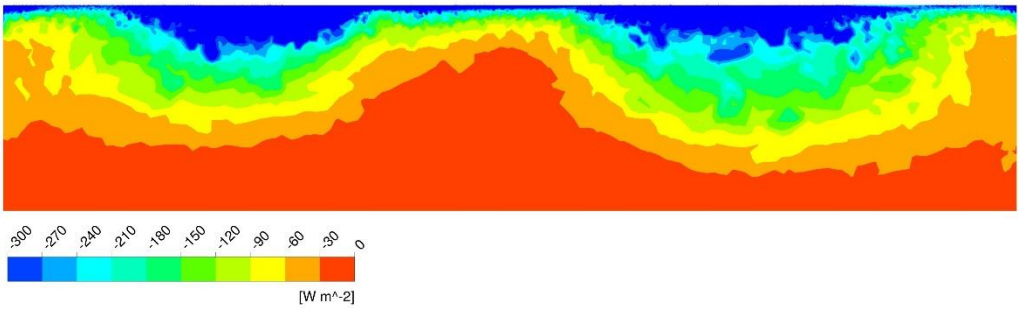

Fin 10, Side A

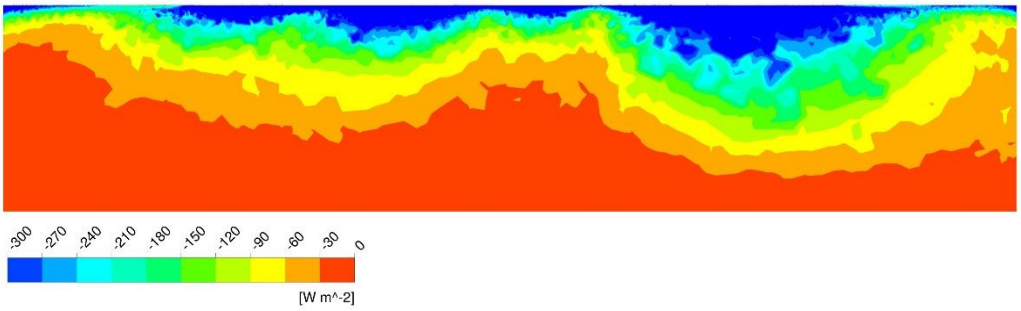

Fin 10, Side B

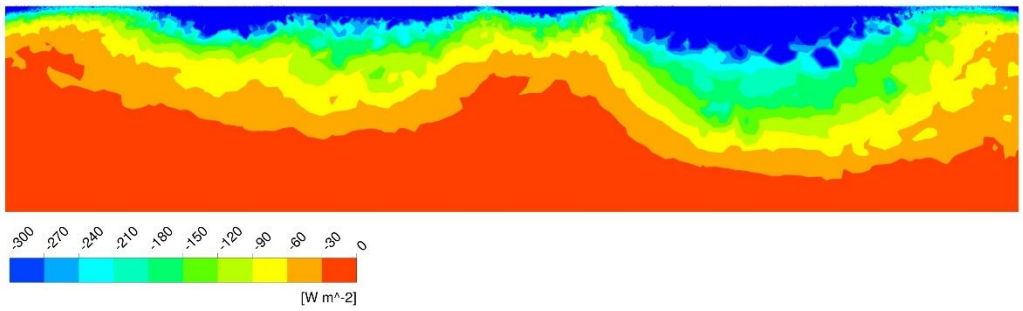

Fin 11, Side A

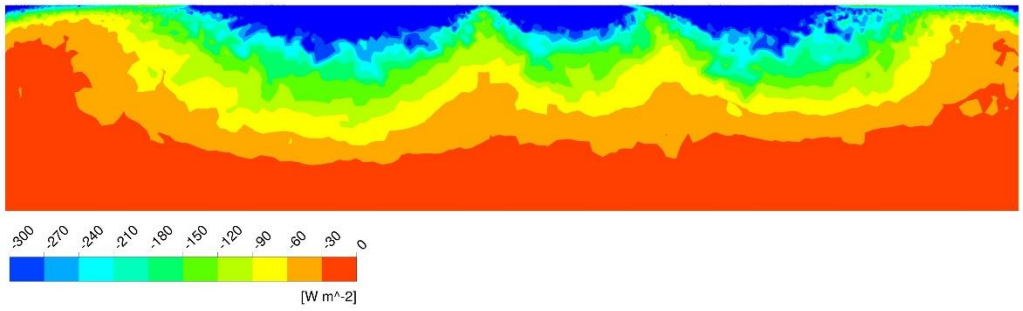

Fin 11, Side B

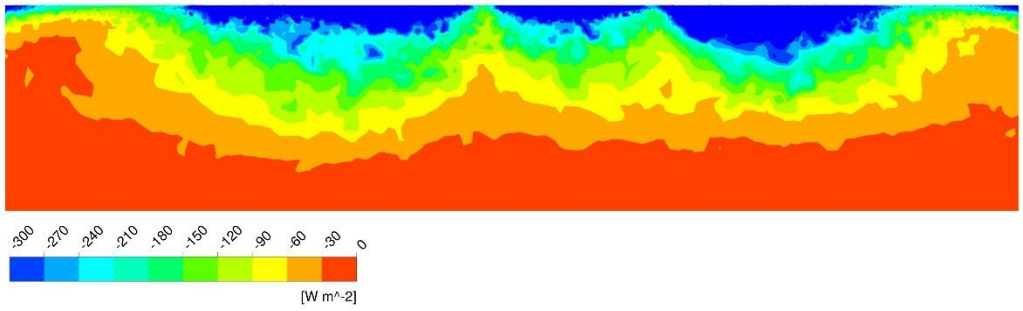

Fin 12, Side A

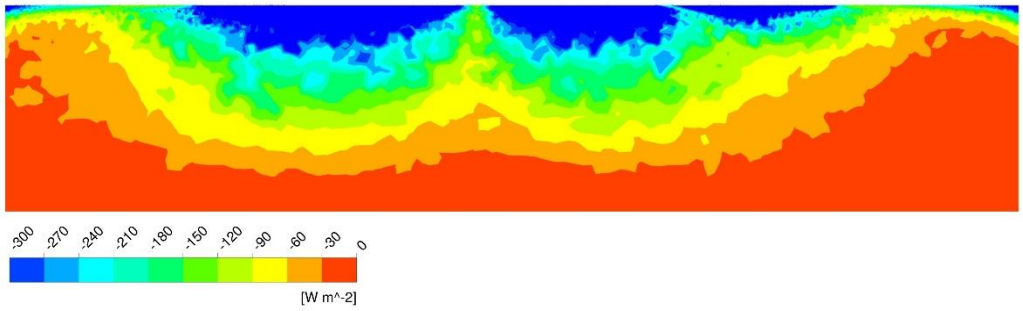

Fin 12, Side B

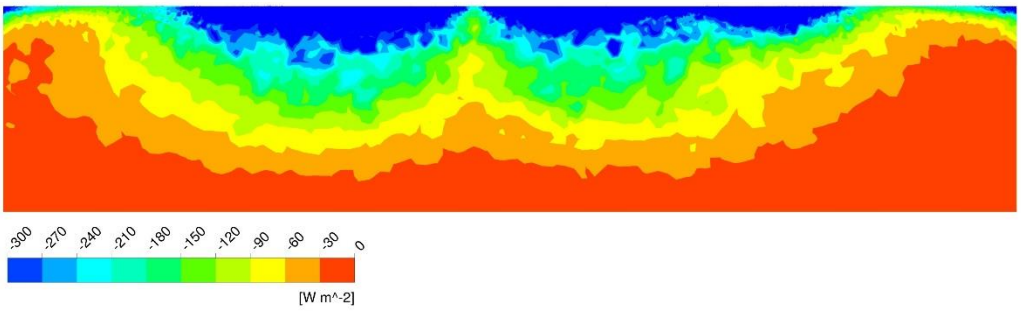

Fin13, Side A

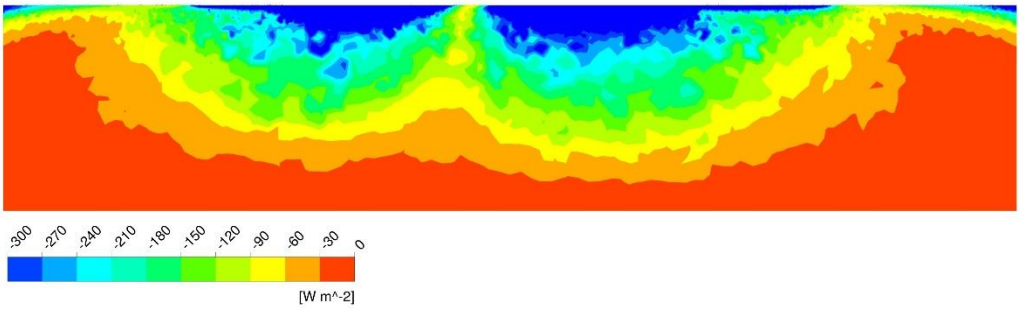

Fin 13, Side B

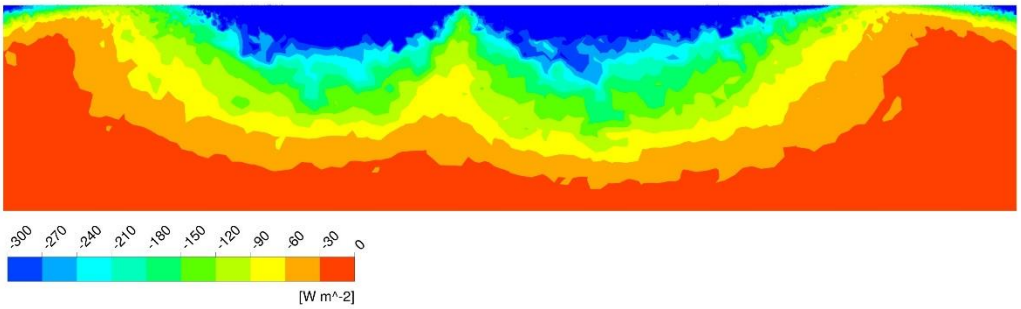

Fin 14, Side A

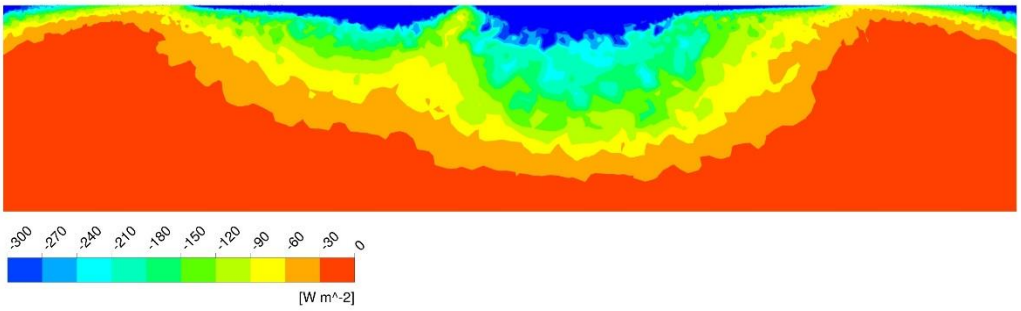

Fin 14, Side B

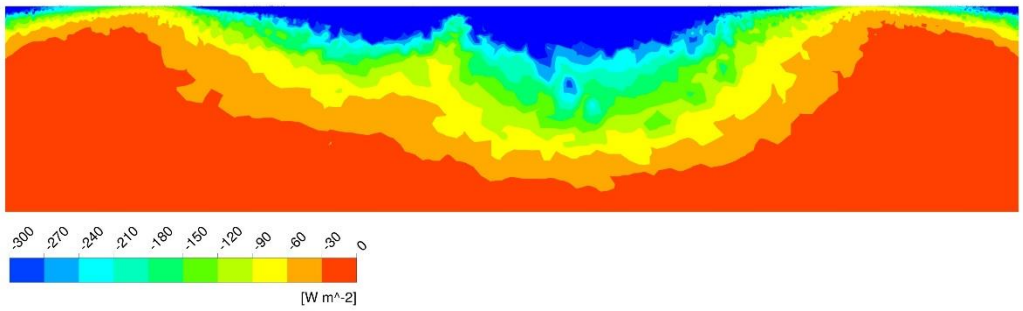

Fin 15, Side A

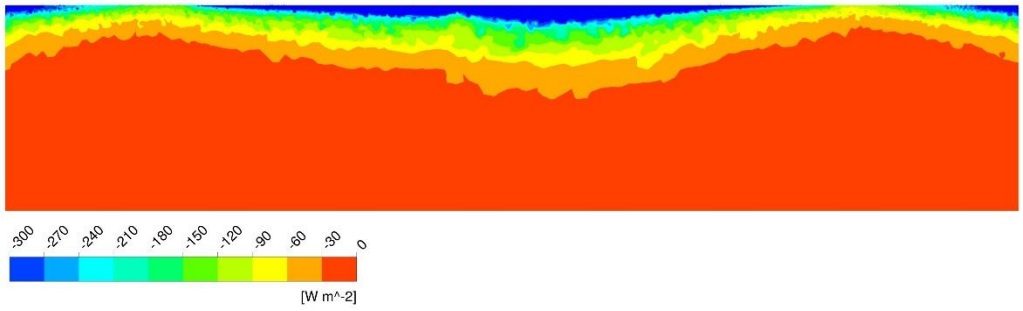

Fin 15, Side B

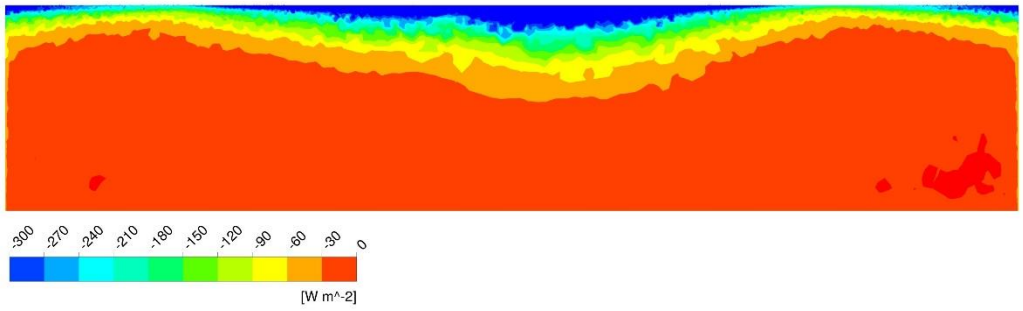

Fin 16, Side A

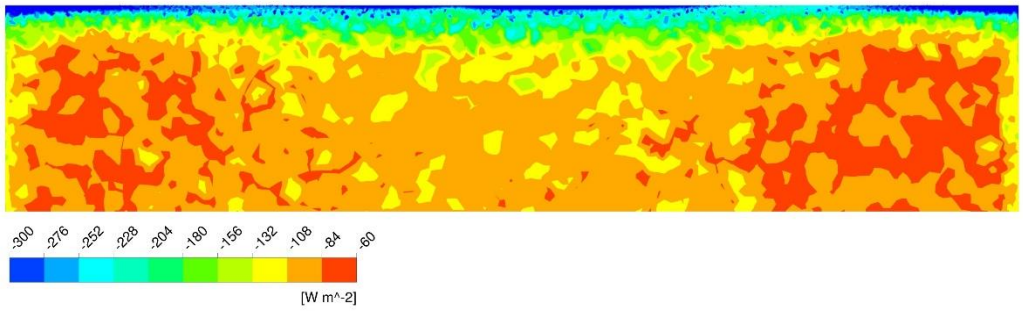

Fin 16, Side B